Chair of Materials Physics

Doctoral Thesis

Metallic Thin Film Fatigue Dominated by the Interface Character

Dipl.-Ing. David Gebhart

October 2024

AFFIDAVIT

I declare on oath that I wrote this thesis independently, did not use any sources and aids other than those specified, have fully and truthfully reported the use of generative methods and models of artificial intelligence, and did not otherwise use any other unauthorized aids.

I declare that I have read, understood and complied with the "Preamble on Integrity in Academic Study, Teaching, and Research Operations" of the Montanuniversität Leoben.

Furthermore, I declare that the electronic and printed versions of the submitted thesis are identical in form and content.

Date 25.Oct.2024

David Gebhart

(The original signature is kept at the university)

This doctoral thesis was written at the Erich Schmid Institute for Materials Science, Austrian Academy of Sciences, within the framework of the D-A-CH cooperation FATIFACE. This work was supported by the Austrian Science Fund (FWF) [Project I 4384-N].

Erich Schmid Institute of Materials Science
Austrian Academy of Sciences
Jahnstraße 12
A-8700 Leoben

Acknowledgements

Special thanks to my supervisor Megan for all of her support, for always taking time out of her day when I needed something, and especially for her understanding when I missed some deadlines. Your patience helped me a lot.

I also thank everyone who worked on the project, Anna, Benoit, and Christoph, those who supported the project, and all the people at the Erich Schmid Institute.

Thank you to my family and old friends whom I couldn't see as often as I would have liked to during the work on this thesis. Fortunately, I made some great new friends along the way.

Abstract

Metallic thin films are integral to a multitude of technological applications, including flexible electronics, photovoltaics, and micro-electromechanical systems (MEMS) where they are frequently subjected to mechanical and thermomechanical stresses. Understanding the fatigue behavior and damage mechanisms of these films, especially the influence of interfaces, is crucial for enhancing their reliability and longevity. This thesis investigates the fatigue properties and mechanical damage evolution in gold thin films on polyimide substrates, both with and without a chromium interlayer, as well as in freestanding Au films.

Utilizing in-situ electrical resistance measurements during cyclic loading, we present the first qualitative report on the importance of full width at half maximum (FWHM) analysis of electrical resistance in cyclic loading investigations. This new concept provides access to crack opening characteristics, which could not be tracked before, analyzing only resistance maxima and minima within each cycle. An increase in the resistance peak width correlates with a transition from necking to through thickness crack formation, and FWHM values can be used to detect through thickness cracks. We also reveal that electrical resistance data can be correlated to three domains of damage propagation and to grain growth. The new method is simple to implement and offers a cost-effective alternative to traditional, time-intensive inspection techniques. A case is made for more extensive use of electrical resistance data, emphasizing its ease of acquisition and the potential for quick in-situ analysis once data processing methods are established.

Additionally, we employ in-situ transmission electron microscopy (TEM) in a cross-sectional specimen to observe dislocation activities and associated fatigue properties at the nanoscale. In the Au/Cr bilayer system, dislocation wall structures inside an ultrafine-grained Au film evolved into what appears to be a geometrically necessary boundary (GNB) parallel to the Cr-Au interface. The GNB acted as an obstacle to dislocation motion, with activated slip systems terminating at its junction, significantly impeding dislocation mobility and enhancing fatigue resistance. These findings suggest that such geometrically necessary structures may play a significant role in damage accumulation in bilayer samples where a strain gradient is present, potentially increasing fatigue life.

In freestanding Au films, intermittent TEM and 4D scanning transmission electron microscopy (4D-STEM) reveal substantial out-of-plane grain rotation, grain boundary migration, and grain growth in regions surrounding propagating cracks initiated from a notch. Crack propagation follows a mixture of intergranular and transgranular fracture

modes. Orientation mapping demonstrates that deformation localization and crack propagation are linked to the local grain orientation, specifically the misorientation between neighboring grains. Cyclic deformation leads to out-of-plane grain rotation around the crack tip, highlighting this as an important deformation mechanism for freestanding metal thin films.

Overall, this work advances the understanding of interface-related damage mechanisms in metallic thin films and emphasizes the critical role of microstructural characteristics on fatigue behavior. The findings contribute valuable insights for the design of more reliable thin film components in flexible electronic devices and other applications where mechanical integrity is crucial. The observed mechanisms, such as the formation of GNBs and the impact of grain orientation on crack propagation, may lead to future tailoring of multilayer systems and microstructures to enhance the fatigue lifetime of thin films.

Kurzfassung

Metallische Dünnschichten sind integraler Bestandteil einer Vielzahl technologischer Anwendungen, einschließlich flexibler Elektronik, Photovoltaik und mikroelektromechanischer Systeme (MEMS), wo sie häufig mechanischen und thermomechanischen Belastungen ausgesetzt sind. Das Verständnis des Ermüdungsverhaltens und der Schadensmechanismen dieser Filme, insbesondere des Einflusses von Grenzflächen, ist entscheidend für die Verbesserung ihrer Zuverlässigkeit und Langlebigkeit. Diese Arbeit untersucht die Ermüdungseigenschaften und die mechanische Schadensevolution in Gold-Dünnschichten auf Polyimid-Substraten, sowohl mit als auch ohne eine Chrom-Zwischenschicht, sowie in freistehenden Gold-Schichten.

Unter Verwendung von elektronischen in-situ-Widerstandsmessungen während der zyklischen Belastung präsentieren wir den ersten qualitativen Bericht über die Bedeutung der Analyse der Halbwertsbreiten (FWHM) in Untersuchungen zur zyklischen Belastung. Dieses neue Konzept bietet Zugang zu Merkmalen der Rissöffnung, die zuvor nicht verfolgt werden konnten, wo nur die Widerstandsmaxima und -minima innerhalb jedes Zyklus analysiert wurden. Ein Anstieg der Halbwertsbreite korreliert mit einem Übergang von unvollständigen Rissen zur Rissbildung durch die gesamte Dicke, und FWHM-Werte können verwendet werden, um Risse durch die gesamte Dicke zu erkennen. Wir zeigen auch, dass elektrische Widerstandsdaten mit drei Bereichen der Schadensausbreitung und dem Kornwachstum korreliert werden können. Diese Methode ist einfach zu implementieren und bietet eine kostengünstige Alternative zu traditionellen, zeitintensiven Inspektionstechniken. Es wird der Nutzen der umfangreichen Prozessierung von elektrischen Daten dargestellt, wobei die leichte Beschaffung und das Potenzial für eine schnelle in-situ-Analyse dieser Datenverarbeitungsmethoden betont wird.

Darüber hinaus verwenden wir in-situ-Transmissionselektronenmikroskopie (TEM) an einer Querschnitts-Probe, um Versetzungsaktivitäten und zugehörige Ermüdungseigenschaften im Nanobereich zu beobachten. Im Au/Cr-Schichtsystem entwickelten sich Wandstrukturen innerhalb eines ultrafeinkörnigen Au-Films zu dem, was eine *geometrically necessary boundary* (GNB) parallel zur Cr-Au-Grenzfläche zu sein scheint. Die GNB wirkte als Hindernis für die Versetzungsbewegungen, wobei aktivierte Gleitsysteme an ihrer Verbindung endeten und die Versetzungsmobilität erheblich beeinträchtigten und die Ermüdungsresistenz erhöhten. Diese Ergebnisse deuten darauf hin, dass solche Strukturen eine bedeutende Rolle bei der Schadensakkumulation in Schichten mit Spannungsgradient spielen können und potenziell die Ermüdungslebensdauer erhöhen können.

In freistehenden Au-Filmen zeigen TEM und 4D-Rasterelektronenmikroskopie (4D-STEM) eine erhebliche *out-of-plane* Kornrotation, Kornverschiebung und Kornwachstum in Bereichen um sich ausbreitende Risse, die von einer Kerbe ausgehen. Die Rissausbreitung folgt einer Mischung aus intergranularem und transgranularem Verhalten. Großflächige Indizierung der Kornorientierungen (*orientation mapping*) zeigt, dass die Deformationslokalisierung und die Rissausbreitung mit der lokalen Kornorientierung, insbesondere der Fehlorientierung zwischen benachbarten Körnern, verbunden sind. Zyklische Deformation führt zu einer *out-of-plane* Kornrotation um die Rissspitze, was dies als wichtigen Deformationsmechanismus für freistehende Metall-Dünnschichten hervorhebt.

Insgesamt fördert diese Arbeit das Verständnis von grenzflächenbezogenen Schadensmechanismen in metallischen Dünnschichten und unterstreicht die kritische Rolle der mikrostrukturellen Merkmale in ihrem Ermüdungsverhalten. Die Ergebnisse liefern wertvolle Erkenntnisse für die Gestaltung zuverlässigerer Dünnschichtkomponenten in flexiblen elektronischen Bauteilen und anderen Anwendungen, in denen mechanische Langlebigkeit entscheidend ist. Die beobachteten Mechanismen, wie die Bildung von GNBs und der Einfluss der Kornorientierung auf die Rissausbreitung, können zur zukünftigen Anpassung von Mehrschichtsystemen und deren Mikrostrukturen führen, um die Ermüdungslebensdauer von den Systemen zu erhöhen.

Contents

1

Introduction

Contents

1.1 Motivation and Aim

Metal films are found across a broad spectrum of technological applications in which they are exposed to mechanical or thermomechanical stresses. Flexible electronics, photovoltaics, micro-electromechanical systems (MEMS), semiconductor technologies, optical devices, and space applications are just a few examples of their widespread use in modern technology. The metal films often serve as electrical conductors for power or signal transmission but they can also be used for other characteristic properties, e.g. their thermal conductivity or their specific optical properties — their reflection, refraction, absorption, and transmission characteristics across the different wavelengths. The films are often not freestanding and there are usually interfaces to substrates and other functional layers present. Introduced stresses and strains can be rather small due to thermal variations and differences in coefficients of thermal expansion (CTEs), or more pronounced due to mechanical events, such as the bending of a foldable display.

To test a material system's damage resistance, one can perform monotonic loading where the material is exposed to increasing stress until it fractures, or until a certain failure criterion is reached. From such investigations, it is established that ductile metal films on flexible substrates form cracks through necking of the film, and ultimately rupture of the film, resulting in channel cracks or through thickness cracks (TTCs) [1, 2]. However, the damage in thin film applications is usually not formed in single events, rather damage occurs through accumulated plastic flow over multiple stress cycles. To investigate such damage it is beneficial to perform fatigue tests. Fatigue testing can be performed in the low cycle regime ($\sim 10^3$ cycles), the high cycle regime ($\sim 10^6$ cycles), and the very high cycle regime ($\sim 10^9$ cycles) where one is mainly interested in damage accumulated through vibrations. There are several established methods in mechanical fatigue testing of metal films on flexible substrates, such as uniaxial cyclic tensile loading, cyclic bending, and resonance loading, summarized in a review by Luo et al. [3]. Fatigue experiments by Sim et al. on polymer-supported face-centered cubic (fcc) Ag thin films found a cracking mechanism similar to that in monotonically loaded films, with debonding, strain localization, necking, and ultimate rupture [4]. The work also describes a second mechanism of crack formation, with the formation of extrusion-intrusion pairs along with void formation at the interface, which is commonly observed in similar experiments in the literature [4, 5, 6, 7].

Extensive fatigue investigations of metal films on flexible substrates have been performed over the years. Available studies mostly investigate different parameters of the materials system, such as film thickness [5, 8, 9] and microstructure [8, 10]. Available research is lacking studies on the effects of the type of interface and the interfacial properties on fatigue damage mechanisms in thin films.

This work aims to contribute to the understanding of interface-related damage in thin metal films. Material systems composed of various combinations of gold, chromium, and polyimide are investigated for their fatigue characteristics. With in-situ experiments and data processing methods, focus is placed on the different interface characteristics and their influence on the fatigue properties of a material system.

1.2 Material System

1.2.1 The Polyimide Substrate Upilex®-S

Polyimides (PIs) are a class of polymers with properties that are well-suited for a variety of research, industrial, and technological applications. Besides excellent chemical stability and high mechanical strength, one of their main advantages is their wide range of thermal stability, with an upper limit of up to 500 °C [11, 12, 13, 14, 15]. PIs were first synthesized in 1908 by Bogert and Renshaw [16] and in 1955 the first high molecular weight aromatic PIs were produced in a two-step polycondensation process [15] which led the way for the first commercially available PI film in the 1960s with DuPont's Kapton® [12].

PIs are synthesized through a straightforward process from two precursor compounds, a dianhydride and a diamine, which gives rise to great variability in choosing the specific precursors and modifying the product's properties. A very common synthesis method is a two-step process: First, the dianhydride and the diamine are stirred in a polar, aprotic solvent where polymerization takes place to form a poly(amic acid). The poly(amic acid) resin solution can then be shaped into the desired form using methods such as casting, spin coating, or blade coating. In the second step, the resin is heated which leads to solvent evaporation and induces imidization which is an intramolecular ring-closure reaction, releasing water condensate. The chemical synthesis is outlined in Fig. 1.1 with the example of Upilex®-S which is a product of 3,3',4,4'-biphenyltetracarboxilic dianhydride (BPDA) and p-phenylene diamine (PDA). Besides thermal imidization, chemical imidization is also widely used, and there are many additional synthesis options in the production of polyimides. D.-J. Liaw et al. wrote an extensive review on synthesis methods, different precursors, and the relationship to the properties of the resulting polyimides [15].

The PI substrate used in this work is Upilex®-S (see Fig. 1.1), an aromatic PI. The high thermal and mechanical stability of such PIs is attributed to rigid chains and strong interchain interactions due to strong polar groups and high polarizability of the planar, aromatic groups [15], as well as due to the formation of inter- and intramolecular charge transfer complexes [18] which are also the reason for the characteristic yellow/brown tint of many polyimides. With the used substrate thickness of 50 µm, some properties of interest to this work are summarized in Table 1.1, provided by the manufacturer [19].

1.2.2 Gold and Chromium

To investigate the interfacial effects on fatigue properties of metallizations used as electrical conductors, this work uses a main functional layer of Au on Upilex®-S, and

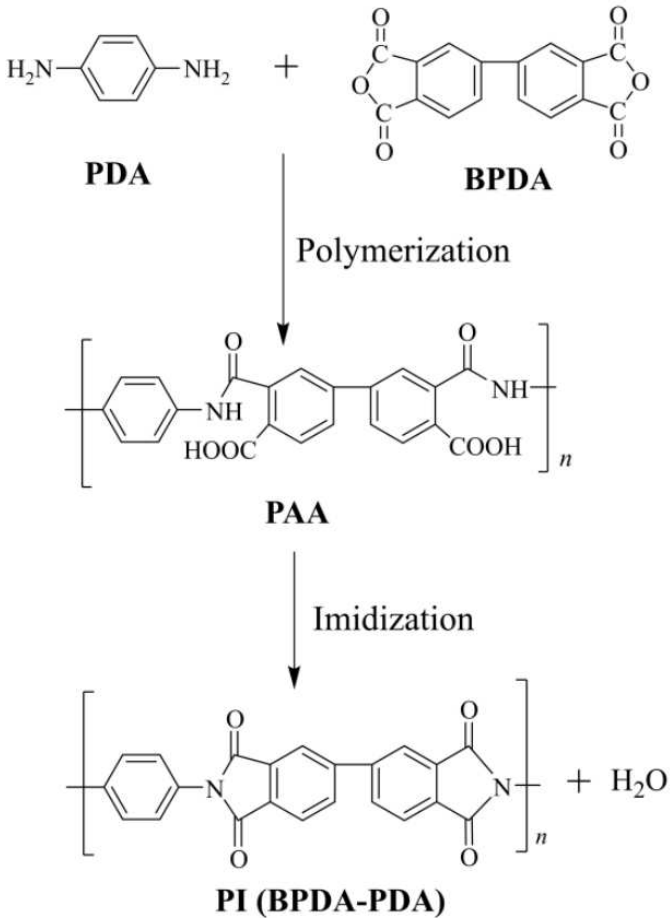

Figure 1.1: Scheme of the common 2-step synthesis route of polyimides illustrated through the example of Upilex®-S [17].

Table 1.1: Properties of Upilex®-S (50 µm), provided by the manufacturer [19]

Property	Value
Tensile Strength	460 MPa
Tensile Modulus	9.3 GPa
CTE (50-200°C)	16 ppm / K
Surface Roughness (R_a)	1.2 nm
Heat Life (tensile strength)	
20,000 h (fixed temperature)	290 °C

aims to compare this system to one with a thin Cr interlayer placed between the polymer substrate and the Au layer. Additional experiments were performed on freestanding Au films. This leads to three types of interfaces for the main Au layer: (i) no interface for

the freestanding samples, (ii) a soft interface at the polymer-metal junction for the PI-Au specimen, and (iii) a hard interface between Cr and Au for the PI-Cr-Au specimen.

With its chemical inertness and high resistance to oxidation, experiments with Au yield clean data from measurements where chemical effects, such as damage introduced due to surface oxidation, are minimized. Au is sometimes used as an electrical conductor when the benefits of its chemical stability and high conductivity outweigh the higher material costs. It is a fcc metal and shows ductile behavior at room temperature. Its fatigue properties are similar to a certain extent to other fcc metals commonly used in conducting films or traces, such as Ag, Cu, and Al. Cr was chosen for its known strong adhesion to polyimide [20], its established use as an adhesion-promoting interlayer between different metals and polyimide substrates [21], and for its body-centered cubic crystal structure and brittle fracture behavior at room temperature.

At room temperature bcc metals generally show less ductility than fcc metals. One of the main attributing factors to ductility is the ability of dislocations to glide along activated slip systems. While the bcc structure gives rise to 48 available slip systems ({110}<111>, {112}<111>, and {123}<111>), more than the 12 slip systems available in the fcc structure, {111}<110>, the slip planes in the bcc structure are less densely packed and not as easily activated. The closest-packed planes in the bcc structure, {110}, possess a lower atomic density than the {111} planes of the fcc structure. Dislocations require higher energy, or resolved shear stress, to glide along available slip systems in bcc metals compared to fcc metals which is the reason why bcc metals are generally less ductile than fcc metals.

1.2.3 Film Deposition through Thermal Evaporation

There is a wide variety of established options for metal film deposition. While thicker films are often deposited from a solution, as in electrochemical deposition and electroless plating, thin films mostly rely on chemical and physical vapor deposition (CVD; PVD) methods which occur through the adsorption of molecules (CVD) or atoms (PVD) on the substrate. In CVD processes, surface reactions of adsorbed molecules lead to the formation of metal layers, and due to surface diffusion of the chemical precursors homogeneous coverage of patterned surfaces can be achieved. PVD processes rely on the direct adsorption of metal atoms and ions from a gaseous state. Surface atom diffusion does occur to some extent in PVD methods, however, they show a strong line-of-sight effect where atoms are hardly deposited onto obstructed surface areas, which makes them best suited for flat substrates.

The films studied in this work were deposited through thermal evaporation, a PVD process. In a vacuum chamber, the metal to be deposited is placed in a high melting point refractory metal crucible. Through the application of a direct current and through Joule heating, the temperature of the crucible is increased to a point where the metal inside evaporates. The evaporated metal condenses on a substrate in the line of sight of the crucible. A detailed explanation of the deposition chamber used in this work is available in E. Preiss' dissertation investigating the fracture toughness of freestanding metal films [22].

1.3 Adhesion at the Metal-Polyimide Interface

With adhesion being a known factor in determining the fatigue lifetime of metallizations on polymer substrates [23], it is necessary to take a closer look at what adhesion is and what mechanisms are involved. Intuitively it seems like a rather trivial thing to have two surfaces stick to each other, but there are a variety of mechanisms involved.

1.3.1 The Work of Adhesion and the contributing Mechanisms

When adhesion is quantified in scientific works, it is mostly given in terms of the work of adhesion, W_{ad}. It was first described by A. Dupré for solid-liquid interfaces [24] and, slightly modified to its most simple thermodynamic form, W_{ad} can be given as $W_{\mathrm{ad}} = \gamma_1 + \gamma_2 - \gamma_{12}$, with γ_1 and γ_2 as surface energies of two materials, and γ_{12} the interface energy between the two materials. It has units of energy per area, or $\mathrm{J/m^2}$. A variety of mechanisms contribute to the total work of adhesion which can be divided into mechanical, physical, and chemical interactions. Mechanical adhesion stems from interlocking effects that are heightened by increased surface roughness and diffusive processes. Physical effects include all electrostatic effects of (induced) dipole - (induced) dipole interactions, or quadrupole interactions, and hydrogen bonding. Lastly, chemical effects are due to the formation of covalent or ionic bonds at the interface, and acid-base interactions between an electron pair acceptor (Lewis acid) and an electron pair donor (Lewis base), including coordination complex formations. In general, the bond strength of physical interactions is more than an order of magnitude lower than that of chemical interactions, however, the density of interaction sites is often higher for physical interactions [25] (see Fig. 1.2). Thermodynamically the total work of adhesion can be expressed as the sum of the work of adhesion from each contributing type of interaction [25].

1.3.2 Possible Chemical Interactions at Metal-Polyimide Interfaces

At a metal-polyimide interface, one might intuitively expect no, or very little, chemical bonding between the two materials, however, there are a variety of ways in which chemical interactions can occur. In general, chemical interactions are considered to result in stronger adhesion than physical interactions, and possible bonding sites for metals are found all over the monomer units (carbonyl groups, imide rings, benzene rings, etc.)

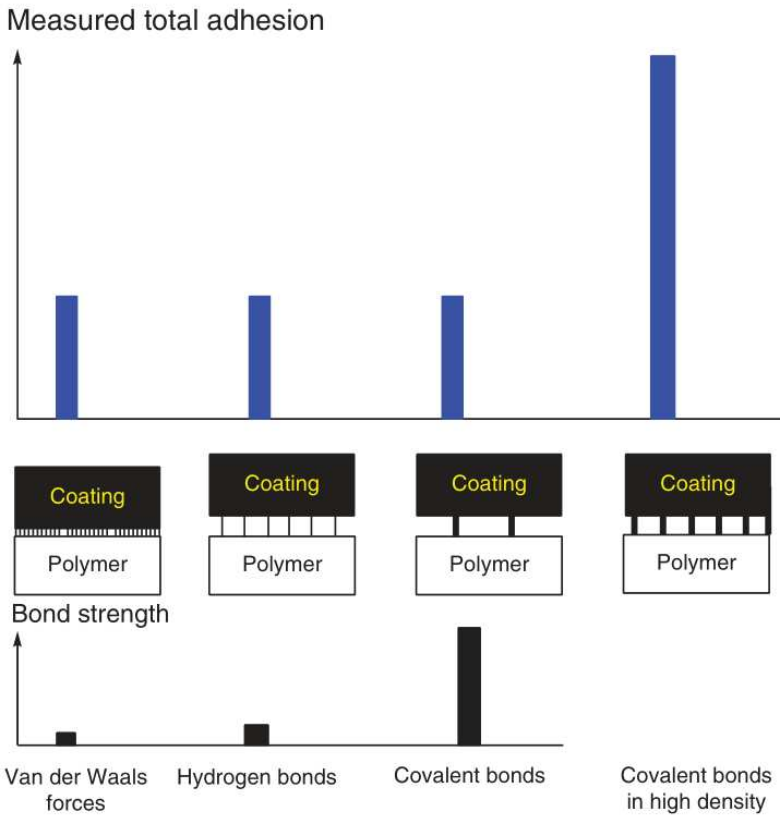

Figure 1.2: Illustration comparing the strengths of different single bonds, the number of bonds, and the resulting work of adhesion due to each kind of interaction. Reprinted in modified form with permission from [25].

[26]. The redox potential of metals is of importance for chemical reactions between metals and polymers [25]. A study by Strunskus et al. [26] found no chemical interaction between Au, Ag, Cu, and Pd, at low coverage depositions on PI (pyromellitic dianhydride - 4,4'-oxydiphenylamine, short PMDA-ODA, or Kapton®) without surface activation before metal deposition, while they found some chemical interaction with Cr, and strong chemical interaction and a reduction of the PI by potassium. X-ray photoelectron spectroscopy (XPS) studies of Cu depositions on a PI substrate (PMDA-ODA) with higher coverages showed that Cu cluster formation led to stronger chemical interaction with the PI, indicating the breaking of at least one bond in the PI's imide rings, while no strong chemical interaction was found for single Cu atoms at the surface [27]. The work argues that this chemical interaction may be the reason for an increased adhesion strength of Cu compared to the less reactive Au. A different group also reported chemical interaction of Cu with PMDA-ODA, with PMDA as the preferred interaction site [28]. Early computational studies of Cr depositions on PMDA-ODA raised the possibility of

metal arene complex formations between Cr and the phenyl groups of the PI [29, 30] but another study found it to be more likely that the formation of Cr-O and Cr-N polymer-bound intermediates and the subsequent formation of Cr-oxides, nitrides, and carbides were responsible for the observed shifts in spectroscopic data due to chemical interactions [31]. However, most studies on chemical interactions at the interface between Cr with PI were done in the 1980s and 90s and the findings remained inconclusive [26, 32, 33], with one study even proposing that the arene complex formation may be the reason for the increased adhesion of Cr on PI compared to Cu that does not form stable arene complexes [33]. As far as the author is aware, the exact chemical interaction mechanisms at the Cr-PI interface have not been revealed to this day but modern density functional theory (DFT) calculations might be able to provide more conclusive findings. For Al, which is a stronger reducing agent and oxidizes more readily, a variety of chemical reactions are found at the PI interface, preferentially at the carbonyl groups [34, 35].

In summary, adhesion is an additive quantity of contributions from mechanical, physical, and chemical effects. Due to high bond energies, chemical effects, or chemical bond formations, are potentially the largest contributor to the total work of adhesion at the interface of two materials. It is known that for some metals, depositions on polyimide substrates lead to chemical bond formation at the interface and this will result in increased adhesion compared to metals that show less, or no, chemical interaction. Whether chemical reactions occur at the interface depends on how reactive a metal is, with the metal's redox potential as a good indicator, and possibly also its d-electron configuration. More noble metals, such as Au, Pd, and Ag, tend to show less chemical interaction with the polyimide substrate compared to more reactive metals like Al and Cr. Therefore, the less noble metals would be more suitable as adhesion-promoting interlayers in technical applications.

1.4 Electrical Resistance and Data Analysis

A common method in fatigue investigations of metal deposition on flexible substrates is to apply cyclic strain while simultaneously recording electrical resistance data. Such in-situ experiments generate a good amount of data but the community seems to be lacking established methods to analyze those data sets, or even to define failure at a certain level of increased resistance. This section briefly describes electrical resistance from an ideal solid, to a real sample, and finally to a film with introduced fatigue damage. It gives a brief overview of electrical resistance from a theoretical viewpoint to outline how parameters like grain size influence electrical resistance measurements. Then a more practical perspective is presented and it is outlined how different characteristics of fatigue damage in a sample may be reflected in in-situ electrical resistance datasets.

1.4.1 Electrical Resistivity of a Metal

The theory of electrical resistivity in a solid is a complex topic and the next paragraphs aim to give an overview, without any claim of a complete description. This section is largely based on a comprehensive, but still quite intuitive, description by Philip Hofmann in his book on solid-state physics [36].

To talk about the electrical resistivity of a solid, a brief description of energy bands is needed. An energy band is a quasi-continuum of states electrons can occupy on the energy scale. Energy bands are a result of interactions due to the overlap of a large number of bonding and antibonding molecular orbitals in a solid and the resulting shifts of discrete energy states that lead to an almost continuous distribution of electronic states on the energy scale. The highest energy level that electrons occupy at 0 K is called the Fermi energy. The low electrical resistivity of metals stems from the fact that the Fermi energy lies within a partially filled energy band. This results in a high density of unoccupied electronic states around the Fermi energy which electrons can fill when they are excited to higher energy levels. Electrons need to occupy those higher states as they gain kinetic energy in the form of drift velocity when an electric field is applied, to be able to move in one direction and contribute to electric current. The density of states around the fermi energy is directly related to the electrical resistivity of a metal.

Another important factor in the electrical resistivity of a metal is electron mobility. The scattering of electrons at positively charged ions of the crystal lattice plays an important contribution to the electron mobility in a crystal. As per Bloch's theorem, in an ideal periodic potential in a crystal lattice, electrons would not scatter at all at

the atomic nuclei and the resistivity of a metal would theoretically go to zero. This theoretically infinite conductivity must not be confused with superconductivity, best described by the formation of Cooper pairs in BCS theory [37]. In real crystals, however, there is never a perfect periodic lattice and scattering of electrons at deviations from the periodic lattice potential has a large influence on the resistivity of a metal. Deviations of the periodic potential are introduced through phonons and at defects, such as vacancies, impurities, dislocations, or grain boundaries. The scattering probability of electrons at lattice sites is often described by their mean free path. This mean free path is directly related to electron mobility in the crystal lattice. Another factor influencing electron mobility is the effective mass of conduction electrons. To give an intuitive description of the effective mass of an electron, one could say it is a measure of how easily an electron can be accelerated in the crystal.

There are other factors that can influence the electrical resistivity of a metal, such as electron-electron scattering, but for a more complete description, the reader is referred to the standard literature on solid-state physics.

1.4.2 Electrical Resistance of a Metal Component

The influence of the scattering of electrons at lattice ions becomes apparent when the mean grain diameter in a sample is reduced. The resistivity of a sample includes a term that is inversely proportional to the mean grain diameter [38, 39]. Especially in the ultrafine-grained (UFG) and in the nanocrystalline (NC) regime, deviations in grain size can lead to large deviations in the material's resistivity. Fig. 1.3, taken from [40], depicts the resistivity of PVD deposited Cu films. It shows that when working with UFG and NC metal samples, one has to be considerate of the mean grain diameter when comparing different samples' electrical properties, and that grain growth can play a role in influencing a sample's electrical resistance measurements during fatigue testing.

1.4.3 Electrical Resistance of Metal Films during Fatigue Testing

The electrical resistance of a sample depends on the electrical resistivity of the material, ρ, the length of the sample, L, and its cross-sectional area, A:

$$R = \rho \frac{L}{A} \tag{1.1}$$

Fatigue tests of metal films apply cyclic strain, mostly with peaks in the range of 0.1 to 5 %, depending on the material and the investigated regime from low- to high-cycle

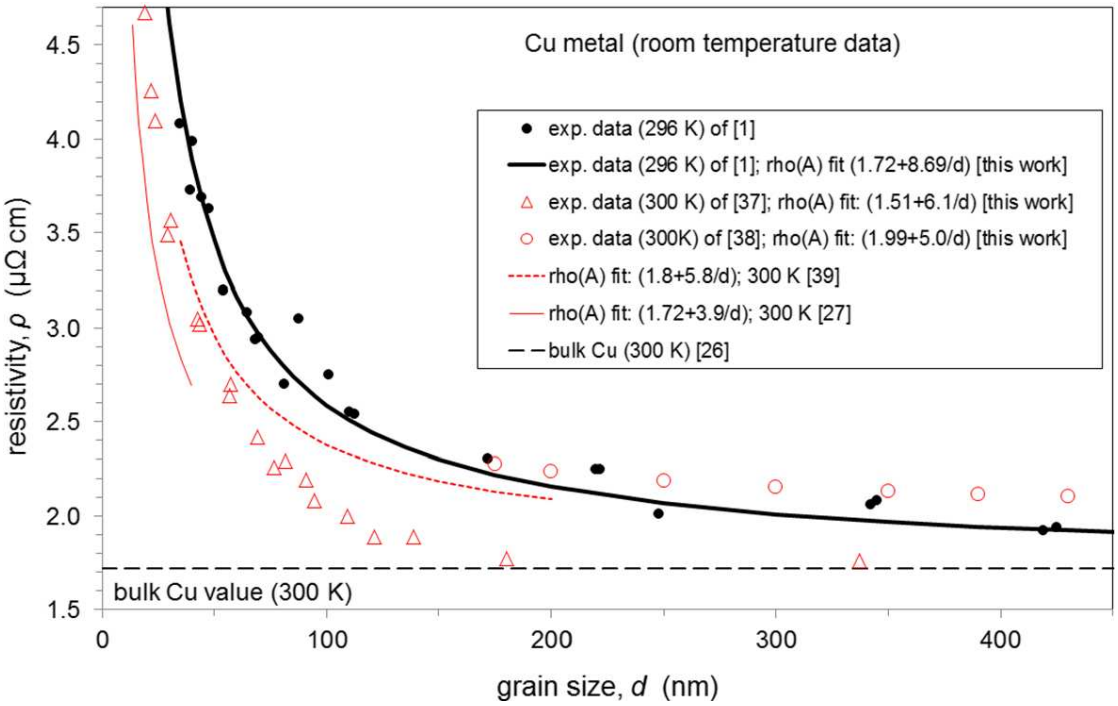

Figure 1.3: Grain size dependence of electrical resistivity on PVD deposited copper films, reprinted with permission from [40].

fatigue. During such tests, cracks can start to form in the film and when that happens, the film's electrical resistance increases significantly and the parameters discussed in the previous sections become negligible. How exactly the evolution of somewhat randomly distributed and possibly meandering microcracks influences a film's overall resistance over time can only be estimated by numerical simulation. However, a simplified model can be of great help in understanding complex relationships in large datasets acquired with in-situ electrical resistance measurements during fatigue testing. Here, an approach is presented that views a cracked film as a network of resistors, parallel and in series.

Cracks in metal films occur as partial cracks, or necking, and through thickness cracks (TTCs) (see Fig. 1.4 (b) and (c)). While cracks do meander and are not always straight, their average propagation direction is perpendicular to the straining direction. In a necking crack, the two crack faces are still connected and there is an electrically conductive material bridge at the center of the crack which persists throughout a strain cycle. The necking cracks may transform, or partly transform, into TTCs during fatigue testing. In TTCs, the cracks are fully opened and the crack faces are not connected. However, at strain minima during cyclic loading, the crack faces may come into contact with each other, creating conductive pathways.

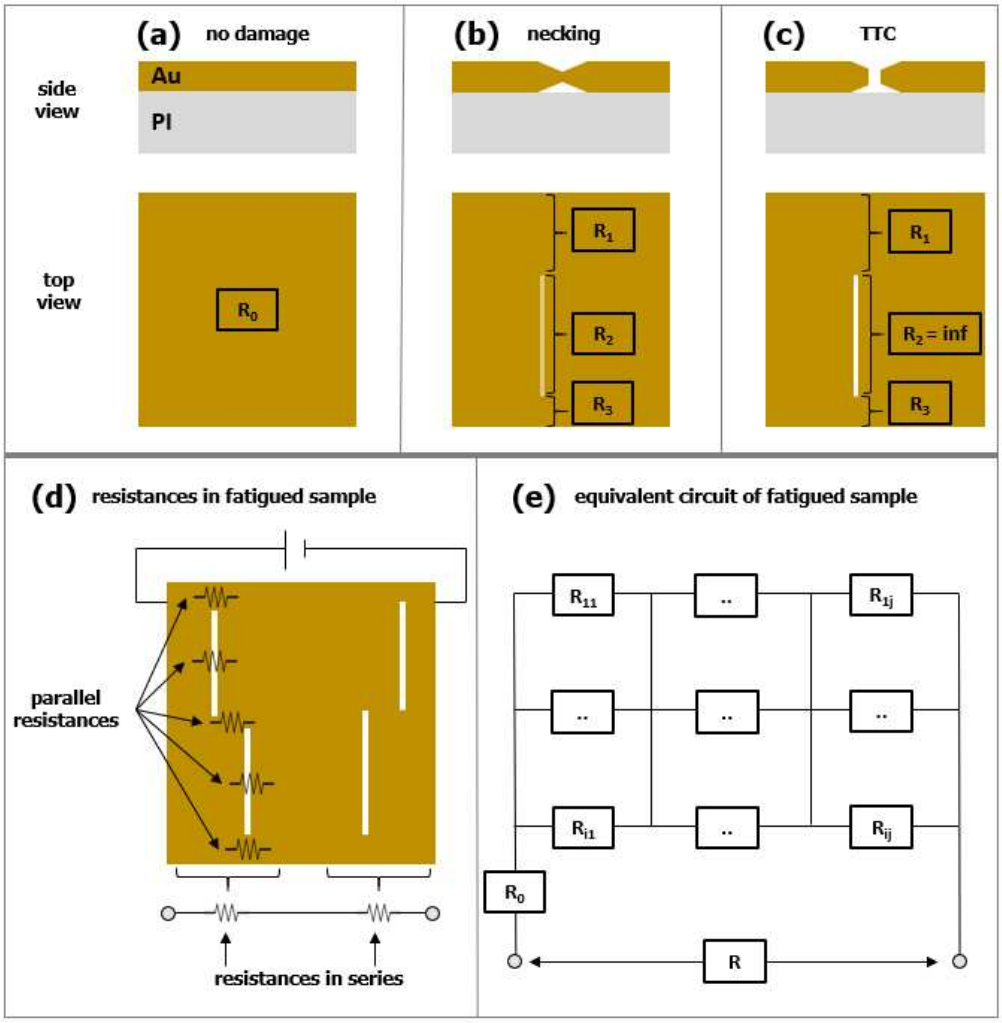

Figure 1.4: Model describing conductive pathways around and through crack sites as an interconnected mesh of wires with varying electrical resistance magnitudes. (a) to (c) gives an area with three different damage states as cross-cuts and top-views with indicated resistances. R_0 is the as-deposited film's resistance. (d) depicts a larger area from the top-view and indicates the parallel and in-series resistances, and (e) shows a general equivalent circuit for this model.

Fig. 1.4 presents a simplified model of electrical resistance in a fatigued film. All paths electricity can flow through can be taken as thin wires that are interconnected to create a complex mesh of conductive pathways. For each one of those imagined wires, the largest factor influencing its resistance is the smallest cross-sectional area of its conductive pathway, which is a type of bottleneck of charge carrier transport. Fig. 1.4

(e) depicts an equivalent circuit for a film with randomly distributed cracks. It consists of many resistances, the wires mentioned above, which are connected in parallel and in series. Two resistors are parallel when they are approximately equally far away from the current sources (measurement electrodes), which would for example be the case for two conductive pathways around both sides of a crack. Resistors are in series when one is further away from the current source. Of course, an increase in the number of parallel resistances of fixed magnitude leads to a decrease in total resistance, while an increase in resistances in series leads to an increase in total resistance.

This simplified model makes it immediately obvious that single measurements of direct current (DC) electrical resistance can never give any separate information on the number of parallel resistors or the number of resistors in series. The measurement only contains a product of parallel and in-series resistors, which can never be separated. There is always a system with an increased number of parallel resistors and a decreased number of in-series resistors that leads to the same total resistance as another system, or vice-versa. In a real sample, the numbers of parallel and in-series resistors are measures of average crack length and linear crack density respectively. Cracks run perpendicular to the straining direction and if the cracks' average length is increased, there are fewer conductive pathways around the cracks, decreasing the number of parallel resistors. Linear crack density is a measure of crack density along the straining direction and if there are more cracks in this direction, the number of resistors in series increases. Naturally, it is known that those two parameters cannot be separated in single measurements [41].

While single measurements can only reflect the total damage in a system, studies of meta-parameters of large measurement series can contain additional information. For example, with increasing strain, the cross-sectional area of conductive pathways will decrease sharply and go to zero when TTCs are present which leads to broad electrical resistance peaks within each strain cycle. Such studies are presented in Chapters 2 and 3.

1.4.4 State of the Art in in-situ Electrical Resistance Data Analysis

Collecting large data sets of electrical resistance data during fatigue testing of metal films on polymer substrates is a rather straightforward task and many groups working on the topic do collect the data. However, the data sets are hardly analyzed in depth. They are mostly used to determine the failure of different material systems once their electrical resistance values cross a certain threshold percentage increase [42, 43, 4, 44, 45, 9]. Some studies venture into deeper analysis of the data sets but a comprehensive description is missing in the literature. Gence et al. looked at single-cycle resistance data and the evolutions of cyclic data in thin films of titanium nitride-silver nanowire nanocomposites

and correlated the reversibility of resistance-increasing processes in their samples [46]. Graz et al. found double peaks in electrical resistance data in gold films due to the formation of gold islands and closure of longitudinal cracks with lateral contraction within strain cycles [47].

In recent years semi-empirical models were developed, describing the electrical resistance increase due to the the degradation of metal films during fatigue testing. Glushko et al. found that the resistance increases with the second power of the areal crack density and with the fourth power of the crack length, assuming TTCs [41]. Cheng and Li [48] developed a complex degradation model linking crack initiation and propagation to electrical resistance data, however, their model requires a rather large number of model fitting parameters. The model may be used to predict the lifetime of a material system when good fitting parameters are found and one model parameter (e.g. film thickness) is changed, and the model suggests that one might be able to derive the amount of inter- and transgranular cracking from the fitting parameters of recorded data. No available model tries to directly relate certain trends in data to distinct characteristics in fatigue damage accumulation. Chapters 2 and 3 presented in this work are intended to fill this gap and advocate for a more comprehensive analysis of available data.

1.5 Fatigue Failure in Thin Metal Films

Fatigue failure in metal films lacks a clear definition. When electrical resistance is measured as the failure indicator, an arbitrary percentage increase in terms of the initial electrical resistance is chosen and the cycle number at which the film surpasses this threshold is taken as the number of cycles to failure. In the literature, this threshold can range from 10 % [45] to 25 % [4]. The practical failure threshold of a film depends on its application — for the transmission of signals, even a hundredfold increase in initial resistance may not pose a problem but for power transmissions with high current densities, just a 20 % increase may lead to overheating. However, it could be beneficial to have a fixed value in the literature that determines where a film is considered to have failed for easier data comparison.

The resistance increase during fatigue cycling mostly stems from the initialization of cracks, and their propagation perpendicular to the loading direction. Cracks initiate at randomly distributed favorable spots in the sample where strain concentration is present [49]. Those points of stress concentration may be voids or small irregularities at the interface between the film and the substrate. The propagation of cracks can be of a more brittle nature where long, narrow, and rather straight cracks run parallel to each other through the film, or it can be more ductile where the cracks are generally shorter, broader, and meandering (see Fig. 1.5 for a representative comparison). In general, brittle cracking is detrimental to the fatigue lifetime of a film because the cracks show a faster propagation rate and their large lengths lead to larger resistance increases compared to shorter ductile cracks of the same crack density (see model depicted in Fig. 1.4).

Crack propagation consumes energy in the form of bond breaking and the formation of newly formed surfaces, and in the form of plastic deformation. Whether a film cracks in a brittle or ductile manner is mostly determined by dislocation mobility. In brittle crack propagation, large stress fields ahead of the crack tip lead to bond breaking and cleavage ahead of the crack tip. In ductile cracking, dislocation movement ahead of the crack tip leads to plastic deformation which absorbs and redistributes the large stress fields in this region, consuming energy and reducing the rate of crack propagation. This plastic deformation in ductile cracking can be seen in Fig. 1.5 where the ductile cracks appear broader than the more brittle ones, due to the plastic wake along the cracks. As previously discussed in Section 1.2, fcc metals are generally more ductile than bcc metals due to their increased dislocation mobility. Since ductile materials show larger resistance to fatigue damage they are generally preferred in applications where the film needs to withstand periodic mechanical stresses.

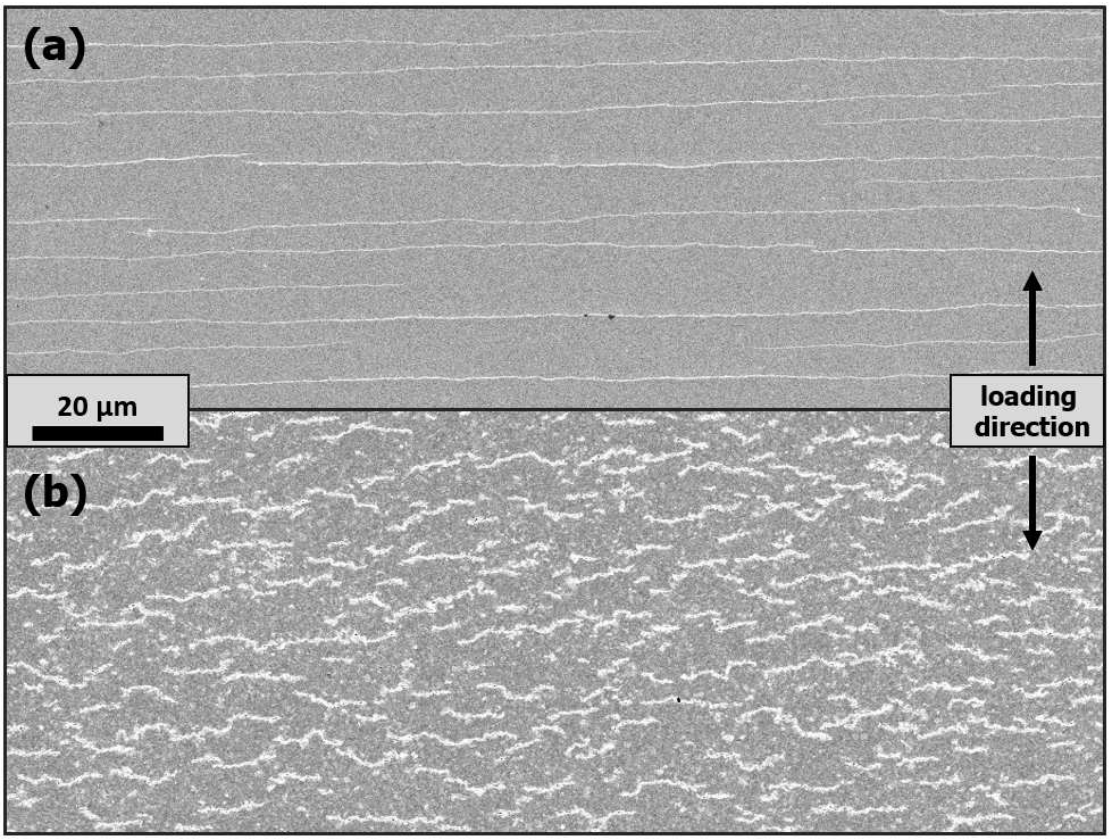

Figure 1.5: Difference in brittle and ductile cracks in scanning electron microscopy micrographs of fatigued metal films. (a) shows brittle cracking in a Cr film and in (b) ductile cracks are observed in a Au film.

Ductile crack propagation generally involves mechanisms based on plastic deformation, such as void formation through vacancy coalescence, and blunting and resharpening of the crack tip [50]. In ductile thin metal films, fatigue damage also involves dislocation-mediated processes. Cracks propagate at extrusion-intrusion pairs along slip planes, and at voids forming at the interface between metal and polymer leading to necking [23, 5]. While dislocation mobility is necessary to a certain extent to allow ductile crack propagation, it can also be detrimental to the fatigue lifetime of metal components. A well-known example of reduced dislocation mobility increasing the fatigue resistance of a metal is the Hall-Petch relation [51, 52], describing increased yield strength in materials when grain sizes are reduced due to grain boundaries acting as barriers to dislocation motion ahead of a crack tip. Similarly, subgrain cell structures may act as additional barriers to dislocation motion, increasing the fatigue resistance of a component [53].

1.6 In-Situ Transmission Electron Microscopy based Measurements in Fatigue Testing

In-situ measurements in fatigue testing of thin films are the continuous measurement of observables during the cyclical application of mechanical forces. Established methods in testing of thin metal films include the aforementioned electrical resistance measurements [49], measurements of internal stresses due to a shift in Bragg angle with a synchrotron x-ray radiation source [54], MEMS-based measurement set-ups [55], measurements inside a scanning electron microscope (SEM) [56], and transmission electron microscopy (TEM) based methods [57]. In-situ experiments generally require a much more complex measurement set-up and the measurement may influence a sample's fatigue properties due to radiation effects or changes in the environment (e.g. vacuum conditions [58, 59]). However, in-situ experiments are essential, and the ability to record data points during fatigue investigations allows insights that are otherwise impossible to achieve, and they are an indispensable addition to post-mortem analyses and ex-situ methods. Recent advancements and the development of direct electron detectors have progressed the development of 4-dimensional scanning transmission electron microscopy (4D-STEM) methods where electron diffraction patterns are recorded on top of micrographs.

In TEM, electrons pass through a thin, electron-transparent sample and the resulting contrast stems from scattering of part of the electrons while passing through the sample. There are two main operating modes. In TEM operation, a parallel beam of electrons is directed onto an area of the sample. By detecting unscattered electrons, an image is generated in the bright-field mode, and the detection of scattered electrons is called dark-field mode. In scanning transmission electron microscopy (STEM), the beam of electrons is not parallel but focused onto a point on the sample, and the beam is rastered over an area. In both operating modes, the sample needs to be electron-transparent. Electron transmission depends on several factors, such as the electrons' acceleration voltage, the material's atomic number and crystal orientation, and the thickness of the sample. Generally, a sample's thickness should be below 100 to 200 nm to achieve sufficient electron transparency in standard commercially available equipment.

1.6.1 Sample Preparation

Several routes are available to prepare a sample for TEM and STEM analysis. With mechanical sample preparation, a small part is cut from a specimen, ground down, and polished until the desired thickness is achieved. This is often challenging and can introduce defects and plastic deformations into the sample.

For single-phase materials, especially single-layer thin films, it can be beneficial to use a sacrificial substrate, deposit the material to the desired thickness, and selectively etch the substrate in wet chemical conditions, or with reactive ion etching.

For multi-layered films, a cross-section is necessary for (S)TEM analysis. When the electron beam intersects different phases, mismatches in crystallographic orientation can lead to increased electron scattering, significantly reducing overall electron transmission and obscuring the detailed information that can be obtained. An efficient way to obtain such cross-sectional samples is using a focused ion beam (FIB) to cut a thin and electron-transparent lamella from a specimen. From an ion source, often liquid Gallium in strong electric fields, ions are accelerated and focused onto a material. When the high-energy ions hit the sample, atoms are dislodged and sputtered, allowing the sample to be cut and milled on the micro and nanoscale.

To place the sample into a (S)TEM, micromanipulators are needed. Sharp needles controlled by piezo actuators are attached to the sample. This can be done by focused ion beam-induced deposition of a metal, often Platinium, by introducing a precursor gas into the vacuum chamber which leads to precise metal deposition where the focused ion beam interacts with the precursor gas. The sample is then lifted and attached to specialized TEM grids and cut from the micromanipulator.

1.6.2 Electron Diffraction and 4D-STEM

For a comprehensive description, the reader is referred to general literature on (S)TEM [60], and specialized literature on 4D-STEM [61]. Here, only a short summary, without any claim for completeness, is given.

The formation of a diffraction pattern from electrons passing through a thin sample is possible due to the wave-like behavior of electrons. When a beam of electrons (or even a single electron) is focused onto a sample, electrons scatter when interacting with the crystal lattice. From scattering centers, an electron's probability distribution propagates in a wave-like manner in all directions. The periodic arrangement of atoms in a crystal lattice leads to constructive interference in the directions fulfilling the Bragg condition and a diffraction pattern can be recorded. From the diffraction pattern, one can obtain the crystal structure of a material, a crystallite's orientation in 3D space, and even internal stresses from variations in the lattice spacing.

A common method of utilizing electron diffraction in material characterization is selected area electron diffraction (SAED). Inside the TEM, an aperture is used to select

an area inside a single grain and a parallel beam of electrons illuminates this area. A spot pattern is then collected from the diffracted beam, allowing the determination of the crystal structure and the crystallographic orientation of that grain. While SAED interacts with larger areas of a sample, there are several methods utilizing decreased spot sizes and interaction volumes, most commonly convergent beam electron diffraction (CBED), nanobeam electron diffraction (NBED), and precession electron diffraction (PED). In CBED the electron beam converges to a spot size in the low nm range with a convergence angle in the range of tens of milliradian, producing detailed diffraction patterns ideal for detailed analysis. NBED uses finely focused electron beams with very small convergence angles, sometimes described as parallel beams, resulting in sharp diffraction patterns from small areas, which is ideal for high-resolution mapping of crystallographic information. PED can improve the quality of the resulting patterns by introducing a precessing motion of the beam around the optical axis, averaging out dynamical diffraction effects, with the downside of increased acquisition times.

4D-STEM derives its name from recording a two-dimensional diffraction pattern over a two-dimensional grid across the sample. The electron beam is rastered over a pattern over a sample, recording a diffraction pattern at each spot. The development of direct electron detectors has allowed for fast acquisition times, making this a feasible method. The recorded patterns allow for the generation of maps containing information about crystallographic orientations and different phases. Advanced automated data processing even enables the calculation of internal strain and stress fields inside a sample, making 4D-STEM a versatile and powerful method.

Specialized sample holders and actuators allow the in-situ straining of samples inside a TEM. In combination with 4D-STEM, this has led to fascinating results, such as the mapping of the strain field around a notch tip [62], or even the mapping of strain fields around individual dislocations [63].

1.7 References

[1] T. Li, Z. Y. Huang, Z. C. Xi, S. P. Lacour, S. Wagner, and Z. Suo. Delocalizing strain in a thin metal film on a polymer substrate. *Mech. Mater.*, 37(2):261–273, February 2005. ISSN 0167-6636. URL http://doi.org/10.1016/j.mechmat.2004.02.002.

[2] N. Lu, X. Wang, Z. Suo, and J. Vlassak. Failure by simultaneous grain growth, strain localization, and interface debonding in metal films on polymer substrates. *J. Mater. Res.*, 24(2):379–385, February 2009. ISSN 2044-5326. URL http://doi.org/10.1557/JMR.2009.0048.

[3] X. Luo, B. Zhang, and G. Zhang. Fatigue of metals at nanoscale: Metal thin films and conductive interconnects for flexible device application. *Nano Mater. Sci.*, 1(3):198–207, September 2019. ISSN 2589-9651. URL http://doi.org/10.1016/j.nanoms.2019.02.003.

[4] G.-D. Sim, Y.-S. Lee, S.-B. Lee, and J. J. Vlassak. Effects of stretching and cycling on the fatigue behavior of polymer-supported Ag thin films. *Mater. Sci. Eng., A*, 575:86–93, July 2013. ISSN 0921-5093. URL http://doi.org/10.1016/j.msea.2013.03.043.

[5] R. Schwaiger and O. Kraft. Size effects in the fatigue behavior of thin Ag films. *Acta Mater.*, 51(1):195–206, January 2003. ISSN 1359-6454. URL http://doi.org/10.1016/S1359-6454(02)00391-9.

[6] B.-J. Kim, H.-A.-S. Shin, J.-H. Lee, and Y.-C. Joo. Effect of cyclic outer and inner bending on the fatigue behavior of a multi-layer metal film on a polymer substrate. *Jpn. J. Appl. Phys.*, 55(6S3):06JF01, May 2016. ISSN 1347-4065. URL http://doi.org/10.7567/JJAP.55.06JF01.

[7] D. Wang, P. A. Gruber, C. A. Volkert, and O. Kraft. Influences of Ta passivation layers on the fatigue behavior of thin Cu films. *Mater. Sci. Eng., A*, 610:33–38, July 2014. ISSN 0921-5093. URL http://doi.org/10.1016/j.msea.2014.05.024.

[8] O. Glushko, A. Klug, E. J. W. List-Kratochvil, and M. J. Cordill. Monotonic and cyclic mechanical reliability of metallization lines on polymer substrates. *J. Mater. Res.*, 32(9):1760–1769, May 2017. ISSN 2044-5326. URL http://doi.org/10.1557/jmr.2017.121.

[9] B.-J. Kim, H.-A.-S. Shin, J.-H. Lee, T.-Y. Yang, T. Haas, P. Gruber, I.-S. Choi, O. Kraft, and Y.-C. Joo. Effect of film thickness on the stretchability and fatigue resistance of Cu films on polymer substrates. *J. Mater. Res.*, 29(23):2827–2834, December 2014. ISSN 0884-2914. URL http://doi.org/10.1557/jmr.2014.339.

[10] O. Glushko and D. Kiener. Initiation of fatigue damage in ultrafine grained metal films. *Acta Mater.*, 206:116599, March 2021. ISSN 1359-6454. URL http://doi.org/10.1016/j.actamat.2020.116599.

[11] J. Ma, X. Liu, R. Wang, C. Lu, X. Wen, and G. Tu. Research Progress and Application of Polyimide-Based Nanocomposites. *Nanomaterials*, 13(4):656, February 2023. ISSN 2079-4991. URL http://doi.org/10.3390/nano13040656.

[12] A. Sezer Hicyilmaz and A. Celik Bedeloglu. Applications of polyimide coatings: a review. *SN Appl. Sci.*, 3(3):1–22, March 2021. ISSN 2523-3971. URL http://doi.org/10.1007/s42452-021-04362-5.

[13] P. Ma, C. Dai, H. Wang, Z. Li, H. Liu, W. Li, and C. Yang. A review on high temperature resistant polyimide films: Heterocyclic structures and nanocomposites. *Compos. Commun.*, 16:84–93, December 2019. ISSN 2452-2139. URL http://doi.org/10.1016/j.coco.2019.08.011.

[14] J. Lin, J. Su, M. Weng, W. Xu, J. Huang, T. Fan, Y. Liu, and Y. Min. Applications of flexible polyimide: barrier material, sensor material, and functional material. 2023.

[15] D.-J. Liaw, K.-L. Wang, Y.-C. Huang, K.-R. Lee, J.-Y. Lai, and C.-S. Ha. Advanced polyimide materials: Syntheses, physical properties and applications. *Prog. Polym. Sci.*, 37(7):907–974, July 2012. ISSN 0079-6700. URL http://doi.org/10.1016/j.progpolymsci.2012.02.005.

[16] M. T. Bogert and R. R. Renshaw. 4-AMINO-0-PHTHALIC ACID AND SOME OF ITS DERIVATIVES.1. *J. Am. Chem. Soc.*, 30(7):1135–1144, July 1908. ISSN 0002-7863. URL http://doi.org/10.1021/ja01949a012.

[17] Y. Ding, H. Hou, Y. Zhao, Z. Zhu, and H. Fong. Electrospun polyimide nanofibers and their applications. *Prog. Polym. Sci.*, 61:67–103, October 2016. ISSN 0079-6700. URL http://doi.org/10.1016/j.progpolymsci.2016.06.006.

[18] M. Hasegawa and K. Horie. Photophysics, photochemistry, and optical properties of polyimides. *Prog. Polym. Sci.*, 26(2):259–335, March 2001. ISSN 0079-6700. URL http://doi.org/10.1016/S0079-6700(00)00042-3.

[19] L. Ube Industries. Upilex Grades. https://www.ube.com/upilex/en/upilex_grade.html, 2023. Accessed: 2023-10-18.

[20] Y.-H. Kim, J. Kim, G. F. Walker, C. Feger, and S. P. Kowalczyk. Adhesion and interface investigation of polyimide on metals. *J. Adhes. Sci. Technol.*, January 1988. URL https://www.tandfonline.com/doi/abs/10.1163/156856188X00101.

[21] J. G. Jinkins and R. E. Davis. Auger analysis of chromium films evaporated on polyimide. *J. Vac. Sci. Technol., A*, 11(4):1056–1060, July 1993. ISSN 0734-2101. URL http://doi.org/10.1116/1.578441.

[22] E. Preiß. *Fracture Toughness of Freestanding Metallic Thin Films Studied by Bulge Testing*. FAU University Press, 2018. ISBN 978-3-96147-118-8. URL http://doi.org/10.25593/978-3-96147-118-8.

[23] G.-D. Sim, Y. Hwangbo, H.-H. Kim, S.-B. Lee, and J. J. Vlassak. Fatigue of polymer-supported Ag thin films. *Scr. Mater.*, 66(11):915–918, June 2012. ISSN 1359-6462. URL http://doi.org/10.1016/j.scriptamat.2012.02.030.

[24] A. Dupré. *Théorie mécanique de la chaleur*. Gauthier-Villars, 1869.

[25] J. F. Friedrich. *Metal-Polymer Systems: Interface Design and Chemical Bonding*. Wiley-VCH, Weinheim, 2017. ISBN 978-3-527-33677-7.

[26] T. Strunskus, M. Grunze, G. Kochendoerfer, and Ch. Wöll. Identification of Physical and Chemical Interaction Mechanisms for the Metals Gold, Silver, Copper, Palladium, Chromium, and Potassium with Polyimide Surfaces. *Langmuir*, 12(11):2712–2725, January 1996. ISSN 0743-7463. URL http://doi.org/10.1021/la950125v.

[27] T. Strunskus, M. Kiene, R. Willecke, A. Thran, C. V. Bechtolsheim, and F. Faupel. Chemistry, diffusion and cluster formation at metal-polymer interfaces. *Mater. Corros.*, 49(3):180–188, March 1998. ISSN 0947-5117. URL http://doi.org/10.1002/(SICI)1521-4176(199803)49:3<180::AID-MACO180>3.0.CO;2-L.

[28] W.-J. Lee, Y.-S. Lee, S.-K. Rha, Y.-J. Lee, K.-Y. Lim, Y.-D. Chung, and C.-N. Whang. Adhesion and interface chemical reactions of Cu/polyimide and Cu/TiN by XPS. *Appl. Surf. Sci.*, 205(1):128–136, January 2003. ISSN 0169-4332. URL http://doi.org/10.1016/S0169-4332(02)01016-4.

[29] A. R. Rossi, P. N. Sanda, B. D. Silverman, and P. S. Ho. A theoretical study of the bonding and XPS spectra of chromium interacting with a polyimide model compound. *Organometallics*, 6(3):580–585, March 1987. ISSN 0276-7333. URL http://doi.org/10.1021/om00146a024.

[30] R. Haight, B. D. Silverman, R. C. White, P. S. Ho, and A. R. Rossi. XPS Studies of Chromium Atoms Interacting with a PMDA-ODA Polyimide Surface. *MRS Online Proc. Libr.*, 108(1):233–240, December 1987. ISSN 1946-4274. URL http://doi.org/10.1557/PROC-108-233.

[31] M. J. Goldberg, J. G. Clabes, A. Viehbeck, and C. A. Kovac. Chromium-Polyimide Interface Chemistry. *MRS Online Proc. Libr.*, 108(1):225–232, December 1987. ISSN 1946-4274. URL http://doi.org/10.1557/PROC-108-225.

[32] A. Selmani, A. Ouhlal, and A. Yelon. Density Functional Calculations on the Metal-Polymer Interfaces. *MRS Online Proc. Libr.*, 304(1):71–81, December 1993. ISSN 1946-4274. URL http://doi.org/10.1557/PROC-304-71.

[33] M. Nandi and A. Sen. Chemical basis for adhesion. Interaction of chromium with polyimide: model studies. *Chem. Mater.*, 1(3):291–292, May 1989. ISSN 0897-4756. URL http://doi.org/10.1021/cm00003a003.

[34] A. Chenite, A. Selmani, B. Lamontagne, and A. Yelon. Interfacial reactions between aluminum and BPDA-PDA. *J. Vac. Sci. Technol., A*, 11(5):2411–2418, September 1993. ISSN 0734-2101. URL http://doi.org/10.1116/1.578586.

[35] J. J. Pireaux, M. Vermeersch, C. Grégoire, P. A. Thiry, R. Caudano, and T. C. Clarke. The aluminum–polyimide interface: An electron-induced vibrational spectroscopy approach. *J. Chem. Phys.*, 88(5):3353–3362, March 1988. ISSN 0021-9606. URL http://doi.org/10.1063/1.453930.

[36] P. Hofmann. *Solid State Physics: An Introduction*. Wiley-VCH, Weinheim, Germany, November 2008. ISBN 978-3-52740861-0. URL https://www.amazon.com/-/de/Solid-State-Physics-Philip-Hofmann/dp/3527408614.

[37] J. Bardeen, L. N. Cooper, and J. R. Schrieffer. Theory of Superconductivity. *Phys. Rev.*, 108(5):1175–1204, December 1957. ISSN 1536-6065. URL http://doi.org/10.1103/PhysRev.108.1175.

[38] P. V. Andrews, M. B. West, and C. R. Robeson. The effect of grain boundaries on the electrical resistivity of polycrystalline copper and aluminium. *Philos. Mag.*, May 1969. URL https://www.tandfonline.com/doi/abs/10.1080/14786436908225855.

[39] I. Bakonyi, V. A. Isnaini, T. Kolonits, Zs. Czigány, J. Gubicza, L. K. Varga, E. Tóth-Kádár, L. Pogány, L. Péter, and H. Ebert. The specific grain-boundary electrical resistivity of Ni. *Philos. Mag.*, May 2019. URL https://www.tandfonline.com/doi/full/10.1080/14786435.2019.1580399.

[40] I. Bakonyi. Accounting for the resistivity contribution of grain boundaries in metals: critical analysis of reported experimental and theoretical data for Ni and Cu. *Eur. Phys. J. Plus*, 136(4):1–48, April 2021. ISSN 2190-5444. URL http://doi.org/10.1140/epjp/s13360-021-01303-4.

[41] O. Glushko, P. Kraker, and M. J. Cordill. Explicit relationship between electrical and topological degradation of polymer-supported metal films subjected to mechanical loading. *Appl. Phys. Lett.*, 110(19), May 2017. ISSN 0003-6951. URL http://doi.org/10.1063/1.4982802.

[42] H.-L. Chen, X.-M. Luo, D. Wang, P. Schaaf, and G.-P. Zhang. Achieving very high cycle fatigue performance of Au thin films for flexible electronic applications. *J. Mater. Sci. Technol.*, 89:107–113, October 2021. ISSN 1005-0302. URL http://doi.org/10.1016/j.jmst.2021.02.025.

[43] Y.-S. Lee, G.-D. Sim, J.-S. Bae, J.-Y. Kim, and S.-B. Lee. Tensile and fatigue behavior of polymer supported silver thin films at elevated temperatures. *Mater. Lett.*, 193:81–84, April 2017. ISSN 0167-577X. URL http://doi.org/10.1016/j.matlet.2017.01.111.

[44] H. Y. Wan, X. M. Luo, X. Li, W. Liu, and G. P. Zhang. Nanotwin-enhanced fatigue resistance of ultrathin Ag films for flexible electronics applications. *Mater. Sci. Eng., A*, 676:421–426, October 2016. ISSN 0921-5093. URL http://doi.org/10.1016/j.msea.2016.09.010.

[45] X. M. Luo and G. P. Zhang. Grain boundary instability dependent fatigue damage behavior in nanoscale gold films on flexible substrates. *Mater. Sci. Eng., A*, 702:81–86, August 2017. ISSN 0921-5093. URL http://doi.org/10.1016/j.msea.2017.07.006.

[46] L. Gence, M. Escalona, C. Castillo, F. Quero, P. Saikia, R. Wheatley, D. E. Diaz-Droguett, M. J. Retamal, U. G. Volkmann, and H. Bhuyan. Wrinkled titanium nitride nanocomposite for robust bendable electrodes. *Nanotechnology*, 30(49):495705, September 2019. ISSN 0957-4484. URL http://doi.org/10.1088/1361-6528/ab416c.

[47] I. M. Graz, D. P. J. Cotton, and S. P. Lacour. Extended cyclic uniaxial loading of stretchable gold thin-films on elastomeric substrates. *Appl. Phys. Lett.*, 94(7), February 2009. ISSN 0003-6951. URL http://doi.org/10.1063/1.3076103.

[48] J. Cheng and Z. Li. An electrical resistance degradation model for thin film under fatigue loading. *Fatigue Fract. Eng. Mater. Struct.*, 43(11):2582–2596, November 2020. ISSN 8756-758X. URL http://doi.org/10.1111/ffe.13278.

[49] B.-J. Kim, H.-A.-S. Shin, S.-Y. Jung, Y. Cho, O. Kraft, I.-S. Choi, and Y.-C. Joo. Crack nucleation during mechanical fatigue in thin metal films on flexible substrates. *Acta Mater.*, 61(9):3473–3481, May 2013. ISSN 1359-6454. URL http://doi.org/10.1016/j.actamat.2013.02.041.

[50] R. O. Ritchie. Mechanisms of fatigue-crack propagation in ductile and brittle solids. *Int. J. Fract.*, 100(1):55–83, November 1999. ISSN 1573-2673. URL http://doi.org/10.1023/A:1018655917051.

[51] E. O. Hall. The Deformation and Ageing of Mild Steel: III Discussion of Results. *Proc. Phys. Soc. B*, 64(9):747, September 1951. ISSN 0370-1301. URL http://doi.org/10.1088/0370-1301/64/9/303.

[52] J. Petch N. The cleavage strength of polycrystals. *J. Iron Steel Inst*, 174:25–28, 1953.

[53] J. P. Lucas and W. W. Gerberich. A Proposed Criterion for Fatigue Threshold: Dislocation Substructure Approach. *Fatigue Fract. Eng. Mater. Struct.*, 6(3):271–280, January 1983. ISSN 8756-758X. URL http://doi.org/10.1111/j.1460-2695.1983.tb00342.x.

[54] M. J. Cordill, P. Kreiml, T. Jörg, S. Zak, and C. Mitterer. Parameters influencing the fracture of Mo films and their wider significance. *MRS Adv.*, 8(19):1061–1067, November 2023. ISSN 2059-8521. URL http://doi.org/10.1557/s43580-023-00612-3.

[55] C. Cao, B. Chen, T. Filleter, and Y. Sun. Mechanical characterization of thin films using a MEMS device inside SEM. In *2015 28th IEEE International Conference on Micro Electro Mechanical Systems (MEMS)*, pages 381–384. 2015. URL http://doi.org/10.1109/MEMSYS.2015.7050969.

[56] A. Barrios, C. Kunka, J. Nogan, K. Hattar, and B. L. Boyce. Automated High-Throughput Fatigue Testing of Freestanding Thin Films. *Small Methods*, 7(7):2201591, July 2023. ISSN 2366-9608. URL http://doi.org/10.1002/smtd.202201591.

[57] L. Sun, T. Xu, and Z. Zhang. *In-Situ Transmission Electron Microscopy*. Springer, Singapore, February 2023. ISBN 978-981-196844-0.

[58] C. M. Barr, T. Duong, D. C. Bufford, Z. Milne, A. Molkeri, N. M. Heckman, D. P. Adams, A. Srivastava, K. Hattar, M. J. Demkowicz, and B. L. Boyce. Autonomous healing of fatigue cracks via cold welding. *Nature*, 620:552–556, August 2023. ISSN 1476-4687. URL http://doi.org/10.1038/s41586-023-06223-0.

[59] T. Kondo, A. Shin, M. Akasaka, H. Hirakata, and K. Minoshima. Vacuum effects on fatigue crack growth in submicrometre-thick freestanding copper films. *Fatigue Fract. Eng. Mater. Struct.*, 42(5):1118–1129, May 2019. ISSN 8756-758X. URL http://doi.org/10.1111/ffe.12976.

[60] C. B. Carter and D. B. Williams. *Transmission Electron Microscopy: Diffraction, Imaging, and Spectrometry*. Springer, September 2016. ISBN 978-3-31926649-7.

[61] C. Ophus. Four-Dimensional Scanning Transmission Electron Microscopy (4D-STEM): From Scanning Nanodiffraction to Ptychography and Beyond. *Microsc. Microanal.*, 25(3):563–582, June 2019. ISSN 1431-9276. URL http://doi.org/10.1017/S1431927619000497.

[62] C. Gammer and D. An. Conditions near a crack tip: Advanced experiments for dislocation analysis and local strain measurement. *MRS Bull.*, 47(8):808–815, 2022. ISSN 0883-7694. URL http://doi.org/10.1557/s43577-022-00377-4.

[63] C. Gammer, I. Issa, A. Minor, R. Ritchie, and D. Kiener. Strain Field Around Individual Dislocations Controls Failure. *Small Methods*, September 2024. URL http://doi.org/10.1002/smtd.202400654.

2

Linking through-thickness cracks in metallic thin films to in-situ electrical resistance peak broadening

David D. Gebhart[a], Anna Krapf[b], Christoph Gammer[a], Benoit Merle[b], Megan J. Cordill[a],

[a] Erich Schmid Institute of Materials Science, Austrian Academy of Sciences, Jahnstrasse 12, 8700 Leoben, Austria
[b] Department of Materials Science & Engineering, Institute 1, University of Erlangen-Nürnberg (FAU), Martensstrasse 5, 91058 Erlangen, Germany

This chapter is reprinted from the article: D. D. Gebhart, A. Krapf, C. Gammer, B. Merle, and M. J. Cordill. Linking through-thickness cracks in metallic thin films to in-situ electrical resistance peak broadening. *Scr. Mater.*, 212:114550, 2022. ISSN 1359-6462. https://doi.org/10.1016/j.scriptamat.2022.114550.

Contents

Abstract

Measurements of electrical resistance have been used extensively as a failure criterion in cyclically loaded conductive films. However, not much research has been performed on extracting additional information contained within such resistance data sets. This

study shows that an increase in peak width evidences a transition from cracks bridging to through-thickness crack formation. A Au/Cr bilayer system on a polyimide substrate is used for data generation but the method is applicable to any material system where both necking and through-thickness cracks are formed and no immediate formation of electrically insulating oxide layers occurs upon damage initiation. The method is easy to implement, and has the ability to replace time-intensive and destructive inspection methods.

2.1 Introduction

Electrically conductive metal coatings are an integral part in a wide variety of applications. Carrying either signals or power, they are present in an abundance of electronic devices and applications, such as sensors, microelectromechanical systems (MEMS), display technology applications, and photovoltaic cells. Many of those applications involve bending and stretching, where mechanical or thermomechanical strain is introduced into the system. As the failure of a single electrical connection can lead to failure of the whole device, we need to understand their cyclic behaviour and fracture mechanisms in order to create long lasting devices. A well established method to investigate such failures is performing in-situ electrical resistance measurements while cyclic tensile or bending loads are applied to the system. Such investigations have been carried out for a wide variety of systems, such as Ag [1, 2, 3], Cu [4, 5, 6], Al [5], Au [7], Au/Ti [8], and Mo/W [9] on polymer substrates.

Most studies are concerned with the optimization of fatigue lifetimes of different material systems and use an increase in electrical resistance only as a failure criterion [1, 2, 3, 4, 5, 6, 7, 8, 9] and very little analysis has been performed to extract further information contained within resistance data. Gence et al. [10] used resistance curve amplitude and curve minima evolution, as well as curve shape continuity, in bending tests to argue robustness of TiN-Ag nanowire nanocomposite coatings. Other studies have discovered a double resistance peak in conductive coatings [11, 12] which has been found by Graz et al. [12] to be caused by lateral contraction and closure of cracks that have formed parallel to the load direction.

While some system parameters, such as mean grain size, will have a small influence on the electrical resistivity of a conducting material [13], larger changes in conducting film electrical resistance are mostly a function of crack length and crack density in the film. An empirical model was found from finite element simulations, giving the relation

of electrical resistance and the (square) product of crack density and crack length (with cracks perpendicular to straining direction) [14]:

$$\frac{R}{R_0} = 1 + \frac{C_l l_0}{\sqrt{2}} + \frac{C_l^2 l_0^2}{2} \tag{2.1}$$

with resistance R, initial resistance R_0, linear crack density C_l, and average crack length l_0. Crack length and crack density cannot be separated within single direct current resistance data points. However, thorough analysis of ensembles of electrical resistance data points could bring more insights.

This work analyzes full width at half maximum (FWHM) values of resistance peaks measured during cyclic uniaxial loading. Fig. 2.1 gives an overview of the analyzed data for one randomly chosen measurement series. All collected data points are shown in Fig. 2.1 (a), an enlarged region of 10 cycles is given in (b), and (c) presents only one cycle. Here, the FWHM is measured from the linear interpolated data at approximately 0.5 cycle durations. A material system of 160 nm Au on polyimide, with a 50 nm Cr interlayer, was used. Au is a face centered cubic (fcc) metal that shows rather ductile fracture properties, while the body centered cubic (bcc) metal Cr behaves more brittle and has a lower fracture strain than Au [15]. In such a system, cracks first form in the brittle interlayer, they serve as stress concentration points, and induce damage in the ductile layer [15, 16, 17]. The system is of scientific interest because Au shows good properties and robustness as an electrical conductor and the Cr interlayer critically improves adhesion to the polymer substrate. It has been shown that monotonic straining of similar material systems first leads to localized necking in the ductile fcc metal film at interlayer-induced stress concentration points, before through-thickness cracks (TTCs) form [18, 19]. Differentiating between TTCs and necking is widely acknowledged as challenging, even with the usual microscopy methods [20].

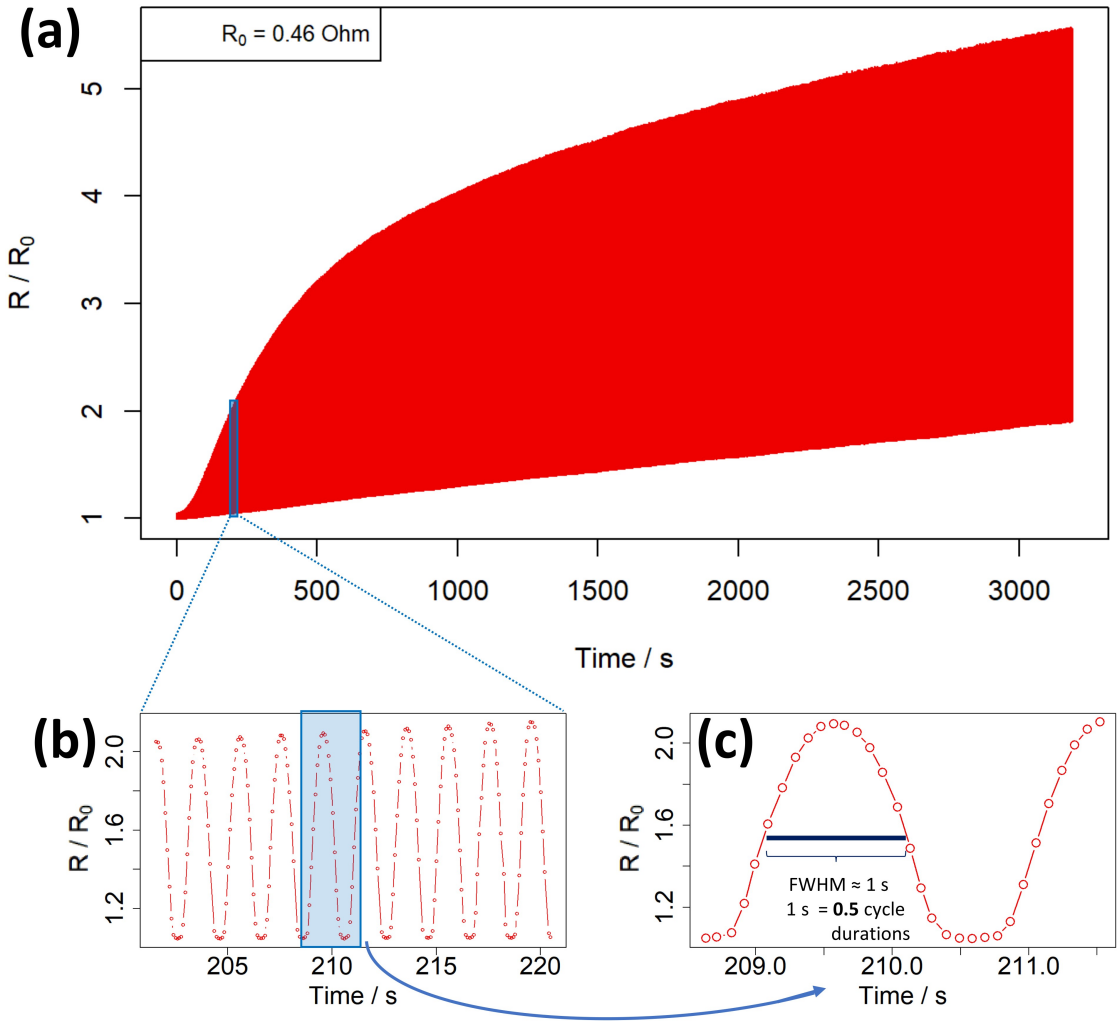

Figure 2.1: One measurement series - overview of acquired data: (a) All collected data points, (b) an enlarged region of 10 cycles, and (c) only one cycle with a FWHM value of approximately 0.5 cycle durations.

The Cr and Au films were deposited onto a 50 × 50 mm^2 polyimide substrate of a thickness of 50 µm (Upilex-S; Ube Industries, Ltd.) with a custom-built thermal evaporation unit at a chamber pressure between 10^{-7} and 10^{-6} mbar. First, a 50 nm Cr layer was deposited at a rate of 0.4 - 0.5 Å/s and a substrate temperature of 150 °C. On top of this layer, a 160 nm Au layer was deposited at a rate of around 1 Å/s and a substrate temperature of 80 °C. Deposition rates and thicknesses were measured with a quartz crystal oscillator and the substrate temperature was measured with a thermocouple positioned close to the substrate. The sample was rotated at 10 rpm during evaporation. The mean grain diameter of the deposited gold film was determined to

be 129 nm with electron backscatter diffraction measurements and (111) texture was observed. After deposition, the sheet was cut into 6 × 25 mm^2 rectangles, using a Cricut Explore Air 2 (Cricut, Inc.). The samples were cyclically loaded under strain control using a Tytron 250 Microforce Testing System (MTS Systems). A sinusoidal load was applied at a frequency of 0.5 Hz, 2 % peak strain, and non-zero minima strain of 0.2 % to prevent sample buckling due to non-negligible plastic deformation of the polyimide substrate. The samples were fastened with a custom-built clamp made of a dielectric bottom and a metallic top section with two attached pins on each side, similar to [21], leaving a 6 × 15 mm^2 gauge section to be strained. The set-up was connected to a Keithley 2000 Multimeter for four-wire resistance measurements. The multimeter's power line cycle (PLC) was set to 1, with a 50 Hz line frequency, to suppress noise in the data. Automated data acquisition was performed using a Sparkfun GPIB-USB Controller (BOB-00549) and controlled by a Scilab script, achieving a sampling rate of around 10 samples s^{-1}. The microstructural characterization was performed by scanning electron microscopy (SEM, Zeiss LEO 1525) imaging of samples loaded to 2 % strain with a custom-built mechanical device with clamps similar to those used in cyclic straining. Focused ion beam (FIB) cross-sections were prepared with a Zeiss LEO 1540XB. To measure linear damage density and damage length, light microscopy images were used. It should be noted that damage has the appearance of cracks in micrographs but since not all apparent cracks penetrate the whole thickness of the film, they will be referred to as damage. For linear damage densities, the number of damage sites intersecting lines parallel to straining direction (at least 700 µm combined) was divided by the total length of all drawn lines. For damage length measurements, an area of 20 × 100 $µm^2$ (the smaller length being perpendicular to the loading direction) was taken and for all damage sites touching this area, their spread perpendicular to the straining direction was measured - the number of damage sites measured was ≥ 28 for all samples. The data was analyzed by a script written in the programming language *R*. For calculation of resistance FWHM values, the function *approxfun* was used to create linear interpolations between measured points. The x-distance between rising and falling interpolations was taken at their intersections with the value bisecting the previous minimum and the current peak maximum.

Fig. 2.2 (a) depicts linear damage density (red diamonds) and average damage length (blue triangles) up to 1600 cycles. The data sets (length and density) were constructed from different samples from the same deposition run. They were tested to a different number of cycles to avoid interrupting cycling to perform damage analysis. Most damage visible in the micrographs (shown in Fig. 2.2 (b) and (c)) occurs at very low cycle numbers, below 50. For both damage density and damage length, the increase between cycles 50 - 100 is approximately an order of magnitude smaller than the initial increase up to cycle 50.

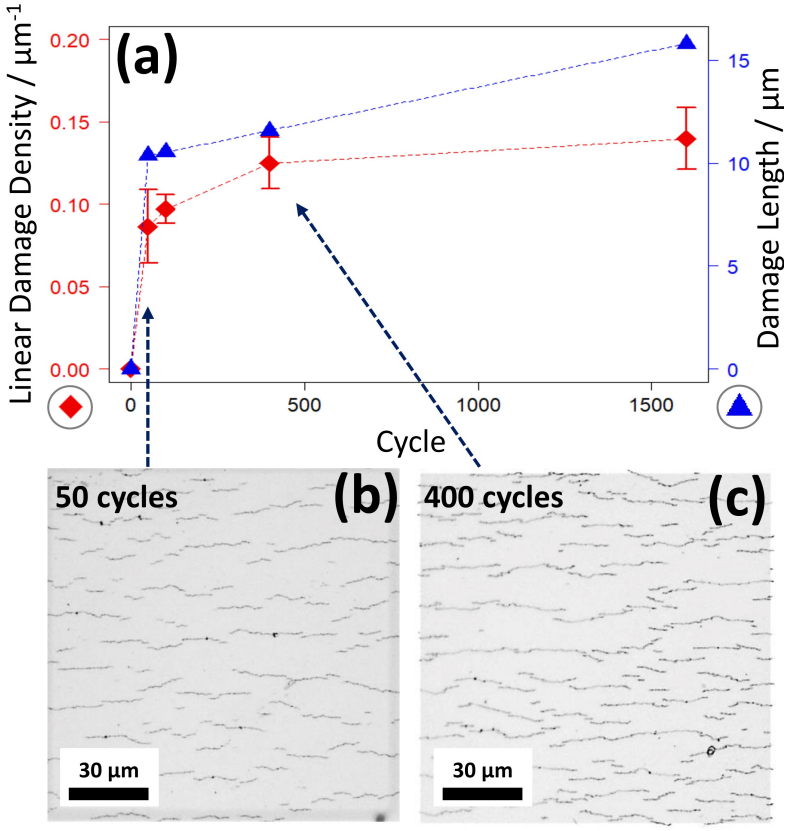

Figure 2.2: (a) Linear damage density (red diamonds) and average damage length (blue triangles; note: no clear unimodal distribution - no width of distribution given in plot). Micrographs after (b) 50 and (c) 400 applied strain cycles.

Fig. 3.6 (a) shows the maximal resistance for each individual cycle up to cycle 1600, given as a mean with one sample standard deviation, taken from four measurement series and normalized to each sample's initial resistance R_0. The increase in average resistance (local slope of the solid black curve) is reaching a maximum after cycle 50, while the damage density and length have already started to level off at that point (compare Fig. 2.2 (a) with Fig. 3.6 (a)). Resistance maxima even continue to increase linearly up to around cycle 300 (see Fig. 3.6 (a)). The delayed increase of the resistance compared to the crack density and length could be an indication that the early damage visible in micrographs does not immediately extend through the whole film thickness and TTCs only develop with further cycling. For TTCs, Eq. 2.1 predicts larger resistance values than measured for early cycles and smaller values for later cycles. At cycle 50 it would yield a value of 2.2 R_0, larger than the measured peak value of 1.3 R_0, and only at cycle 400 would it drop below the measured value of 4.9 R_0, with a model value of 3.1 R_0. Note that the model assumes all cracks to be of the exact same length and might underestimate the

electrical resistance compared to a realistic, wider distribution. However, the model still shows an earlier increase in resistance than the measurements. This is a clear indication that a process of damage propagation is happening which cannot be captured by surface micrographs. One such process would be the evolution of surface cracks (necking) to TTCs.

The data also features a distinct and highly repeatable broadening of resistance peaks with increasing cycle numbers. This is shown in the plot of full width at half maximum (FWHM) values in Fig. 3.6 (b), with a value of 1 representing a full cycle duration. The data depicted comes from the same four measurement series shown in Fig. 3.6 (a). As a reference, note that a perfect sinusoidal curve would show a FWHM value of 0.5 cycle durations. As can be seen in Fig. 3.6 (c) and (d), early resistance peaks are narrower than the strain peaks while later peaks are broader. The strain signal remains sinusoidal in either case, exhibiting a constant FWHM value of 0.5.

The initial drop in electrical FWHM values can be correlated to the extensive damage formation and propagation visible in the micrographs up to cycle 50 (see Fig. 2.2). The decrease in FWHM is an indication that this damage is formed around strain maxima, because this leads to a spike in resistance centered around strain maxima, thus making the peaks more pointed and narrow. Please note that it was confirmed by SEM micrographs taken after 5 and 10 cycles (not shown here) that most damage in the Au layer does not form immediately during the very first cycles but rather there is continuous damage formation and propagation at early cycle numbers.

After the initial decrease, the FWHM plot shows similar trends as the peak resistance values in Fig. 3.6 (a). Both show a maximum and almost constant slope between cycles 50 and 300 and both start to level off with further cycling. The FWHM values are simply a measurement of how quickly electrical resistance rises within one cycle. With sinusoidal strain, a FWHM value greater than 0.5 means that the electrical resistance increases faster than the applied strain. The resistance peak of cycle 400 in Fig. 3.6 (d) shows a very steep increase at low strain values which then almost transitions to a plateau around the strain maximum. Cracks which have not propagated through the whole film thickness will include metallic bridging ligaments electrically connecting the crack faces. The electrical resistance of a sample is relative to the mean conductive cross-section between crack faces and a plateau in a resistance peak signifies that cracks are completely opened and that their conductive cross-sections are not further decreased with increasing strain (cracks/damage do not propagate further either through the film or laterally in-plane). The more electrically conductive bridges between crack faces break

during cycling, the more pronounced this plateau will become and the higher the FWHM value will be. With a reduction in conductive cross-section between crack faces, TTCs are forming and propagating which leads to a more complete crack opening at smaller strain values and increases the FWHM values. This means that a rise in FWHM values is a good indication of the formation of TTCs which can otherwise only be detected with extensive inspection methods, such as Focused Ion Beam (FIB) cross-sectioning.

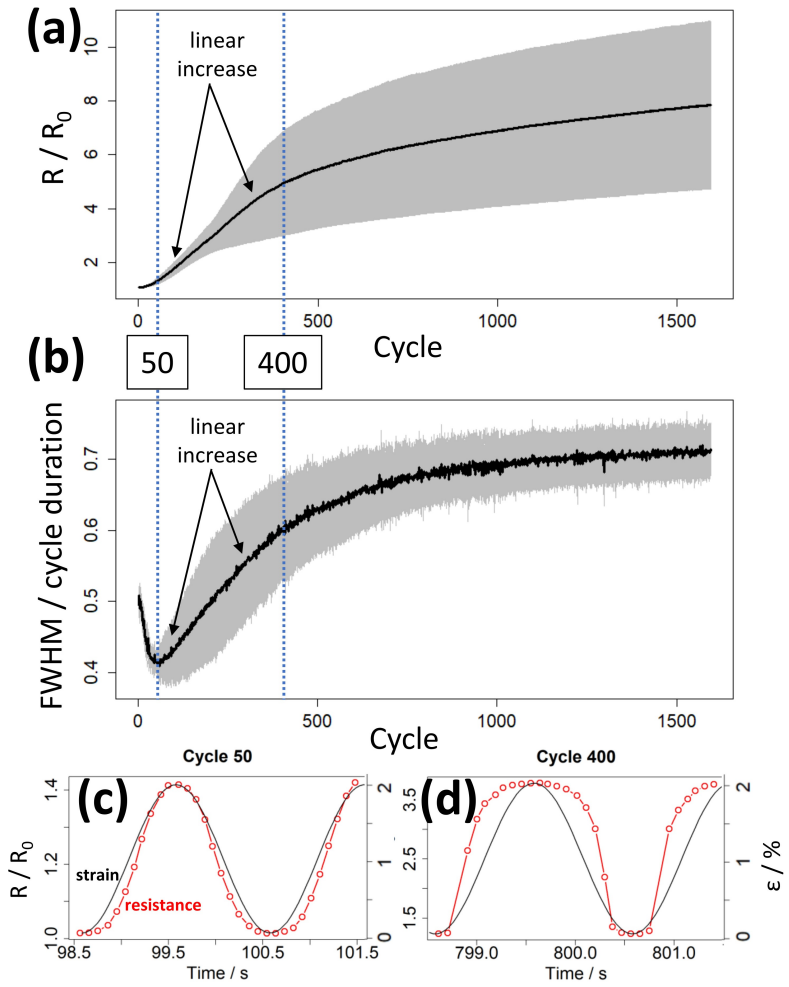

Figure 2.3: (a) Maxima resistance data points for each cycle normalized to initial resistance - mean ± 1 sample standard deviation (s) (4 measurement series). (b) Full width at half maximum for each cycle - mean ± 1 s (4 measurement series). Resistance peaks of one measurement series of cycles (c) 50 and (d) 400 in red with the sinusoidal strain curve overlayed in black.

To affirm the relation between FWHM and through-thickness cracking, SEM images of samples loaded to 2 % strain are depicted in Fig. 2.4. SEM images of FIB cross-sections of unloaded damage sites are presented in Fig. 2.5. It is confirmed that necking does occur, as it was observed in literature [15, 16, 17, 18, 19]. With damage growing both from the surface and the substrate, it can be assumed that the black center lines observed at higher cycle numbers in Fig. 2.4 are TTCs. After 50 cycles, no clear TTCs can be made out and large parts of the damage sites are surface cracks. Only after 100 cycles, some damage has evolved into TTCs. However, there still seem to be bridges at damage centers which are not opened at 2 % strain, leading to conductive pathways between crack faces (see inset on right side of Fig. 2.4) and damage fringes are mostly surface cracks (inset on left side of Fig. 2.4). Generally, many damage sites form during the first 100 cycles and significant proportions are not yet full TTCs at maximum strain. This is in line with a FWHM value of below 0.5 cycle durations at that range, which indicates pronounced damage propagation around strain maxima along with conductive pathways across damage sites at maximum strain. From cycle 100 to cycle 400, FWHM shows its maximum increase and rises from around 0.45 to 0.6 cycle durations, indicating further development of TTCs. This is also where most TTC formation is observed in SEM images. After 400 cycles, damage center regions show a pronounced black center line and even damage fringes have in large part become TTCs. With further loading to 1600 cycles, only slight changes can be observed - damage fringes have developed into TTCs up to the very tip of the damage sites, fitting a slower FWHM increase from 0.6 to 0.7 cycle durations and an onset of saturation (see Fig. 3.6 (b)). Here, the damage sites (now TTCs) are fully opened at the strain maximum and hardly any conductive pathways form when strain is slightly reduced, leading to almost constant electrical resistance around the strain maximum and steep resistance slopes at strain values where cracks open/close. This results in broad resistance peaks and a FWHM value well above 0.5 cycle durations.

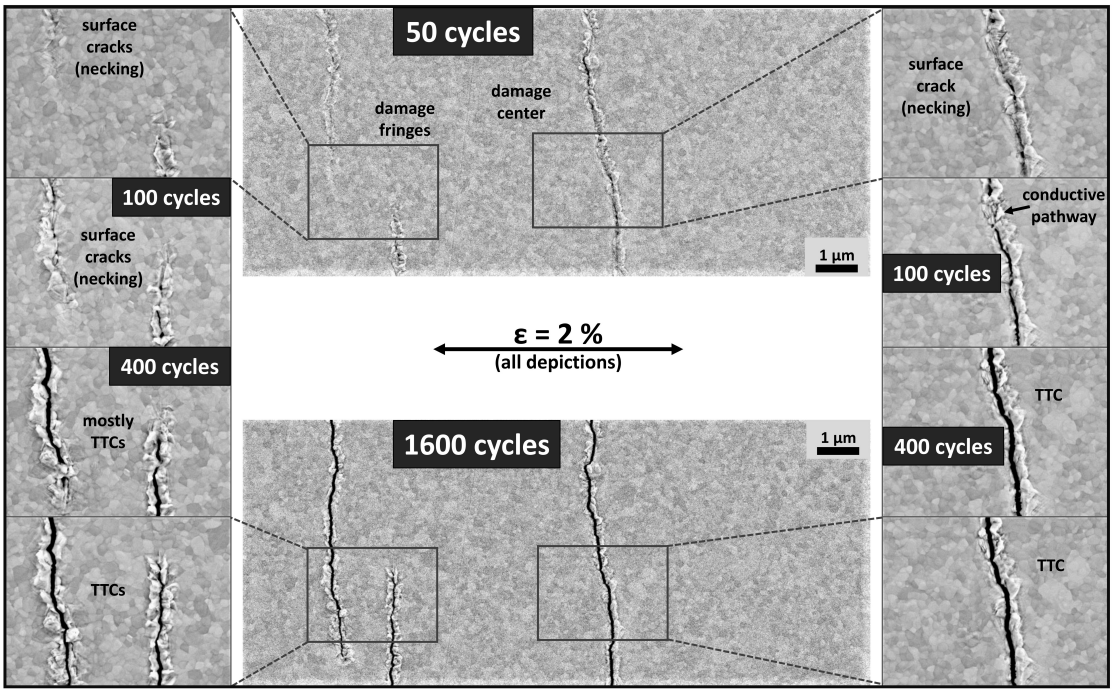

Figure 2.4: SEM images of the same sample region at 2 % strain (loaded) after 50, 100, 400, and 1600 applied strain cycles (top to bottom).

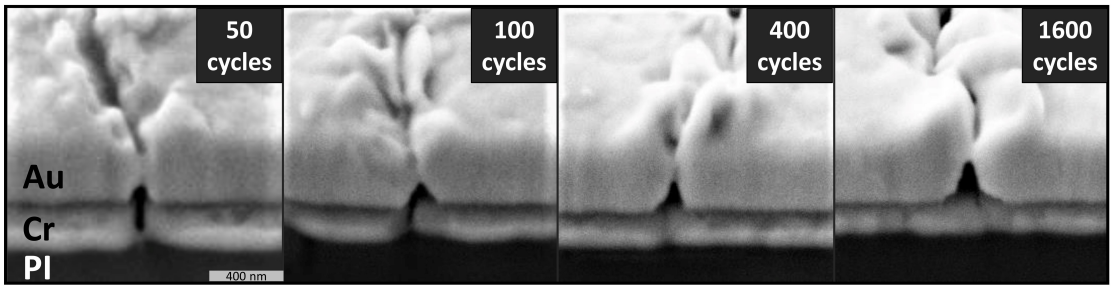

Figure 2.5: SEM images of FIB cross-sections at damage sites after 50, 100, 400, and 1600 applied strain cycles (unloaded). Imaged at a 36 ° angle (0 ° being in-plane) - scale bar only valid in x-dimension. Note: different damage sites imaged.

To the best of our knowledge, this is the first qualitative report on the importance of FWHM analysis in cyclic loading investigations. This new concept gives access to crack opening characteristics, which could so far not be tracked from using resistance maxima and minima. In addition to general measurements of increase in electrical resistance that describe the total amount of accumulated damage, peak widths can provide more

insight into the type of damage present in a sample, either TTC or necking. As a first demonstration, it was shown that FWHM values can be used to detect through-thickness cracks. With FWHM reflecting crack opening and closure properties within a loading cycle, such an analysis has a strong application potential to other investigations. The method is very simple to implement and with enough measurement precision, it could be applied to fatigue experiments in bulk materials, such as crack propagation in notched specimens, as well as more complex fracture mechanics investigations, such as crack closure in fatigue loading.

Funding: This work was supported by the Austrian Science Fund (FWF) [Project I 4913-N] and the German Research Foundation (DFG) [grant ME-4368/8] within the framework of the D-A-CH cooperation FATIFACE.

All data supporting the findings of this study is available from the corresponding author upon reasonable request.

2.2 References

[1] G.-D. Sim, Y.-S. Lee, S.-B. Lee, and J. J. Vlassak. Effects of stretching and cycling on the fatigue behavior of polymer-supported Ag thin films. *Mater. Sci. Eng. A*, 575:86–93, 2013. ISSN 0921-5093. URL http://doi.org/10.1016/j.msea.2013.03.043.

[2] H. Wan, X. Luo, X. Li, W. Liu, and G. Zhang. Nanotwin-enhanced fatigue resistance of ultrathin Ag films for flexible electronics applications. *Mater. Sci. Eng. A*, 676:421–426, 2016. ISSN 0921-5093. URL http://doi.org/10.1016/j.msea.2016.09.010.

[3] Y.-S. Lee, G.-D. Sim, J.-S. Bae, J.-Y. Kim, and S.-B. Lee. Tensile and fatigue behavior of polymer supported silver thin films at elevated temperatures. *Mater. Lett.*, 193:81–84, 2017. ISSN 0167-577X. URL http://doi.org/10.1016/j.matlet.2017.01.111.

[4] B.-J. Kim, H.-A.-S. Shin, J.-H. Lee, T.-Y. Yang, T. Haas, P. Gruber, I.-S. Choi, O. Kraft, and Y.-C. Joo. Effect of film thickness on the stretchability and fatigue resistance of Cu films on polymer substrates. *J. Mater. Res.*, 29(23):2827–2834, DEC 14 2014. ISSN 0884-2914. URL http://doi.org/10.1557/jmr.2014.339.

[5] X. J. Sun, C. C. Wang, J. Zhang, G. Liu, G. J. Zhang, X. D. Ding, G. P. Zhang, and J. Sun. Thickness dependent fatigue life at microcrack nucleation for metal thin films on flexible substrates. *J. Phys. D: Appl. Phys*, 41(19):195404, sep 2008. URL http://doi.org/10.1088/0022-3727/41/19/195404.

[6] J. Zhang, X. Zhang, G. Liu, R. Wang, G. Zhang, and J. Sun. Length scale dependent yield strength and fatigue behavior of nanocrystalline Cu thin films. *Mater. Sci. Eng. A*, 528(25):7774–7780, 2011. ISSN 0921-5093. URL http://doi.org/10.1016/j.msea.2011.06.083.

[7] X. Luo and G. Zhang. Grain boundary instability dependent fatigue damage behavior in nanoscale gold films on flexible substrates. *Mater. Sci. Eng. A*, 702:81–86, 2017. ISSN 0921-5093. URL http://doi.org/10.1016/j.msea.2017.07.006.

[8] H.-L. Chen, X.-M. Luo, D. Wang, P. Schaaf, and G.-P. Zhang. Achieving very high cycle fatigue performance of Au thin films for flexible electronic applications. *J Mater Sci Technol*, Apr 2021. URL http://doi.org/10.1016/j.jmst.2021.02.025.

[9] F. Wang, X.-M. Luo, D. Wang, P. Schaaf, and G.-P. Zhang. Fatigue behavior of nanoscale Mo/W multilayers on flexible substrates. *MRS Adv.*, 4:2309–2317, 9 2019. ISSN 2059-8521. URL http://doi.org/10.1557/adv.2019.252.

[10] L. Gence, M. Escalona, C. Castillo, F. Quero, P. Saikia, R. Wheatley, D. E. Diaz-Droguett, M. J. Retamal, U. G. Volkmann, and H. Bhuyan. Wrinkled titanium nitride nanocomposite for robust bendable electrodes. *Nanotechnology*, 30(49):495705, sep 2019. URL http://doi.org/10.1088/1361-6528/ab416c.

[11] C. Chambers, S. P. Lacour, S. Wagner, Z. Suo, and Z. Huang. Super-elastic Gold Conductors on Elastomeric Substrates. *MRS OPL*, Dec 2003. URL http://doi.org/10.1557/PROC-769-H10.3.

[12] I. M. Graz, D. P. J. Cotton, and S. P. Lacour. Extended cyclic uniaxial loading of stretchable gold thin-films on elastomeric substrates. *Appl. Phys. Lett.*, 94:071902, Feb 2009. URL http://doi.org/10.1063/1.3076103.

[13] J.-W. Lim and M. Isshiki. Electrical resistivity of Cu films deposited by ion beam deposition: Effects of grain size, impurities, and morphological defect. *J. Appl. Phys.*, 99(9):094909, 2006. URL http://doi.org/10.1063/1.2194247.

[14] O. Glushko, P. Kraker, and M. J. Cordill. Explicit relationship between electrical and topological degradation of polymer-supported metal films subjected to mechanical loading. *Appl. Phys. Lett.*, 110:191904, May 2017. URL http://doi.org/10.1063/1.4982802.

[15] B. Putz, R. L. Schoeppner, O. Glushko, D. F. Bahr, and M. J. Cordill. Improved electro-mechanical performance of gold films on polyimide without adhesion layers. *Scr. Mater.*, 102:23–26, 2015. ISSN 1359-6462. URL http://doi.org/10.1016/j.scriptamat.2015.02.005.

[16] M. J. Cordill, T. Jörg, D. M. Többens, and C. Mitterer. Improved fracture resistance of Cu/Mo bilayers with thickness tailoring. *Scr. Mater.*, 202:113994, 2021. ISSN 1359-6462. URL http://doi.org/10.1016/j.scriptamat.2021.113994.

[17] V. M. Marx, F. Toth, A. Wiesinger, J. Berger, C. Kirchlechner, M. J. Cordill, F. D. Fischer, F. G. Rammerstorfer, and G. Dehm. The influence of a brittle Cr interlayer on the deformation behavior of thin Cu films on flexible substrates: Experiment and model. *Acta Mater.*, 89:278–289, 2015. ISSN 1359-6454. URL http://doi.org/10.1016/j.actamat.2015.01.047.

[18] M. J. Cordill and V. M. Marx. Fragmentation testing for ductile thin films on polymer substrates. *Philos. Mag. Lett.*, 93(11):618–624, 2013. URL http://doi.org/10.1080/09500839.2013.830792.

[19] P. Kreiml, M. Rausch, V. L. Terziyska, H. Köstenbauer, J. Winkler, C. Mitterer, and M. J. Cordill. Electro-mechanical behavior of Al/Mo bilayers studied with in situ straining methods. *Thin Solid Films*, 665:131–136, 2018. ISSN 0040-6090. URL http://doi.org/10.1016/j.tsf.2018.07.054.

[20] O. Glushko, B. Putz, and M. Cordill. Determining effective crack lengths from electrical measurements in polymer-supported thin films. *Thin Solid Films*, 699:137906, Apr 2020. ISSN 00406090. URL http://doi.org/10.1016/j.tsf.2020.137906.

[21] O. Glushko and M. J. Cordill. Electrical Resistance of Metal Films on Polymer Substrates Under Tension. *Exp. Tech.*, 40(1):303–310, Feb 2016. ISSN 0732-8818, 1747-1567. URL http://doi.org/10.1007/s40799-016-0040-x.

3

Describing Mechanical Damage Evolution through in-situ Electrical Resistance Measurements

David D. Gebhart[a], Anna Krapf[b], Benoit Merle[c], Christoph Gammer[a], Megan J. Cordill[a],

[a] Erich Schmid Institute of Materials Science, Austrian Academy of Sciences, Jahnstrasse 12, 8700 Leoben, Austria
[b] Department of Materials Science & Engineering, Institute 1, University of Erlangen-Nürnberg (FAU), Martensstrasse 5, 91058 Erlangen, Germany
[c] Institute of Materials Engineering, University of Kassel, Moenchebergstr. 3, 34125 Kassel, Germany

This chapter is reprinted from the article: D. D. Gebhart, A. Krapf, C. Gammer, B. Merle, and M. J. Cordill. Describing Mechanical Damage Evolution through in-situ Electrical Resistance Measurements. *J. Vac. Sci. Technol., A*, 1 March 2023; 41 (2): 023408. ISSN 0734-2101. https://doi.org/10.1116/6.0002362.

Contents

Abstract

The fatigue properties of metallizations used as electrical conductors in flexible electronic devices have been thoroughly studied over the years. Most studies use time intensive and costly characterization methods to evaluate mechanical damage. For their ease of access, in-situ electrical resistance measurements are often performed along with other characterization methods. However, the data are mostly used as an indicator of failure and a thorough analysis is usually missing. This work shows some deeper analysis methods of such data sets, using gold films on polyimide, with and without a chromium interlayer, revealing that grain growth, through-thickness cracking, and some general fatigue behavior can be determined from electrical resistance data alone. A case is made for increased utilization of such easily obtained data, reducing costs and time required for the experiments.

3.1 Introduction

With increasing demand for long-lasting flexible and form-adjusting thin film electronic devices and components, there is a need to better understand fatigue properties of metallizations used as electric conductors. Such electrical connections often consist of a rather ductile face-centered cubic (fcc) metal film (e.g. Cu, Ag, Au) on a polymer substrate. The work of adhesion in those systems can be low and an increase in adhesion between substrate and metal film was shown to improve fatigue properties [1]. An intrinsic increase in adhesion is hardly achievable. Instead, a thin adhesion promoting layer (in the low nm range) is often placed between substrate and conductive coating, where body-centered cubic (bcc) metals have shown to fulfill the requirements well. Metals used in interlayers include Ta [2, 3], Mo [4], and Cr [2, 5, 6]. Studies in fatigue properties of such systems mainly utilize time-intensive and expensive microscopy methods to characterize the degradation processes, with inspections mostly being performed intermittently or post loading. Conventional methods have revealed several factors that influence fatigue properties of thin film electronic conductors, such as film thickness or grain size [7, 8, 9]. While a thin 5 nm Ti interlayer was shown to improve longevity of a 1 μm Au films [10], in systems of thinner functional layers and thicker interlayers, the interlayer can be detrimental to damage resistance [11].

While many studies also perform in-situ electrical resistance measurements during cyclic loading, the recorded data is mostly used as an indicator of failure when the normalized resistance increases above a certain threshold. Since it is not easy to observe mechanical

damage in-situ, little research has so far been done to correlate specific changes in the electrical resistance data to mechanical damage evolution. Finding such correlations and the development of general methods to observe mechanical degradation in film conductors in electrical data will greatly improve the ease of studying such systems in the future. A novel method to analyze electrical data was recently introduced that uses the evolution of electrical resistance peak widths to differentiate between surface damage and through-thickness cracks (TTCs) [12].

The data sets studied in this work were obtained from material systems with and without an adhesion promoting interlayer while keeping the functional layer's thickness, grain size and texture constant. Gold was used as the functional layer for its chemical inertness. Without the formation of an oxide layer upon contact with air, cracks that close at strain minima during cyclical loading will better recover their conductivity, enhancing the information contained in electrical resistance data sets. This work demonstrates that certain correlations can be found and that those correlations can indicate how damage propagates, microstructure changes in the film, and what type of damage is present at different times during a loading regime.

3.2 Materials and Methods

The investigated material systems consist of 150 nm Au films deposited on polyimide substrates (Upilex-S obtained from Merck KGaA) with and without a 30 nm Cr interlayer. The films were produced by thermal evaporation using a custom-built deposition system described in [13] at a base pressure between 10^{-7} and 10^{-6} mbar with deposition rates of approximately 1 Å/s (Au) and between 0.5 and 0.8 Å/s (Cr). During depositions the substrate was heated to 80 °C (Au depositions) and 150 °C (Cr). The samples were cyclically loaded with an MTS Tytron 250, applying a sinusoidal load under strain control at a frequency of 0.5 Hz. Using a gauge length of 15 mm, the maximum strain amplitude was 2 % while the minimum value was set to 0.2 % as minima values of 0 % showed buckling of the samples due to compressive stress induced by the viscoelastic properties of the substrate. During loading, four-point resistance measurements were taken with a Keithley 2000 multimeter at a power line cycle setting of 1, resulting in approximately 20 data points per cycle. The data was analyzed in its normalized form as a ratio of electrical resistance, R, over initial resistance, R_0. The samples were imaged by scanning electron microscopy (SEM) in a Zeiss LEO 1525 and electron backscatter diffraction (EBSD) characterization was performed using a Tescan Magna with a Bruker eflash FS detector and Bruker's ESPRIT software, using a pixel size of 25 nm. To access the Cr interlayer for characterization, the Au layer was removed in several samples with aqua

regia, 5 ml HNO_3 (65 %) added to 20 ml of HCl (32 %), and SEM images were taken from the same regions before and after etching. Linear crack density measurements were performed by drawing 9 lines of 65 µm length, parallel to the straining direction, in SEM images of different sample regions and counting the number of intersections with damage sites.

3.3 Results and Discussion

First, a look at complete electrical resistance data sets acquired within this study reveals some general trends. Fig. 3.1 (a) and (b) show plots of one data set of all acquired data points for each system, with an inset of 10 cycles for the Au sample. Fig. 3.1 (c) and (d) show only the maxima and the minima data points for each cycle, taken from 5 measurement series and plotted as mean ± one sample standard deviation (s), revealing good reproducibility of measurements. The maxima data points contain information about damage initiation and propagation while the minima data points mirror crack closure properties and damage recovery at minima strain values. It can be seen that maxima values follow the general trend of an increasing slope at the beginning, a region of maximum slope, and an onset of saturation where the slope starts to decrease again. The change in slope is better visualized in Fig. 3.2 where only the first 2500 cycles are plotted for the Cr-Au system because the transitions happen at earlier cycle numbers. Some lines to guide the eye are included in Fig. 3.2 and the region with the highest slope is indicated where the curve can be approximated as linear.

The three sections in Fig. 3.2 can be interpreted as domains of different damage formation: (1) damage initiation and onset of propagation, (2) maximal and constant damage propagation, and (3) arresting damage propagation. In Domain 1, damage sites form at energetically favourable positions distributed throughout the sample and start to propagate, mainly perpendicular to the strain direction. In Domain 2, there is an equilibrium in damage initiation and crack propagation in combination with stress release and crack arrest through interaction of neighboring damage sites. Finite element models in literature show stress concentrations in the substrate at cracked sites in the functional film [14, 15] which leads to decreased stress in the surrounding regions and counteracts damage propagation. This effect takes over in Domain 3, where resistance increase starts to level off.

Identifying the three domains is a very time efficient way of analyzing such data sets. A quick look reveals where Domain 2 of damage propagation is present and a goal in developing long-lasting systems would be to shift Domain 2 to higher cycle numbers and

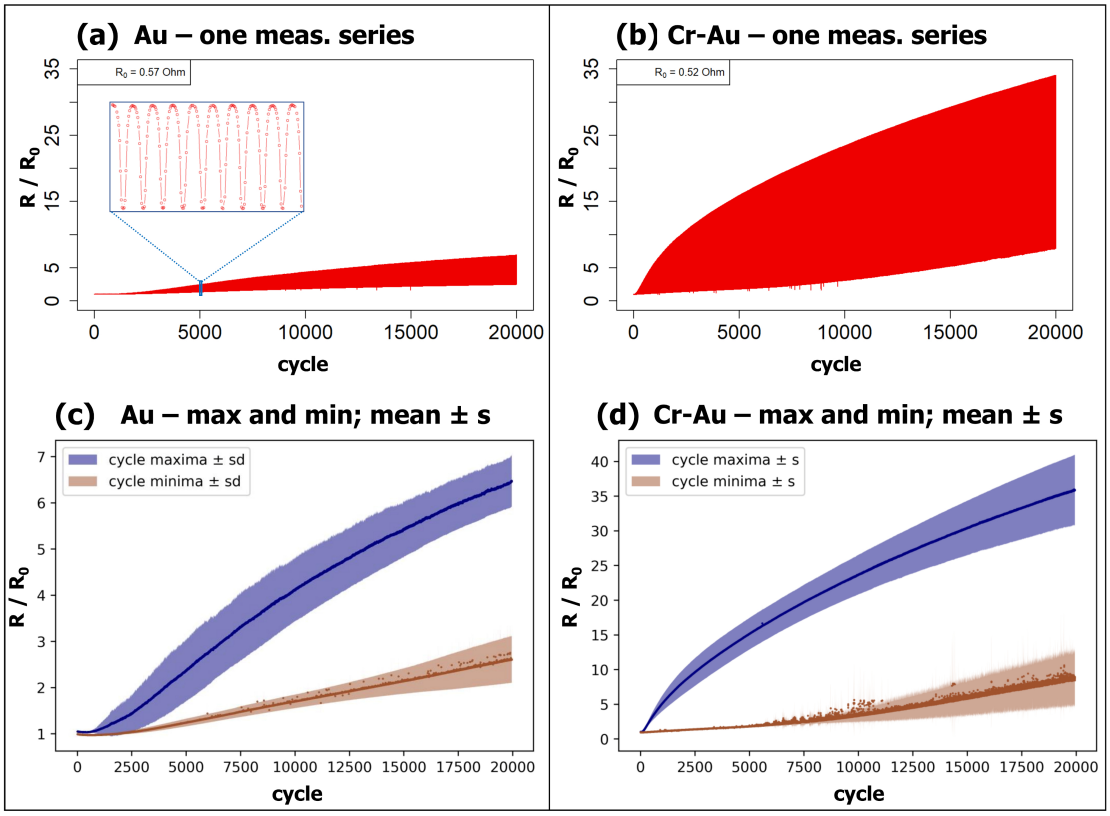

Figure 3.1: Resistance data (R/R_0) of cyclically strained (2 %) 150 nm Au (a, c) and 30 nm Cr / 150 nm Au bilayer (b, d) on PI. In (a-b) all data points for 1 measurement series up to 20000 cycles are shown. In (c-d), the averages of 5 measurement series are shown - cycle maxima (blue) and cycle minima (red). The error bars are ± 1 sample standard deviation. Note the different y-scale in (c) and (d).

decrease the slope as much as possible.

In the two studied systems in this work, Domain 2 sets in at lower cycle numbers (around cycles 150 to 600) in the Cr-Au system, with a slope of approximately 5 x 10^{-3} R_0/cycle compared to a slope of approximately 3 x 10^{-4} R_0/cycle in the region of around cycle 3500 to 9500 in the Au system. The relatively thick Cr interlayer of 30 nm, with a ratio of 1:5 to the 150 nm Au functional layer leads to faster degradation of the whole system. It is also revealed in SEM images in Fig. 3.3 that most of the damage occurs in Domain 2 for both film systems.

A second observation that is apparent from looking at the electrical resistance data

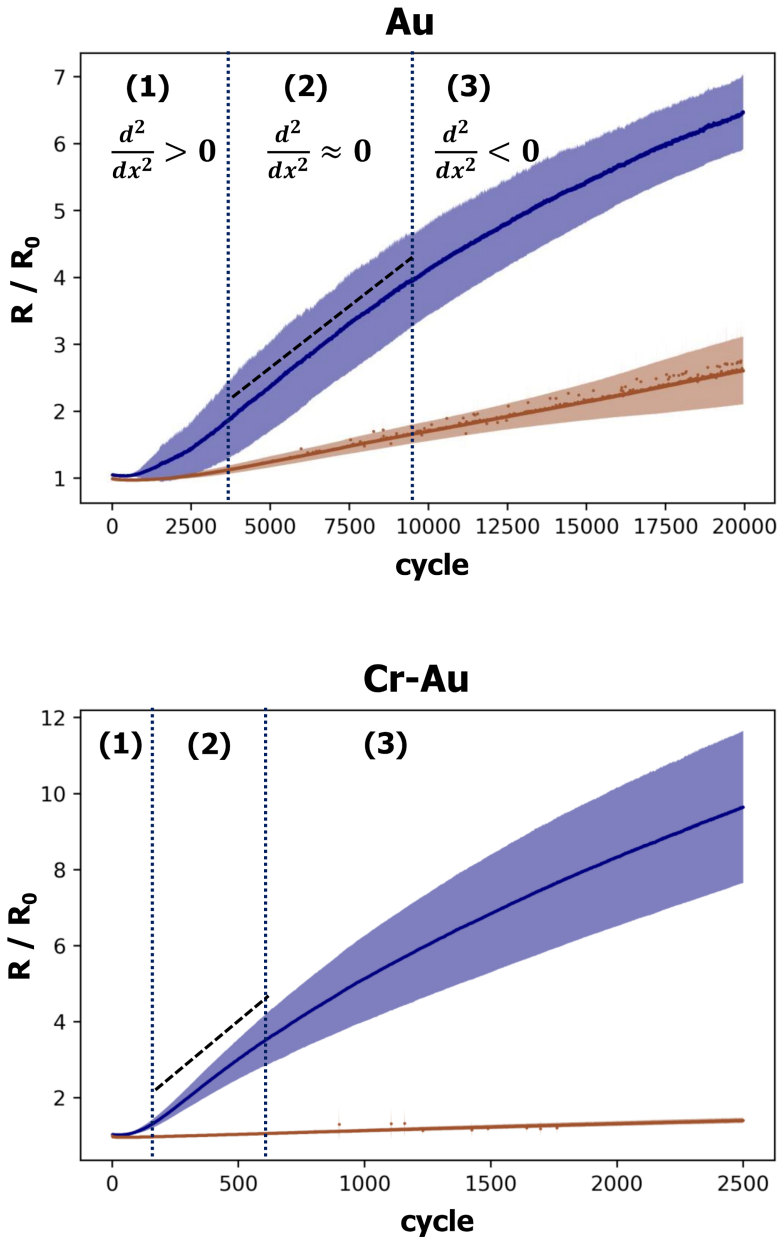

Figure 3.2: Maxima and minima resistance values taken during cyclic uniaxial straining to 2 % in Au (a: 20000 cycles) and Cr-Au (b: 2500 cycles) of 5 measurement series - mean ± 1 s. Three damage domains indicating the evolution of maxima values. Black dashed lines visualize linear increase in Domain 2. Note: different x- and y-scale.

is that the resistance amplitude is a lot higher in the Cr-Au system (see Fig. 3.1 (a) and (b)). SEM images (see Fig. 3.3) show that fewer but longer cracks are present in this system. If the simplified assumption is made that all cracks are fully opened at strain maxima, the conducting pathways running around those cracks could be seen as a network of parallel conductors with a certain resistance at narrow constrictions where cracks meet. A system showing fewer but longer cracks would consist of less parallel resistances and would show a higher overall resistance than a system with a greater number of parallel resistors of equal magnitude. It is possible that this amplitude is an indication of crack length and also the slope in Domain 2 could be an indication, however, more studies are needed to confirm this hypothesis. It is generally known that from one resistance data point, no estimation of crack length can be made, only a product of crack length and crack density can be determined [16]. However, it could be possible to separate information of those two parameters from an ensemble of data points through the evolution of cycle characteristics, such as peak shape and amplitude.

Previous studies have found abnormally large grain growth during cyclic loading of similar systems [10, 17] and grain size is known to be an important parameter in fatigue properties of thin metal films. To investigate grain growth, time intensive methods are necessary, such as EBSD or transmission electron microscopy. However, grain growth will also be reflected in simple electrical resistance measurements. In crystalline metals, electrons scatter at deviations from the periodic potential - this could be phonons, or defects, such as interstitials and vacancies, impurities, and also grain boundaries. Therefore, grain size will have an effect on the resistivity of a metal sample.

The samples studied here showed grain growth similar to that observed in literature[18, 10, 17, 19]. In in-lens SEM images (lower magnification images in Fig. 3.3), an increasing number of higher contrast areas can be observed close to cracks and also in areas between cracks. On closer inspection, the lighter areas are roughened surface features due to primary and secondary slip bands and resulting slip steps. An increased surface roughness leads to an increase in secondary electron emission and these surface features appear as bright areas in in-lens images. Fig. 3.4 (a) shows a close up of such features with indicated slip bands and Fig. 3.4 (b) and (c) show one SEM image with a complementary EBSD band contrast map, showing that those features are actually coarsened grains. The grain growth is also visible in electrical resistance minima values at early cycle numbers, before resistance increase due to damage propagation takes over. Fig. 3.5 shows a clear and continuous decrease in electrical resistance at early cycle numbers in the data sets of about 2 % in Au and around 4 % in Cr-Au. It has to be noted that the largest drop in the very first cycle could be due to a rearrangement of electrical contact with the clamps, but further decrease is most likely occurring due to grain coarsening. An increase in resistance at higher cycle numbers should not be interpreted as an end of

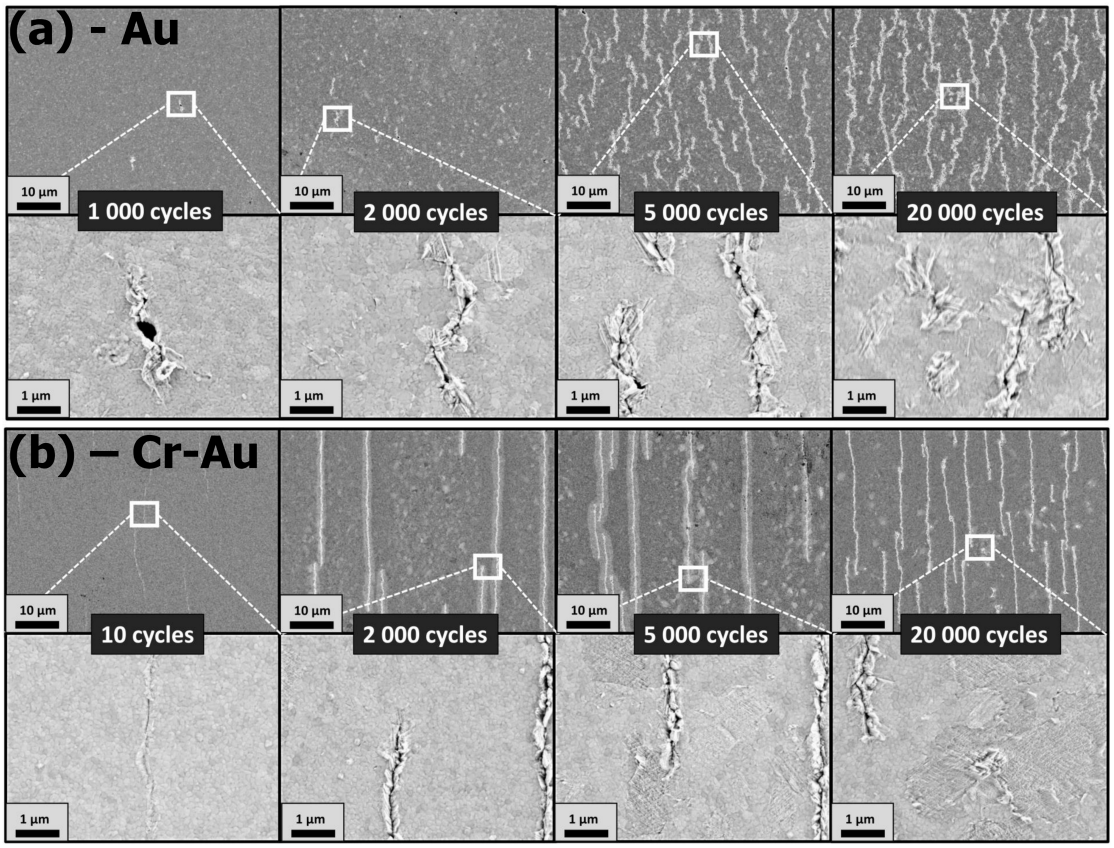

Figure 3.3: SEM images of damage evolution for Au (a) and Cr-Au (b). Lower magnifications taken with an in-lens secondary electron (SE) detector and higher magnifications with a SE detector at the side of the chamber. Note: all images are of similar sample regions, but not of the exact same areas.

grain coarsening, rather that the resistance increase from damage is the primary factor influencing resistance data from there on.

A previous study analyzing the evolution of electrical resistance peak characteristics has shown that full width at half maximum (FWHM) values can reflect the type of damage that is present to be either surface damage or through-thickness cracks (TTCs) [12]. Broad peaks with a plateau around the maximum indicate a complete crack opening before the strain maximum is reached. These broad peaks are a sign that TTCs are present. Narrower peaks, more closely mirroring the applied sinusoidal strain, are an indication of superficial damage and necking of conductive pathways between crack faces during loading. Fig. 3.6 shows the evolution of FWHM values for both investigated systems and for each system one early and one later stage resistance peak is depicted to better visualize this increase in peak width. Two factors influence FWHM values

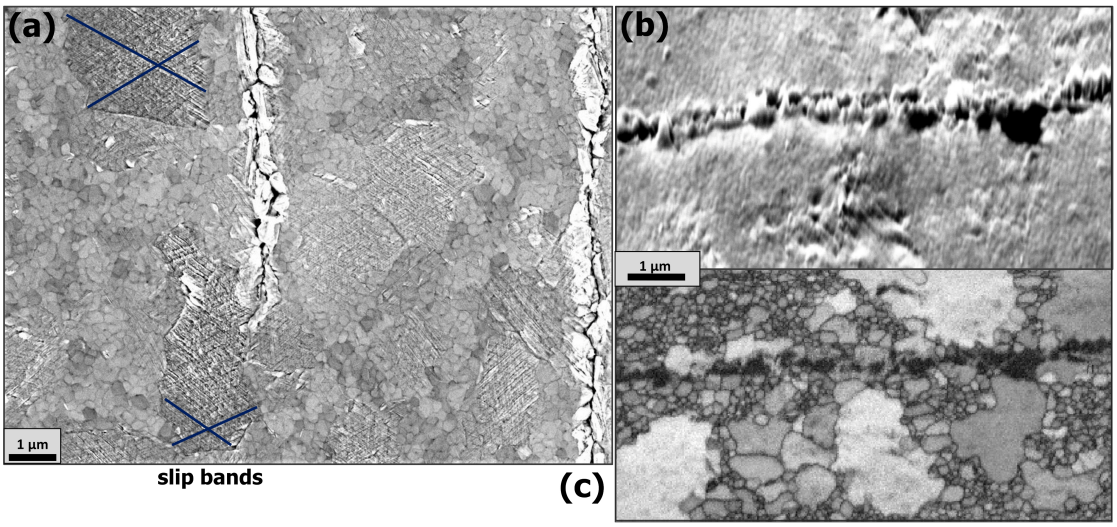

Figure 3.4: Slip steps increasing surface roughness and indicating large grains in Cr-Au samples after fatigue loading. (a) Top view SEM image showing slip bands marked by blue lines. (b) SEM overview (70° tilt) of slip steps close to a crack and (c) EBSD band contrast map of the same region depicted in (b), indicating large, singular grains where slip steps are present.

in counteracting ways. Pronounced damage formation and propagation leads to rather sharp peaks and a reduced FWHM value while a high percentage of TTCs present leads to broad peaks and an increase in FWHM values. Both samples show a FWHM value of around 0.5 at the start. This value is expected in undamaged condition because it is the value that mirrors the sinusoidal applied strain. The drop in FWHM values is present in both systems but it is more pronounced in the Cr-Au samples at early cycle numbers where significant damage is already introduced after 10 cycles, as can be seen in Fig. 3.3 (b). Both film systems show an increase in peak widths in the scope or the experiment with the increase slowing down at around 6000 cycles for Au, with a FWHM value of around 0.67 cycle durations, and at around 1500 cycles at a value of 0.7 cycle durations for Cr-Au. Here, it can be assumed that the damage present in the systems are mostly TTCs, as was shown in [12]. The values show good reproducibility for the five tested samples each, especially in the Cr-Au system. It has to be noted that this method will not work in ambient atmosphere for a material which forms a dielectric oxide layer immediately upon contact with air.

With all data pointing at earlier damage onset, propagation, and saturation in the Cr-Au system, a closer look was taken on the underlying Cr layer in this system. The Au layer was removed with aqua regia which introduces a passivating oxide layer on the Cr interlayer [20]. SEM images in Fig. 3.7 show the same sample regions before

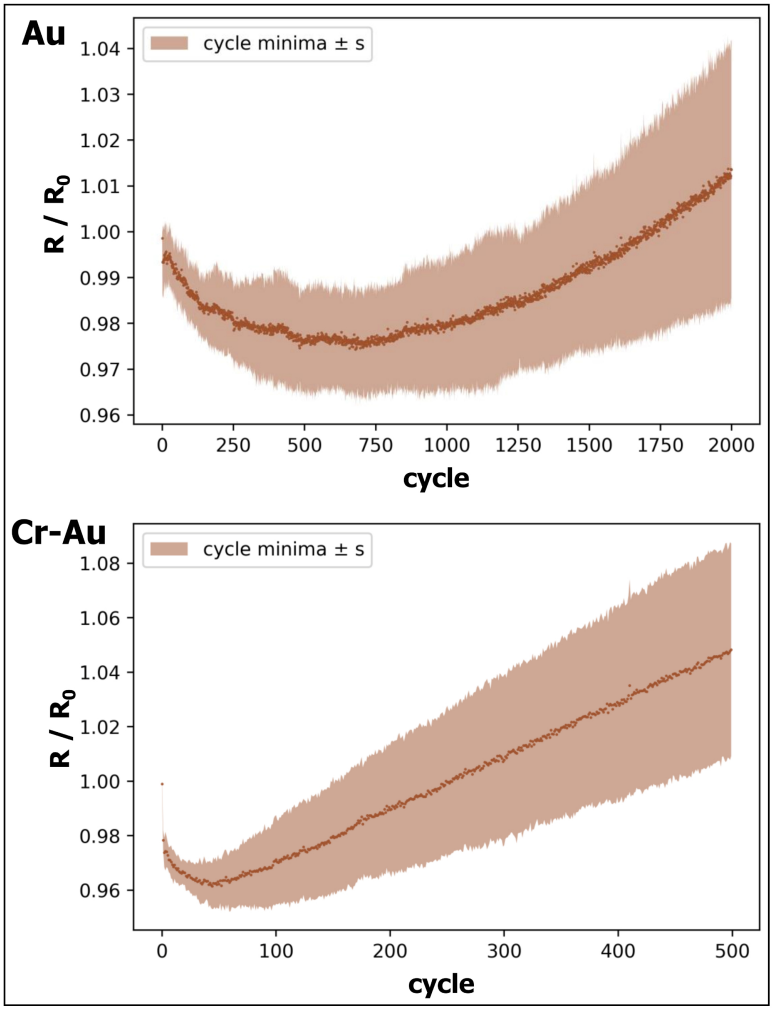

Figure 3.5: Initial decrease in minima resistance values for Au (top) and Cr-Au (bottom), indicating grain growth in the Au layer during early cycling. Mean ± 1 s.

and after removal of the Au layer after 10 and 1000 loading cycles, with damage sites overlapping in the Cr and Au layer. Linear crack density measurements in the Cr layer showed most of the damage already formed after 50 cycles, with an increase of about 40 % from cycle 50 (0.10 ± 0.02 cracks per micrometer) to cycle 1000 (0.14 ± 0.01 cracks/µm). After 10 cycles (Fig. 3.7 (a-b)) the cracks present in the Cr layer seem to fully permeate the layer's thickness, while the Au layer only shows superficial damage and no through-thickness cracks through both layers are observed. With further cycling to 1000 cycles (Fig. 3.7 (c-d)), the damage in the Au film propagates in the out-of-plane direction, forming through-thickness cracks. This correlates well with a strong increase

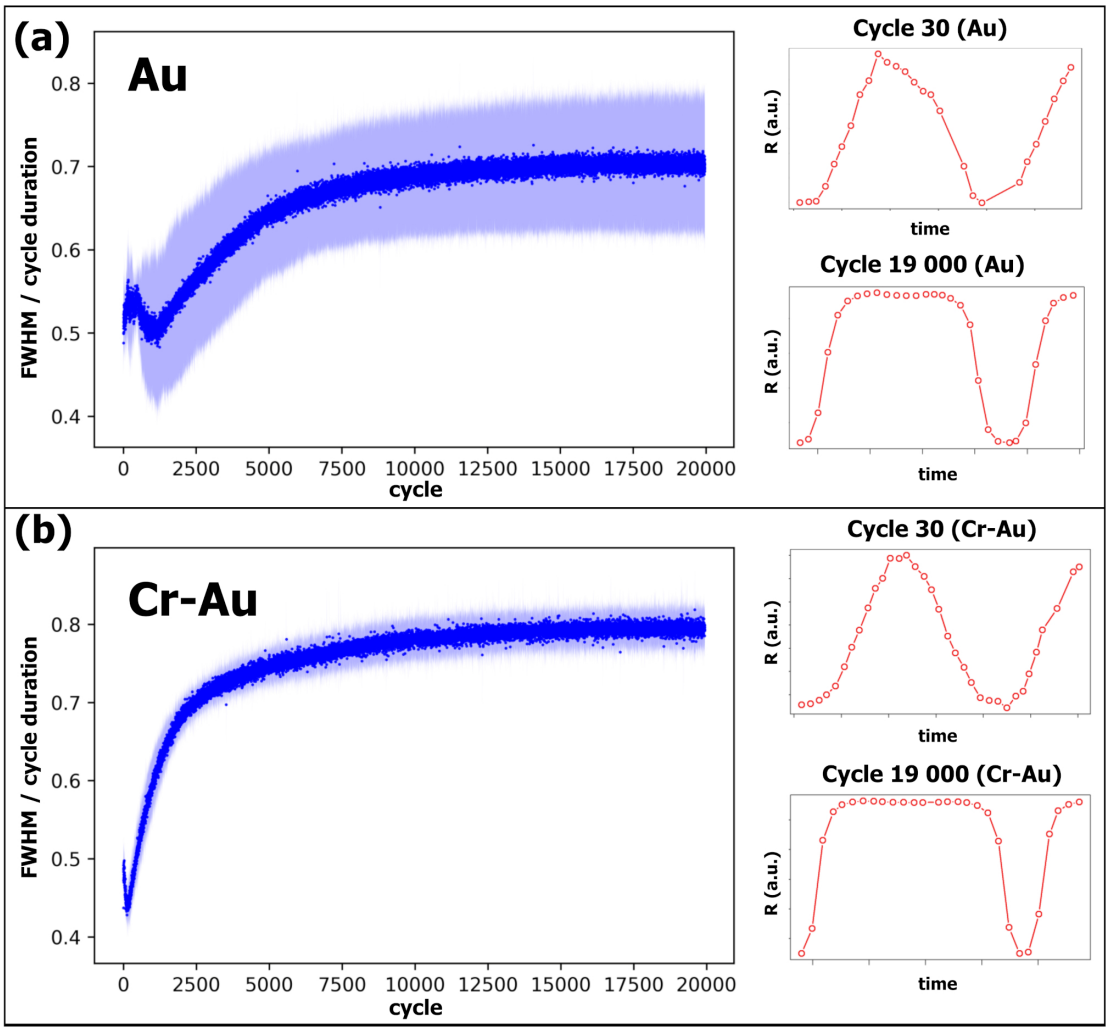

Figure 3.6: FWHM values showing a broadening of resistance peaks for both Au (a) and Cr-Au (b) - mean (dark blue) ± 1 s (light blue). Plots on the right show resistance curves for cycle 30 and cycle 19000 of one measurement series for each system to visualize the peak broadening.

in FWHM values in this system (see Fig. 3.6 (b)) and is a good example of the powerful application of one of the methods described in this work.

3.4 Conclusions

It is shown that electrical resistance data taken during cyclic uniaxial loading of thin film conductors contain useful information beyond a simple failure criterion. Electrical data

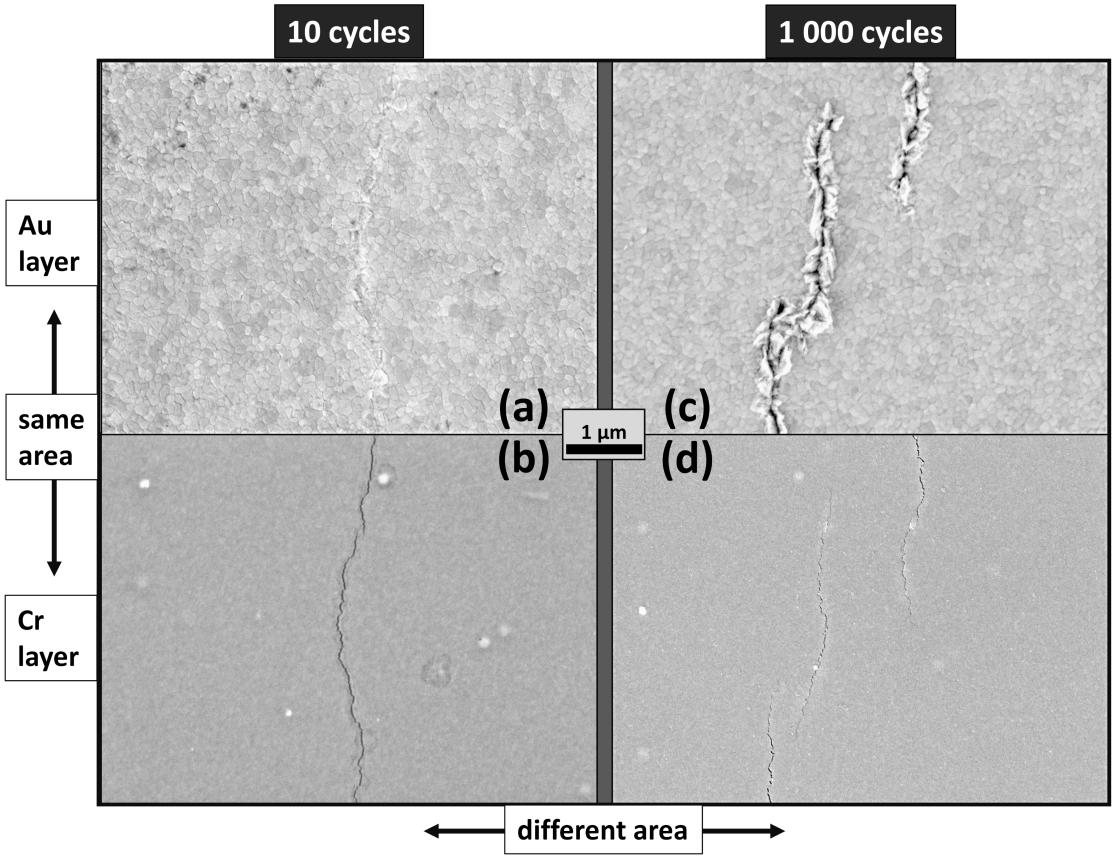

Figure 3.7: SEM images of Cr-Au after 10 (left; a, b) and 1000 (right; c, d) cycles to 2 % maximum strain. Top (a, c): Au layer. Bottom (b, d): Underlying Cr-Layer at the same regions, imaged after chemical removal of Au.

was correlated to 3 domains of damage propagation and to grain growth. A previously published method for identifying the formation of through-thickness cracks from surface damage through an increase in electrical resistance FWHM values could be verified with congruent SEM images of a Au top layer and a Cr interlayer. A case is made for a more extensive use of electrical data, for its ease of acquisition and the possibility of quick and cost-effective in-situ analysis, once methods of interpreting the data are established.

Acknowledgments

Funding: This work was supported by the Austrian Science Fund (FWF) [Project I 4384-N] and the German Research Foundation (DFG) [grant ME-4368/8] within the framework of the D-A-CH cooperation FATIFACE.

Data Availability

The data that support the findings of this study are available from the corresponding author upon reasonable request.

Author Declarations

The authors have no conflicts to disclose.

3.5 References

[1] G.-D. Sim, Y. Hwangbo, H.-H. Kim, S.-B. Lee, and J. J. Vlassak. Fatigue of polymer-supported Ag thin films. *Scripta Materialia*, 66(11):915–918, 2012. ISSN 1359-6462. URL http://doi.org/https://doi.org/10.1016/j.scriptamat.2012.02.030. Viewpoint set no. 49: Strengthening effect of nano-scale twins.

[2] J. D. Yeager, D. J. Phillips, D. M. Rector, and D. F. Bahr. Characterization of flexible ECoG electrode arrays for chronic recording in awake rats. *Journal of Neuroscience Methods*, 173(2):279–285, 2008. ISSN 0165-0270. URL http://doi.org/https://doi.org/10.1016/j.jneumeth.2008.06.024.

[3] D. Wang, P. A. Gruber, C. A. Volkert, and O. Kraft. Influences of Ta passivation layers on the fatigue behavior of thin Cu films. *Materials Science and Engineering: A*, 610:33–38, 2014. ISSN 0921-5093. URL http://doi.org/https://doi.org/10.1016/j.msea.2014.05.024.

[4] P. Kreiml, M. Rausch, V. L. Terziyska, J. Winkler, and M. J. Cordill. Compressive and tensile bending of sputter deposited Al/Mo bilayers. *Scr. Mater.*, 162:367–371, March 2019. ISSN 1359-6462. URL http://doi.org/10.1016/j.scriptamat.2018.11.048.

[5] N. Lu, X. Wang, Z. Suo, and J. Vlassak. Metal films on polymer substrates stretched beyond 50%. *Applied Physics Letters*, 91(22):221909, 2007. URL http://doi.org/10.1063/1.2817234.

[6] M. Todeschini, A. Bastos da Silva Fanta, F. Jensen, J. B. Wagner, and A. Han. Influence of Ti and Cr Adhesion Layers on Ultrathin Au Films. *ACS Appl. Mater. Interfaces*, 9(42):37374–37385, October 2017. ISSN 1944-8244. URL http://doi.org/10.1021/acsami.7b10136.

[7] M. J. Cordill, O. Glushko, A. Kleinbichler, B. Putz, D. M. Többens, and C. Kirchlechner. Microstructural influence on the cyclic electro-mechanical behaviour of ductile films on polymer substrates. *Thin Solid Films*, 644:166–172, December 2017. ISSN 0040-6090. URL http://doi.org/10.1016/j.tsf.2017.06.067.

[8] R. Schwaiger and O. Kraft. Size effects in the fatigue behavior of thin Ag films. *Acta Mater.*, 51(1):195–206, January 2003. ISSN 1359-6454. URL http://doi.org/10.1016/S1359-6454(02)00391-9.

[9] G. P. Zhang, R. Schwaiger, C. A. Volkert, and O. Kraft. Effect of film thickness and grain size on fatigue-induced dislocation structures in Cu thin films. *Philos. Mag. Lett.*, 83(8):477–483, August 2003. ISSN 0950-0839. URL http://doi.org/10.1080/0950083031000151383.

[10] H.-L. Chen, X.-M. Luo, D. Wang, P. Schaaf, and G.-P. Zhang. Achieving very high cycle fatigue performance of Au thin films for flexible electronic applications. *J. Mater. Sci. Technol.*, 89:107–113, October 2021. ISSN 1005-0302. URL http://doi.org/10.1016/j.jmst.2021.02.025.

[11] M. J. Cordill, T. Jörg, D. M. Többens, and C. Mitterer. Improved fracture resistance of Cu/Mo bilayers with thickness tailoring. *Scr. Mater.*, 202:113994, September 2021. ISSN 1359-6462. URL http://doi.org/10.1016/j.scriptamat.2021.113994.

[12] D. D. Gebhart, A. Krapf, C. Gammer, B. Merle, and M. J. Cordill. Linking through-thickness cracks in metallic thin films to in-situ electrical resistance peak broadening. *Scr. Mater.*, 212:114550, April 2022. ISSN 1359-6462. URL http://doi.org/10.1016/j.scriptamat.2022.114550.

[13] E. Preiß. *Fracture Toughness of Freestanding Metallic Thin Films Studied by Bulge Testing*. FAU University Press, 2018. ISBN 978-3-96147-118-8. URL http://doi.org/10.25593/978-3-96147-118-8.

[14] V. M. Marx, F. Toth, A. Wiesinger, J. Berger, C. Kirchlechner, M. J. Cordill, F. D. Fischer, F. G. Rammerstorfer, and G. Dehm. The influence of a brittle Cr interlayer on the deformation behavior of thin Cu films on flexible substrates: Experiment and model. *Acta Mater.*, 89:278–289, May 2015. ISSN 1359-6454. URL http://doi.org/10.1016/j.actamat.2015.01.047.

[15] I. Ben Cheikh, G. Parry, D. Dalmas, R. Estevez, and J. Marthelot. Analysis of the multi-cracking mechanism of brittle thin films on elastic-plastic substrates. *Int. J. Solids Struct.*, 180-181:176–188, December 2019. ISSN 0020-7683. URL http://doi.org/10.1016/j.ijsolstr.2019.07.026.

[16] O. Glushko, B. Putz, and M. J. Cordill. Determining effective crack lengths from electrical measurements in polymer-supported thin films. *Thin Solid Films*, 699:137906, April 2020. ISSN 0040-6090. URL http://doi.org/10.1016/j.tsf.2020.137906.

[17] O. Glushko and M. J. Cordill. The driving force governing room temperature grain coarsening in thin gold films. *Scr. Mater.*, 130:42–45, March 2017. ISSN 1359-6462. URL http://doi.org/10.1016/j.scriptamat.2016.11.012.

[18] O. Glushko and M. J. Cordill. Electrical Resistance Decrease Due to Grain Coarsening Under Cyclic Deformation. *JOM*, 66(4):598–601, April 2014. ISSN 1543-1851. URL http://doi.org/10.1007/s11837-014-0943-x.

[19] O. Glushko and D. Kiener. Initiation of fatigue damage in ultrafine grained metal films. *Acta Mater.*, 206:116599, March 2021. ISSN 1359-6454. URL http://doi.org/10.1016/j.actamat.2020.116599.

[20] P. Köllensperger, W. Karl, M. Ahmad, W. Pike, and M. Green. Patterning of platinum (Pt) thin films by chemical wet etching in Aqua Regia. *Journal of Micromechanics and Microengineering - J MICROMECHANIC MICROENGINEER*, 22, June 2012. URL http://doi.org/10.1088/0960-1317/22/6/067001.

4

Cyclic Failure of a Cr–Au Bilayer on Polyimide: In Situ Transmission Electron Microscopy Observations of Interfacial Dislocation Mechanisms

David D. Gebhart[a], Anna Krapf[b], Lukas Schretter[a], Alice Lassnig[a], Benoit Merle[c], Megan J. Cordill[a], Christoph Gammer[a],

[a] Erich Schmid Institute of Materials Science, Austrian Academy of Sciences, Jahnstrasse 12, 8700 Leoben, Austria
[b] Department of Materials Science & Engineering, Institute 1, University of Erlangen-Nürnberg (FAU), Martensstrasse 5, 91058 Erlangen, Germany
[c] Institute of Materials Engineering, University of Kassel, Moenchebergstr. 3, 34125 Kassel, Germany

This chapter is reprinted from the article: D. D. Gebhart, A. Krapf, L. Schretter, A. Lassnig, B. Merle, M. J. Cordill, and C. Gammer. Cyclic Failure of a Cr–Au Bilayer on Polyimide: In Situ Transmission Electron Microscopy Observations of Interfacial Dislocation Mechanisms *Advanced Engineering Materials*, 26(19):2400251 ISSN 1438-1656. URL https://doi.org/10.1002/adem.202400251.

Contents

Abstract

This work presents in-situ transmission electron microscopy observations of dislocation activities and associated fatigue properties in a cross-sectional sample of a Cr-Au bilayer on a polyimide substrate under cyclic loading. Dislocation structures in the Au layer are observed to evolve into a geometrically necessary boundary parallel to the Cr-Au interface, which significantly impedes dislocation motion and plays a crucial role in enhancing the fatigue resistance of the studied sample. While a comparison to the damage in a conventional blanket film testing geometry reveals some differences in the accumulation of plastic flow, the findings can provide insights into the underlying mechanisms governing fatigue in nanostructured multilayer materials on polymer substrates.

Keywords

In-Situ TEM, Fatigue Resistance, Metal Bilayer, Polyimide Substrate, Dislocation Activity, Geometrically Necessary Boundaries, Cyclic Loading

4.1 Introduction

Thin metal layers on polyimide substrates are used as flexible and shape-adjusting conductors in electronic devices and components, such as displays, sensors, or microelectromechanical systems (MEMS), among a variety of other applications. An additional interlayer may be used to increase adhesion between the main functional layer and the polymer substrate. Polyimides are a class of thermosetting polymers with excellent thermal stability, chemical inertness, and suitable flexibility which makes them an ideal choice for flexible electronics. Electrically conducting films or lines are typically coated from Cu, Au, Ag, or Al. They are rather ductile metals due to good dislocation mobility along close-packed planes in the face-centered cubic (fcc) crystal structure, which provides them with resistance to crack formation and failure in applications where they are exposed to mechanical or thermo-mechanical stresses.

Extensive research has been conducted on the fatigue of metal films on polymer substrates where cyclical load is applied through uniaxial loading,[1, 2] biaxial loading,[3] and bending.[4, 5] While valuable insights have been collected on the fatigue properties of specific material systems, underlying dislocation mechanisms can often only be

deduced from post-mortem transmission electron microscopy (TEM) inspections.[6, 7] Interlayers have been shown to be detrimental to the fatigue life of metal-polymer systems as they can act as crack initiation sites.[8, 9, 10, 11] However, while the effect is known, not much information is available on the root causes. In-situ TEM investigations can reveal the underlying mechanisms and are needed for a better understanding of processes influencing the fatigue lifetime of multilayer architectures. Fatigue damage is an accumulation of plastic deformation through the movement of dislocations within each applied load cycle. The mobility of dislocations in a polycrystalline material is impeded by grain boundaries and twin boundaries, and it can also be hindered dislocation structures within a grain.[12] In a multilayer system, the interfaces are a strong additional barrier to dislocation mobility.[13, 14, 15] To visualize dislocation motion and to better understand the underlying mechanisms and their influence on fatigue behavior, in-situ TEM investigations are crucial. TEM imaging comes with the inherent limitation that a sample needs to be electron transparent. While an amorphous polyimide substrate can fulfill transparency requirements in the TEM up to a thickness of 3 µm,[16] a crystalline multilayer system needs to be imaged as a cross-section to achieve a clear image.

This work presents an in-situ TEM fatigue investigation of a cross-sectional sample of a Cr-Au bilayer on a polyimide substrate. Focus is placed on the dislocation activity in the Au layer, and on the evolution of dislocation structures.

4.2 Results and Discussion

In the as-deposited and as-produced state, various dislocations were already present throughout the sample (see **Figure 4.1** (a)). During precycling, a migration of the grain boundary (GB) on the right-hand side of the center grain was observed, leading to a coarsening of this grain (see Figure 4.1 (a) and (b)). With further cycling at constant maximum loads of 560 µN, a type of dislocation wall structure formed, showing large dislocation activity in the structure's vicinity while acting as a barrier to dislocation mobility (Figure 4.1 (c) and supplementary video S1). Similar dislocation wall structures have been found in cyclically loaded Ni micropillars [17], in combination with long-range strain fields associated with the presence of geometrically necessary dislocations (GNDs). With further cycling, the dislocation structure evolved into one distinct line, parallel to the Cr-Au interface, that acted as a barrier to dislocation motion and activated slip systems, and as an apparent source for dislocation nucleation throughout the experiment (see supplementary video S2). A nanodiffraction pattern map was taken after 200 cycles and two insets in Figure 4.1 (e) depict diffraction patterns from above and

below the feature, indicating a [611] zone axis. Both depictions show an average of 5 x 5 patterns taken at the regions indicated by white arrows in the figure. No difference in the positioning of the reflections could be determined between the two depictions but there are variations in spot intensities which indicate that a low-angle boundary, showing out-of-plane tilt, was present between the two regions. This implies the presence of a twist boundary. The distinct feature with a low mismatch angle is indicative of a type of dislocation boundary, an accumulation of either statistically stored dislocations (SSDs) or GNDs [12]. With the Au layer fixed to the Cr layer on one side, and with the Au film surface on the other side — the interface between the Au layer and the loosely adhering protective layer of amorphous carbon, a strain gradient must be present in this layer. It has been stated that geometrically necessary boundaries (GNBs) may form due to a non-uniform strain in the interior of the grains [18]. A GNB, a type of subgrain structure, is formed by glide dislocations. Kuhlmann-Wilsdorf and Hansen state that there are generally two types of such structures - incidental dislocation boundaries (IDBs) are a result of random mutual trapping of glide dislocations, and GNBs form due to glide-induced lattice rotations between neighboring volume elements within a grain [19]. In essence, GNBs accommodate different active slip systems of different magnitudes of plastic slip within a single grain [12, 20, 18, 21]. Au and Cr show quite a large mismatch in Poisson's ratios, with 0.42 for Au and 0.21 for Cr [22], further promoting the strain gradient in the presented sample, and GNBs are dislocation structures accommodating localized lattice misorientations due to such gradients within grains. The GNB first clearly appeared after 130 load cycles in the center grain of the specimen where activated slip systems terminated at its junction (see Figure 4.1 (d)). A white dashed line indicates the GNB's position in Figure 4.1 (f), after 400 cycles. GNBs are mostly described for large monotonic strain gradients introduced to a specimen but hardly in cyclically loaded samples. However, the accumulation of plastic flow during cycling at comparatively lower strains, with the associated strain gradient present in the Au layer within each cycle, seems to lead to the formation of a GNB just as in bulk specimens that are monotonically loaded to higher strains [23]. While not much literature is available on cyclically loaded samples, the accumulation of GNDs and the formation of GNBs has previously been described by Huang et al. at regions where a strain gradient is present in cyclically loaded Ni-based superalloys with grain sizes in the µm range [24].

From cycle 800 onwards (Figure 4.1 (h) to (j)), the GNB was observed to migrate downwards, towards the Cr-Au interface (the migration path is indicated in Figure 4.1 (i)), along with increased dislocation activity. Simultaneously, the GB to the left of the center grain migrated inwards, towards a developing crack in the Cr layer (seen and discussed later). This crack in the Cr layer may have introduced enhanced stress concentration in that region leading to shear stresses along both boundaries, associated

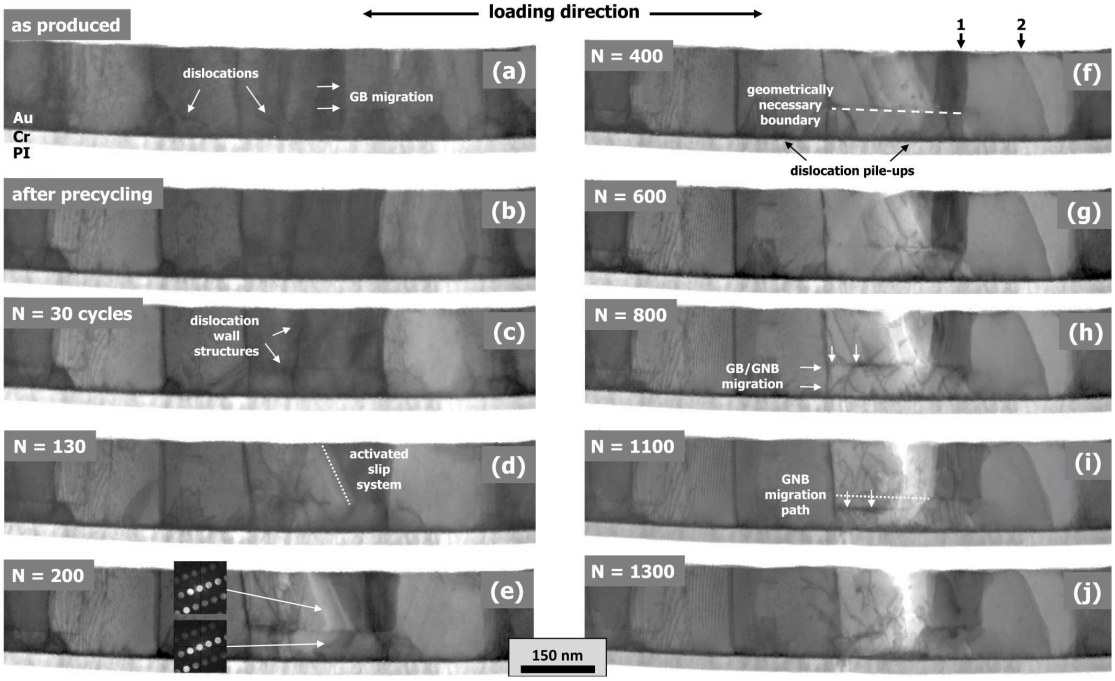

Figure 4.1: TEM micrographs showing both the Au and the Cr layer in the unloaded state before any applied loading (a), before cycling at constant load maxima of 560 µN (b), and throughout various stages during the experiment, with the sustained number of cycles indicated in the top left of each depiction (c to j). Insets in (e) show nanodiffraction patterns with arrows indicating the region where they were recorded. Two black arrows on top of (f) indicate two evolving features discussed in the text.

with GB migration [25, 26].

Throughout all stages of the sample's life, dislocations piled up at the interface between the Au and Cr layers. Those pile-ups were visible as areas of higher contrast in TEM observations throughout cycling, indicated in Figure 4.1 (f) and later in Figure 4.3 (a) and (j), and visible in supplementary videos 1 to 4. Activated slip systems were first revealed in the sample after 130 cycles (marked in Figure 4.1 (d)) through lines of alternating contrast in the scanning transmission electron microscopy (STEM) images which terminated at the GNB. With further cycling the brightening increased, suggesting a thinning of the sample around those slip bands. Along with this thinning, two developing features were observed (marked by black arrows above Figure 4.1 (f)): (1) what first appears similar to a broadening of the GB to the right of the thinning grain, and (2) a contrast change, where a part of the adjacent grain appears darker, up

to an arching boundary. However, closer inspection of the sample post-fracture revealed that those features stem from material transport along the direction of the transmitted electron beam (viewing direction), out of the free surfaces on the top and bottom of the cross-section. The diffraction patterns of the developing features showed only a reduction in overall intensity and no changes in the crystallographic orientation could be observed. **Figure 4.2** (a) gives a STEM micrograph of the sample after fracture and Figure 4.2 (b) presents a scanning electron microscopy (SEM) micrograph of the sample observed at a 36 ° angle (54 ° tilted from the top view perspective). Note that from this angle the top of the Au layer is visible in Figure 4.2 (b) (marked as Au (top)) through the protective carbon layer. In the SEM image, the front cross-sectional surface characteristics are well visible and it can be seen that the sample has become thicker due to the formation of extrusions which led to a darker contrast (feature 1). Feature 2 may be due to similar plastic flow out of the back surface of the sample, indicated by a white dashed line in Figure 4.2 (b). In previous cyclically loading experiments of similar blanket film samples conventionally tested, extrusions and slip steps were observed on the free surface in the direction out of the film's plane, perpendicular to the one observed here [8, 9] (shown in the discussion with Figure 4.4 (c) and (d)). This shows an inevitable shortcoming of cross-sectional in-situ TEM experiments, where plastic flow and dislocation mobility are less constrained at the newly introduced free surfaces than they would be in a conventionally tested blanket thin film. While more information is gathered from such TEM experiments, the limitations need to also be considered, and what may appear to be a grain boundary can be an out-of-plane deformation.

To reveal the dislocation activities within single cycles, screen grabs of videos recorded during cycling are displayed in Figure 4.3. With STEM scan speed limiting the image acquisition rate, 12 frames could be acquired over one strain cycle of 2 seconds. The timestamps in the images represent the time within the depicted cycle in steps of 1/6 s, with maximum strain being applied at a time of 1 s. Figure 4.3 (a) through (h) show that both full and partial dislocation glide through the sample contribute to plastic deformation. The screen grabs are of a video recorded during cycles 401-500, where thinning of the sample along a particular slip system was prevalent (see Figure 4.1 (f) and (g)). Both a full dislocation (Figure 4.3 (b)) and a leading partial dislocation (Figure 4.3 (d)) were seen gliding along a close-packed plane. The partial dislocation movement resulted in a stacking fault (SF) that appeared as a dark area in the bright field STEM image (indicated in Figure 4.3 (d) and (e)). SFs often appeared around strain maxima in the recorded videos and disappeared again when strain was reduced within a cycle (see Figure 4.3 (h) and see also supplementary video S3). Either the leading partial moved back through the grain or the trailing partial followed, generating plastic flow along that plane. Forward and backward glide of dislocations was observed throughout the experiment.

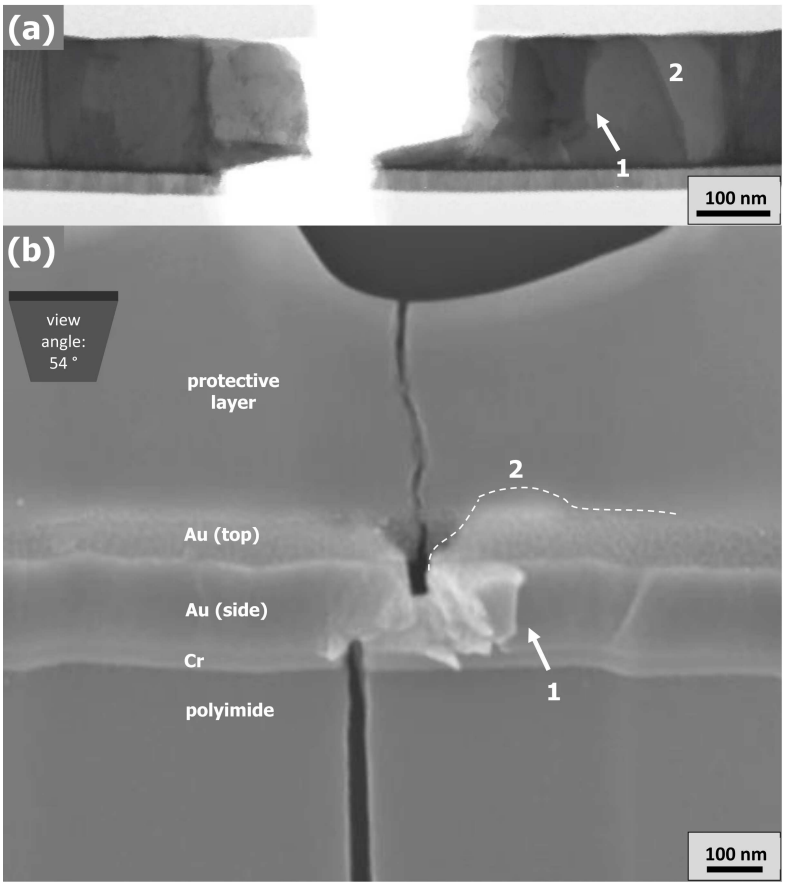

Figure 4.2: Post-fracture analysis of the sample. (a) A TEM micrograph while the specimen is still in contact with the indenter (leading to increased spacing between fracture surfaces) with a view angle straight onto the cross-section (90 °), and (b) SEM image with sample tilt and view angle (36 °) indicated in an inset in the top left corner. The deformations in the out-of-plane direction that led to a contrast change in TEM imaging are marked in both depictions. Note: The top side of the Au layer is visible through the protective carbon layer in (b).

Figure 4.3 (i) through (p) depict a later cycle (cycle 1097) where full dislocations could be seen propagating in one direction with increasing strain and propagating in the opposite direction when strain is decreased again. This bidirectional movement of dislocations is to be expected and is known to occur in both full [27] and partial [28] dislocations in fcc metals under cyclic loading conditions, and has been observed in molecular dynamics simulations [29].

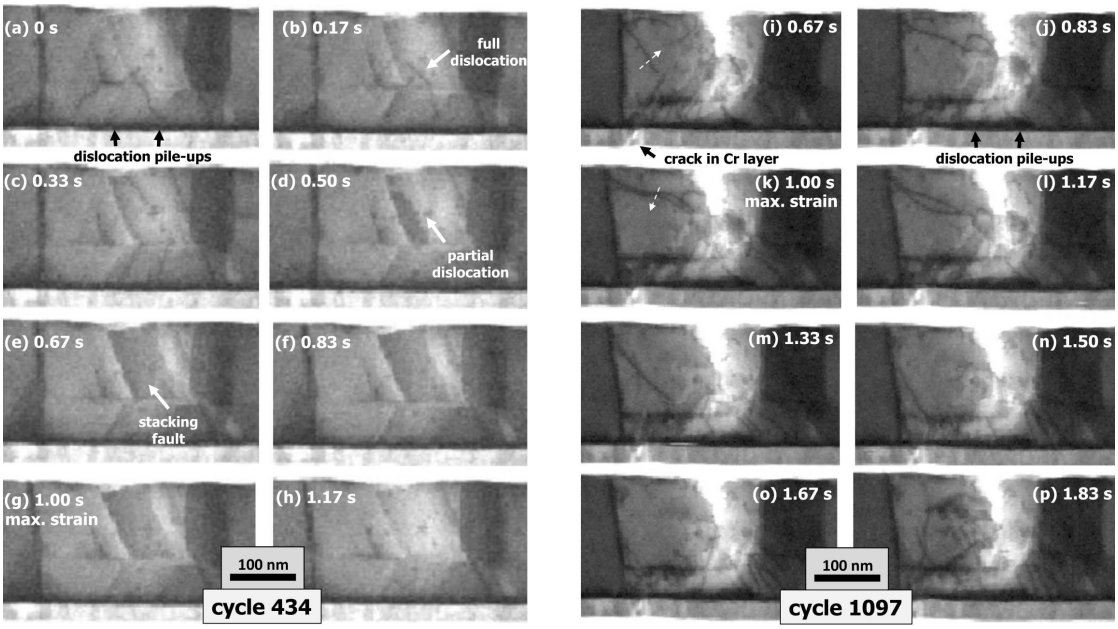

Figure 4.3: Eight frames taken from bright-field STEM video recordings of both cycle 434 (a to h) and cycle 1097 (i to p), showing dislocation activities in the center grain where most plastic flow accumulated during cyclic loading and where the sample ultimately failed. Full and partial dislocation motion and a resulting stacking fault are indicated in (a to h). A reversal in the direction of the motion of a full dislocation with strain reversal is indicated by white dashed arrows in (i) and (k). Black arrows in (a) and (j) indicate dislocation pile-ups at the interface between Cr and Au, leading to increased diffraction, visible as darker regions in the Au layer. A crack in the Cr layer is indicated in (i). Note that the two cycles are not shown over their full durations. Time stamps on the top left of each depiction indicate the stage of each cycle: unloaded at 0 s, maximum load at 1 s.

Many pinning points of dislocations could be seen throughout the grain and both depicted cycles show the GNB to be an obstacle to dislocation motion. Dislocations were emitted from activated sources at the GNB, at GBs, and at pinning points. While the dislocation termini mostly moved along boundaries, free surfaces, and the Au film surface during cycling, they sometimes repositioned so that the dislocation line terminated at a pinning point (see supplementary videos S2, S3, and S4).

A post-fracture analysis of the cross-sectional sample and the cracks in a sample of a blanket thin film of similar architecture, which is continuous in the xy-plane, reveals some differences in accumulated damage. Figure 4.4 compares the sample described in

this work (Figure 4.4 (a) and (b)) to a conventional blanket Cr-Au bilayer (30 nm - 150 nm) on polyimide that was uniaxially strained to 2 % for 1,600 cycles (Figure 4.4 (c) and (d)), and to one strained to 50 cycles (Figure 4.4 (e)). The accumulated plastic flow in the cross-sectional sample led to extrusions along the two newly present surfaces of the cross-section (see features 1 and 2 in Figure 4.2). However, since plastic flow was more constrained in the plane of the film , the xy-plane, in the blanket film sample, extrusions in the vicinity of cracks formed in the out-of-plane direction. A focused ion beam (FIB) cut through a formed crack in the blanket film sample (Figure 4.4 (d)) reveals what may be the most important difference in fracture behavior of the blanket film sample to the cross-sectional sample: while Au, Cr, and polyimide seem to still adhere to each other post-fracture in the cross-sectional sample, a void formed between the Au and Cr layers in the blanket film sample. Sim et al. previously discussed how crack formation in cyclically loaded ductile metal films, under tensile load, requires debonding from the substrate in different failure modes [30]. However, it seems more likely that necking and void formation led to what appears to be debonding in the blanket film. The absence of voids in the cross-sectional sample may be due to the possibility for vacancies to migrate to the free surfaces of the cross-section and that they are not confined to coalesce into voids at the interfaces. Additionally, the stress fields at the interfaces in the cross-sectional sample can be expected to be different due to stress relaxations through unimpeded deformations at the free surfaces. Figure 4.4 (e) depicts the cracked Cr interlayer of the blanket film specimen after a reduced number of just 50 load cycles to 2 %. The interlayer was revealed through selective wet etching of the Au layer post-loading. While only superficial damage was present in the Au layer at this stage, many microcracks were visible in the Cr layer. The Cr layer cracked before the Au layer and introduced damage in the Au layer through stress concentration at the cracked sites in the Cr layer. This is in contrast to the behaviour of the cross-sectional sample where plastic flow first started to accumulate in the Au layer before a crack formed in the Cr layer. Additionally, cracks were observed to form a lot earlier in the blanket film sample compared to the cross-sectional one (see also [8, 9]). A possible explanation is that cracks in the Cr layer initiate and propagate at randomly distributed favorable sites (e.g. nanosized grooves at the interface, hillocks) and the small interface area of the cross-sectional sample did not have any such sites present. The cross-sectional sample may also show different stress states at the interfaces due to its reduced size and unimpeded deformations in one dimension. In any case, it appears that the reduced size and the two additional free surfaces required for cross-section imaging can play a significant role in changing a specimen's resulting mechanical damage. While a lot of insight on the fundamental damage mechanisms can be deduced from in-situ TEM fatigue experiments of cross-sectional samples, the deviations in overall damage formation to blanket films must be considered.

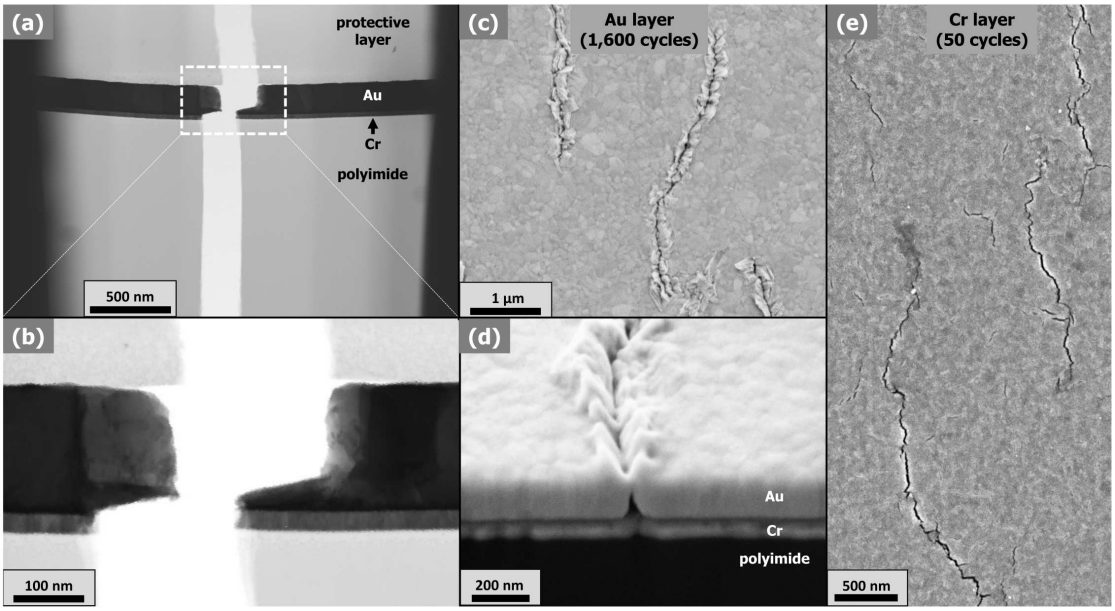

Figure 4.4: A comparison of the cross-sectional sample after fracture (a and b) to SEM micrographs of a blanket film strained to 2 % for 1,600 cycles (c and d) and 50 cycles (e). (d) shows the FIB cut cross-section of a crack. (e) presents the cracked Cr interlayer of a sample strained to 2 % for 50 cycles. The Au layer in (e) was removed by wet etching after the 50 load cycles.
Note: the Au layer thickness in the samples depicted in (c, d, and e) was slightly lower at 150 nm.

4.3 Conclusion

In-situ observations of a cross-sectional sample of a Cr-Au bilayer on a polyimide substrate during cyclic loading give insights into the dislocation activity and the sample's associated fatigue behavior. After various cycles of increasing load maxima during precycling, the specimen sustained a further 1327 cycles at constant maximum loads of 560 µN before it ultimately failed by intragranular rupture (see supplementary video S4 showing the last 27 cycles to failure). While a comparison to a conventionally tested blanket film of similar architecture shows some differences in the accumulation of plastic flow, the present experiment could reveal new insight into the dominant deformation mechanisms in this system. The main finding of this work is that dislocation wall structures inside an ultrafine-grained Au film evolved into what appeared to be a geometrically necessary boundary (GNB). The GNB formed parallel to the interface between Cr and Au, along the direction perpendicular to the largest strain gradient present in the Au layer. The GNB acted as an obstacle to dislocation motion and activated slip systems terminated at

its junction. This indicates that such geometrically necessary structures may play a large part in the damage accumulation of bilayer samples where a strain gradient is present and that their presence may increase fatigue life. To the best of the authors' knowledge, the influence of GNBs on the fatigue damage of nanostructured multilayer samples has so far not been discussed in the literature. Additional observations include the pile-up of dislocations at the interface between Au and Cr layers, dislocation structures acting as an obstacle to dislocation motion in the Au layer, back-and-forth motion of both full and partial dislocations in the Au layer, the formation of stacking faults, and the migration of both a GB and a GNB in the Au layer upon fracture of the Cr layer.

A comparison to cracks formed in a blanket film of similar architecture revealed some differences in the failure of the sample due to the newly formed free surfaces of the cross-section and due to the specimen's reduced size. However, new interpretations can be deduced for blanket films from the observed mechanisms of accumulation of plastic flow and the dislocation structures and their influence on dislocation motion. In-situ observations of dislocation activities, formed dislocation structures, and dislocation motion is crucial in understanding the accumulation of plastic flow in metal films. They give an understanding of mechanisms at the atomic scale and are a valuable complement to fatigue experiments on conventionally tested blanket film samples. The observed formation of a GNB may lead to future tailoring of multilayer systems to introduce such dislocation structures to increase the fatigue lifetime of thin films.

4.4 Experimental Section

Prior to TEM sample preparation, a Cr(30 nm)-Au(180 nm) bilayer was deposited onto a polyimide substrate of 50 µm thickness (Upilex-S; Merck KGaA, Darmstadt, Germany) using a custom thermal evaporation chamber at a base pressure of 10^{-7} to 10^{-6} mbar at a deposition rate of 0.5 to 0.8 Å s^{-1} (Cr) and approximately 1 Å s^{-1} (Au). The substrate was heated through quartz halogen lamps above the sample holder to 150 °C during the Cr deposition and reduced to 80 °C throughout the Au deposition. A post-deposition heat treatment was performed at 150 °C for 2 hours inside the chamber without breaking the vacuum.

A TEM lamella was cut out from the sample with Ga^+ ions, operating at 30 kV acceleration voltage and at ion current intensities between 10 nA (rough cutting) and 50 pA (polishing), using a FIB inside a Zeiss Auriga Workstation (Carl Zeiss AG, Oberkochen,

Germany). The workstation was equipped with an Omniprobe 200 nanomanipulator (Oxford Instruments plc, Abingdon, UK) and a gas injection system was used to attach the manipulator to the lamella by focused ion beam induced deposition (FIBID) of a Pt compound. Before placing the sample into the FIB chamber, a permanent marker was used to draw a line on the upper Au layer of the sample as an additional protection layer. After evaporation of the solvents inside the vacuum chamber, a residual amorphous layer of organic coloring compounds from the permanent marker of approximately 0.5 µm thickness remained as a protective layer against ion radiation damage.

The lamella with a top area of approximately 8 µm × 1 µm was cut and rotated 90° so that the cross-section was pointing in the out-of-plane direction. It was attached flat with FIBID Pt deposition onto two Si ridges on a push-to-pull (PTP) device (stiffness value: 450 N m^{-1}) obtained from Bruker Corp. (Billerica, USA) that was fixed on an accompanying Cu TEM sample holder with vacuum adhesive wax. From a side-view 1 ° angle, stepwise, trapezoid-shaped cuts of decreasing width were milled on the lamella from both top and bottom with the Ga^+ ion beam until an electron transparent mid-section remained of approximately 100 nm thickness over a width of 1 µm, spanning the cut-out cross-section. Another trapezoid-shaped cut was performed from a top view on a Pt protective layer deposited onto the PI substrate layer, without directly exposing the metal layers to the ion beam, to localize strain concentration during cyclic loading in the center of the lamella.

In-situ cyclic straining of the sample was performed inside a JEM-2200FS TEM (JEOL Ltd., Akishima, Japan), using a Hysitron PI 95 TEM PicoIndenter (Bruker Corp., Billerica, USA). To find a suitable maximum load, the load was slowly increased from 35 µN to 560 µN, in steps of 5 to 10 µN, until a pronounced dislocation activity could be observed within one cycle. Precycling primarily consisted of single, slow cycles with a full cycle duration of 60 s, with some sets of faster cycles (0.5 Hz) performed at irregular intervals. In total, approximately 300 cycles were performed at various load maxima during precycling. The strain at the thinnest region of the sample was measured to be approximately 3 % at a load of 560 µN at the beginning of cyclic loading, increasing to up to 5 % at later stages when the center region cross-section decreased and the applied force was more concentrated. With the cyclic peak load kept at 560 µN, the sample was cycled at 0.5 Hz, predominantly in sets of 100 cycles. During cycling, scanning live view videos were captured in bright field scanning TEM (BF-STEM) mode, and in between sets, BF-STEM micrographs were recorded at a lower acquisition rate, all performed at an acceleration voltage of 200 kV. Additionally, scanning nanodiffraction mapping [31] was used to record a map of 256×64 equally spaced diffraction patterns. A stepsize of 2 nm was chosen allowing to scan the entire region of interest. The diffraction patterns were recorded using a

MerlinEM direct electron detector and scanning was carried out using a TVIPS universal scan generator. Three pattern maps were recorded before and during precycling, one was recorded after 200 cycles at 560 µN, and one was recorded after the sample failed at 1,327 cycles at 560 µN. The patterns were analyzed using the software tool CrysTBox [32].

Figure 4.5 presents the sample mounted on the PTP device in different stages of preparation and from various viewing angles and magnifications. An SEM image is given in Figure 4.5 (a), FIB micrographs in Fig 4.5 (b) and (c), and TEM micrographs in (d) and (e). The PTP device transforms the compressive motion of the indenter (indicated with a black arrow) into a tensile force on the sample by loading the four springs. Unpublished SEM micrographs of blanket film samples, which were recorded in the scope of a previous publication [9], are shown at the end of this work as a comparison to the cross-sectional sample. They were taken with an LEO 1525 SEM (Carl Zeiss AG, Oberkochen, Germany). For experimental details about the conventionally tested film samples, the reader is referred to that publication [9].

Acknowledgements

Funding: This work was supported by the Austrian Science Fund (FWF) [Project I 4384-N] and the German Research Foundation (DFG) [grant ME-4368/8] within the framework of the D-A-CH cooperation FATIFACE.

Data Availability

The data that support the findings of this study are available from the corresponding author upon reasonable request.

Author Declarations

The authors have no conflicts to disclose

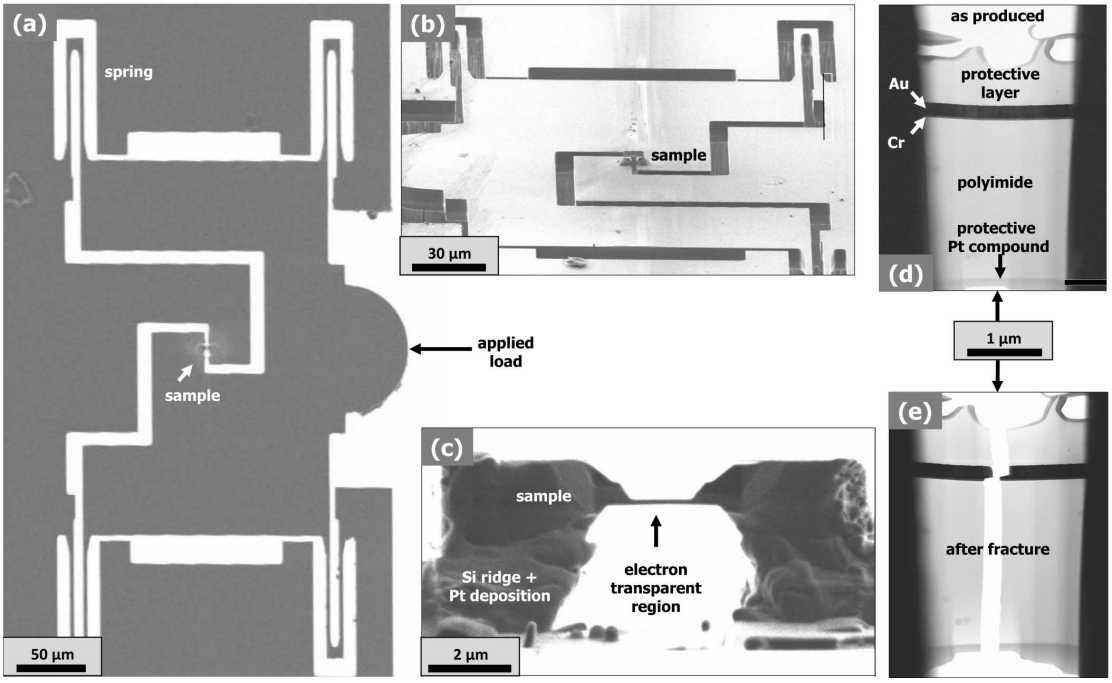

Figure 4.5: Overview of the measurement set-up from various angles: (a) Top-view SEM micrograph of the push-to-pull device with the sample mounted in the center, with four springs at the edges of the imaged region. Load is applied from the right-hand side by the indenter, in the plane of the image. (b) FIB acquisition from a 36 ° view angle, and (c) an enlarged view at a 1 ° angle showing the thinned, electron transparent center region. (d and e) TEM micrographs of the sample before loading and post-fracture.

4.5 References

[1] D. Wang, P. A. Gruber, C. A. Volkert, and O. Kraft. Influences of Ta passivation layers on the fatigue behavior of thin Cu films. *Mater. Sci. Eng., A*, 610:33–38, July 2014. ISSN 0921-5093. URL http://doi.org/10.1016/j.msea.2014.05.024.

[2] O. Glushko and D. Kiener. Initiation of fatigue damage in ultrafine grained metal films. *Acta Mater.*, 206:116599, March 2021. ISSN 1359-6454. URL http://doi.org/10.1016/j.actamat.2020.116599.

[3] S. Altaf Husain, P. Kreiml, P.-O. Renault, C. Mitterer, M. J. Cordill, and D. Faurie. Link between cracking mechanisms of trilayer films on flexible substrates and electro-mechanical reliability under biaxial loading. *J. Vac. Sci. Technol., A*, 41(3), May 2023. ISSN 0734-2101. URL http://doi.org/10.1116/6.0002348.

[4] T.-W. Kim, J.-S. Lee, Y.-C. Kim, Y.-C. Joo, and B.-J. Kim. Bending Strain and Bending Fatigue Lifetime of Flexible Metal Electrodes on Polymer Substrates. *Materials*, 12(15):2490, August 2019. ISSN 1996-1944. URL http://doi.org/10.3390/ma12152490.

[5] D.-J. Lee, J.-S. Lee, T.-W. Kim, S.-Y. Lee, Y.-B. Park, Y.-C. Joo, and B.-J. Kim. Effect of the Thermal Annealing on the Stretchability and Fatigue Failure of the Copper Film on the Polymer Substrate. *J. Electron. Mater.*, 48(7):4582–4588, July 2019. ISSN 1543-186X. URL http://doi.org/10.1007/s11664-019-07237-z.

[6] X. M. Luo and G. P. Zhang. Grain boundary instability dependent fatigue damage behavior in nanoscale gold films on flexible substrates. *Mater. Sci. Eng., A*, 702:81–86, August 2017. ISSN 0921-5093. URL http://doi.org/10.1016/j.msea.2017.07.006.

[7] G. P. Zhang, C. A. Volkert, R. Schwaiger, P. Wellner, E. Arzt, and O. Kraft. Length-scale-controlled fatigue mechanisms in thin copper films. *Acta Mater.*, 54(11):3127–3139, June 2006. ISSN 1359-6454. URL http://doi.org/10.1016/j.actamat.2006.03.013.

[8] D. D. Gebhart, A. Krapf, C. Gammer, B. Merle, and M. J. Cordill. Linking through-thickness cracks in metallic thin films to in-situ electrical resistance peak broadening. *Scr. Mater.*, 212:114550, April 2022. ISSN 1359-6462. URL http://doi.org/10.1016/j.scriptamat.2022.114550.

[9] D. Gebhart, A. Krapf, B. Merle, C. Gammer, and M. Cordill. Describing mechanical damage evolution through in situ electrical resistance measurements. *J. Vac. Sci. Technol., A*, 41:023408, February 2023. URL http://doi.org/10.1116/6.0002362.

[10] M. J. Cordill, T. Jörg, D. M. Többens, and C. Mitterer. Improved fracture resistance of Cu/Mo bilayers with thickness tailoring. *Scr. Mater.*, 202:113994, September 2021. ISSN 1359-6462. URL http://doi.org/10.1016/j.scriptamat.2021.113994.

[11] Y. Xia, Z. Xie, J. Zuo, K. Wu, X. Yao, G. Liu, and J. Sun. Fatigue tolerance of nanostructured Cu/interlayer bilayers: Tuned by heterogeneous interface. *Scr. Mater.*, 234:115563, September 2023. ISSN 1359-6462. URL http://doi.org/10.1016/j.scriptamat.2023.115563.

[12] H. Pan, Y. He, and X. Zhang. Interactions between Dislocations and Boundaries during Deformation. *Materials*, 14(4):1012, February 2021. ISSN 1996-1944. URL http://doi.org/10.3390/ma14041012.

[13] A. Kashiwar. *TEM Investigations of Deformation Mechanisms in Nanocrystalline Metals and Multilayered Composites*. Ph.d. thesis, Technische Universität Darmstadt, Darmstadt, 2022. URL http://doi.org/10.26083/tuprints-00020058.

[14] S. Shao and S. N. Medyanik. Dislocation–interface interaction in nanoscale fcc metallic bilayers. *Mech. Res. Commun.*, 37(3):315–319, April 2010. ISSN 0093-6413. URL http://doi.org/10.1016/j.mechrescom.2010.03.007.

[15] A. Sáenz-Trevizo and A. M. Hodge. Nanomaterials by design: a review of nanoscale metallic multilayers. *Nanotechnology*, 31(29):292002, May 2020. ISSN 0957-4484. URL http://doi.org/10.1088/1361-6528/ab803f.

[16] S. H. Oh, M. Legros, D. Kiener, and G. Dehm. In situ observation of dislocation nucleation and escape in a submicrometre aluminium single crystal. *Nat. Mater.*, 8:95–100, February 2009. ISSN 1476-4660. URL http://doi.org/10.1038/nmat2370.

[17] V. Samaee, S. Sandfeld, H. Idrissi, J. Groten, T. Pardoen, R. Schwaiger, and D. Schryvers. Dislocation structures and the role of grain boundaries in cyclically deformed Ni micropillars. *Mater. Sci. Eng., A*, 769:138295, January 2020. ISSN 0921-5093. URL http://doi.org/10.1016/j.msea.2019.138295.

[18] N. Hansen and D. J. Jensen. Development of microstructure in FCC metals during cold work. *Philos. Trans. R. Soc. London, Ser. A*, 357(1756):1447–1469, June 1999. ISSN 1471-2962. URL http://doi.org/10.1098/rsta.1999.0384.

[19] D. Kuhlmann-Wilsdorf and N. Hansen. Geometrically necessary, incidental and subgrain boundaries. *Scr. Metall. Mater.*, 25(7):1557–1562, July 1991. ISSN 0956-716X. URL http://doi.org/10.1016/0956-716X(91)90451-6.

[20] O. Rezvanian, M. A. Zikry, and A. M. Rajendran. Statistically stored, geometrically necessary and grain boundary dislocation densities: microstructural representation and modelling. *Proc. R. Soc. A.*, 463(2087):2833–2853, August 2007. ISSN 1471-2946. URL https://royalsocietypublishing.org/doi/10.1098/rspa.2007.0020.

[21] D. A. Hughes, N. Hansen, and D. J. Bammann. Geometrically necessary boundaries, incidental dislocation boundaries and geometrically necessary dislocations. *Scr. Mater.*, 48(2):147–153, January 2003. ISSN 1359-6462. URL http://doi.org/10.1016/S1359-6462(02)00358-5.

[22] F. Cardarelli. *Materials Handbook*. Springer, London, England, UK, 2008. ISBN 978-1-84628-669-8. URL https://link.springer.com/book/10.1007/978-1-84628-669-8.

[23] D. A. Hughes and N. Hansen. Microstructure and strength of nickel at large strains. *Acta Mater.*, 48(11):2985–3004, June 2000. ISSN 1359-6454. URL http://doi.org/10.1016/S1359-6454(00)00082-3.

[24] E.-W. Huang, R. Barabash, G. Ice, W. Liu, Y.-L. Liu, J.-J. Kai, and P. Liaw. Cyclic-loading-induced Accumulation of Geometrically Necessary Dislocations Near Grain Boundaries in an Ni-based Superalloy. *JOM*, 61:53–58, December 2009. URL http://doi.org/10.1007/s11837-009-0181-9.

[25] S. Li, C. A. Powell, S. Mathaudhu, B. Gwalani, A. Devaraj, and C. Wang. Review of recent progress on in situ TEM shear deformation: a retrospective and perspective view. *J. Mater. Sci.*, 57(26):12177–12201, July 2022. ISSN 1573-4803. URL http://doi.org/10.1007/s10853-022-07331-4.

[26] R. Gautier, A. Rajabzadeh, M. Larranaga, N. Combe, F. Mompiou, and M. Legros. Shear-coupled migration of grain boundaries: the key missing link in the mechanical behavior of small-grained metals? *C. R. Phys.*, 22(S3):19–34, 2021. ISSN 1878-1535. URL http://doi.org/10.5802/crphys.52.

[27] F. Mompiou, D. Caillard, M. Legros, and H. Mughrabi. In situ TEM observations of reverse dislocation motion upon unloading in tensile-deformed UFG aluminium. *Acta Mater.*, 60(8):3402–3414, May 2012. ISSN 1359-6454. URL http://doi.org/10.1016/j.actamat.2012.02.049.

[28] A. Rajput and S. K. Paul. Bauschinger Effect Analysis in Polycrystalline Copper: an Atomistic Simulation. *Trans. Indian Natl. Acad. Eng.*, 7(1):235–242, March 2022. ISSN 2662-5423. URL http://doi.org/10.1007/s41403-021-00266-3.

[29] M. J. Cordill, M. S. Lund, J. Parker, C. Leighton, A. K. Nair, D. Farkas, N. R. Moody, and W. W. Gerberich. The Nano-Jackhammer effect in probing near-surface mechanical properties. *Int. J. Plast.*, 25(11):2045–2058, November 2009. ISSN 0749-6419. URL http://doi.org/10.1016/j.ijplas.2008.12.015.

[30] G.-D. Sim, Y. Hwangbo, H.-H. Kim, S.-B. Lee, and J. J. Vlassak. Fatigue of polymer-supported Ag thin films. *Scr. Mater.*, 66(11):915–918, June 2012. ISSN 1359-6462. URL http://doi.org/10.1016/j.scriptamat.2012.02.030.

[31] C. Gammer, V. Burak Ozdol, C. H. Liebscher, and A. M. Minor. Diffraction contrast imaging using virtual apertures. *Ultramicroscopy*, 155:1–10, August 2015. ISSN 0304-3991. URL http://doi.org/10.1016/j.ultramic.2015.03.015.

[32] M. Klinger. More features, more tools, more CrysTBox. *J. Appl. Crystallogr.*, 50(4):1226–1234, August 2017. ISSN 1600-5767. URL http://doi.org/10.1107/S1600576717006793.

5

Grain rotation and crack propagation in bulge tested gold films with 4D-STEM

David D. Gebhart[a], Lukas Schretter[a], Anna Krapf[b], Benoit Merle[c], Megan J. Cordill[a], Christoph Gammer[a],

[a] Erich Schmid Institute of Materials Science, Austrian Academy of Sciences, Jahnstrasse 12, 8700 Leoben, Austria
[b] Department of Materials Science & Engineering, Institute 1, University of Erlangen-Nürnberg (FAU), Martensstrasse 5, 91058 Erlangen, Germany
[c] Institute of Materials Engineering, University of Kassel, Moenchebergstr. 3, 34125 Kassel, Germany

This chapter is reprinted from the article: D. D. Gebhart, L. Schretter, A. Krapf, B. Merle, M. J. Cordill, and C. Gammer. Grain rotation and crack propagation in bulge tested gold films with 4D-STEM, under review at JOM (JOMJ-D-24-01590) at the time of the submission of this thesis.

Contents

Abstract

This work investigates the stable crack propagation in notched, ultrafine-grained, free-standing Au films under cyclic loading with a bulge tester. Using intermittent transmission electron microscopy, including 4D scanning transmission electron microscopy, the study investigates dislocation activities and grain-boundary-mediated processes during crack propagation at nanoscale resolution. The regions surrounding the propagating crack show significant out-of-plane grain rotation, grain boundary migration, and grain growth and coalescence. Orientation mapping highlights the influence of grain orientations and misorientations on deformation localization and the crack propagation path, emphasizing the complex interplay of microstructural features in fatigue properties. The findings highlight the role of grain-boundary-mediated mechanisms in the cyclic fatigue of metallic thin films, providing insights into damage mechanisms at the nanoscale.

5.1 Introduction

Fatigue crack propagation investigations are crucial in determining materials' deformation and failure behavior under cyclic loading conditions. Continuous deformation with each load cycle is usually associated with full or partial dislocation glide in the material and the well-known Hall-Petch relation demonstrates that a reduction in grain size up to a certain length scale will decrease a material's plastic flow caused by impeded dislocation mobility at grain boundaries (GB) [1, 2, 3]. In order to engineer materials with optimal properties, dislocation- and GB-mediated processes need to be visualized and studied. GB-mediated processes include GB migration [4], GB sliding [5], and grain rotation [6, 7]. The visualization is best performed by transmission electron microscopy (TEM) investigations where dislocations show up as streaks resulting from a decrease in electron transmission due to their associated lattice distortions or they can be visualized directly at atomic resolution. Furthermore, electron diffraction patterns can be acquired, containing information about crystallographic orientation. Samples can be strained in-situ inside the TEM to best capture processes and mechanisms associated with plastic flow. Several in situ methods have been established, the core principle is that the samples are mechanically connected to actuators, which are mostly piezoelectric, electrostatic, or based on thermal expansion. A thorough review on available methods and devices has recently been published by Li et al. [8]. Recent improvements in electron detectors have led to increased utilization of four-dimensional scanning transmission electron microscopy (4D-STEM) methods. A convergent, parallel, or precessing electron beam is scanned over a sample region and a map of diffraction patterns is recorded. This data can be processed to generate orientation maps [9, 10] and strain maps [11, 12] among other parameters.

This work uses a recently developed setup [13] to combine cyclic uniaxial stress with intermittent TEM characterization, including 4D-STEM methods. An ultrafine-grained (UFG) 150 nm freestanding, electron-transparent Au film with a small notch in the center is cyclically loaded using a bulge-tester. The sample is intermittently placed into a TEM where both STEM images and nanobeam electron diffraction pattern maps are recorded. This approach allows a crack initiated by the notch to be followed and to understand how the crystallographic orientations of the grains influences deformation localization, microstructural changes, and the crack propagation path.

5.2 Materials and methods

To produce freestanding Au thin films, custom substrates were purchased from Silson Ltd. (Southam, UK). The substates consist of a square Si chip (12.5 mm edge length and of 525 µm thickness) coated with a 100 nm silicon nitride (SiNx) film on top. At the center they contain pre-etched a 1×4 mm^2 window holding the freestanding SiNx membrane. Au films 150 nm thick were deposited on the SiNx-coated side of the substrate by thermal evaporation, using a self-built deposition system, previously described by E. Preiß et al. [14]. The deposition system is equipped with a quartz crystal oscillator for monitoring the deposition rate and the thickness of the deposited film and with halogen lamps used for substrate heating. The deposition was performed at a substrate temperature of 80 °C and a deposition rate of 1.0 Å/s while rotating the substrate at 10 rpm, resulting in a columnar, UFG microstructure. Subsequent heat treatment of two hours at 120 °C was applied. The SiNx membrane was then removed from the window backside by reactive ion etching for three minutes with a PlasmaLab 80Plus (Oxford Instruments plc, UK) at a pressure of 95 mTorr, using a CF_4 flow of 100 sccm, and 100 W RF power, resulting in a freestanding Au film. Finally, a notch of 10 µm length and approximately 200 nm width was cut at the center of the freestanding Au film, running along the long axis of the window using a focused ion beam (FIB) in a Zeiss AURIGA Workstation (Carl Zeiss AG, Germany). The notch was milled with Ga^+ ions at an acceleration voltage of 30 kV and an ion current of 10 pA, over a duration of approximately 10 seconds.

Vacuum adhesive was used at a temperature of 150 °C on a heating plate to attach the sample onto a custom-made sample retainer, designed to fit onto a bulge test setup and on a TEM holder, described in detail in [13]. The setup allows the sample (glued to the custom retainer) to be placed directly onto the bulge tester and into the TEM without any further modifications. This allows to perform intermittent TEM investigations during bulge testing. The sample retainer is mounted onto the bulge tester by screws, with fixed o-rings ensuring an airtight seal. For bulge testing a custom made setup was used, built

by Merle and Göken [15]. The setup is equipped with an autofocus laser displacement sensor to measure the deflection of the freestanding film. The laser was aligned with the center of the membrane before any fatigue loading was performed. An aspect ratio of 4 was chosen for the rectangular window because from Vlassak's model it is well-known in bulge testing that with an aspect ratio of 4 or greater, the long axis can be approximated to being of infinite length [16, 17]. This allows the assumption of zero strain and uniform membrane deflection along the long axis. Cyclic pressure was applied in triangular form at a frequency of 0.2 Hz and a peak nominal differential pressure of 14 kPa for two samples and 15 kPa for another sample. The gas exiting the notched and cracked region is negligible and was not visible in any of the continuously recorded pressure measurements.

To characterize the damage evolution of the Au thin film during cyclic bulge testing intermittent TEM investigations were carried out in a JEM-2200FS (JEOL Ltd., Akishima, Japan) using an acceleration voltage of 200 kV. Therefore, after a number of cycles, the bulge testing was interrupted and the sample retainer was transferred to the TEM. Using this approach a series of STEM micrographs could be recorded showing the damage evolution around the notch. Additionally, to investigate the evolution of the grain orientation during cyclic loading in more details for one samples 4D-STEM maps were recorded after 0, 100, and 1,000 cycles. For each state six maps spanning an area of approximately 1.8×1.8 μm^2 and consisting of 128×128 equally spaced nanobeam-diffraction patterns were recorded. A Merlin4R direct electron detector (Quantum Detectors, Oxfordshire, UK) was used to record 512×512 pixel nano diffraction patterns. Automated crystal orientation mapping (ACOM), a pattern matching algorithm to determine crystal orientations from nano diffraction patterns, was performed using a combination of preexisting and in-house developed Python code. Kinematical diffraction patterns covering the entire crystal symmetry were simulated using the packages Diffsims [18] and Orix [19]. Pattern matching was performed using an in-house developed code based on the method described in [20]. For better signal to noise ratio, 4 to 100 distinct patterns were recorded from the same grain.

5.3 Results and Discussion

Fig. 5.1 shows the in-plane and out-of plane orientation maps of the initial state. The sample has a strong [111] texture as seen from the out-of-plane orientation map. While previous bulge test studies on similar, but unnotched, freestanding Au films have shown that at room temperature, bulge testing results in catastrophic failure through rupture of the membrane [21, 22], we observed stable crack growth in all three notched samples up to the maximum applied cycle numbers of 15,000 (14 kPa) and 13,000 (15 kPa). Fig. 5.2

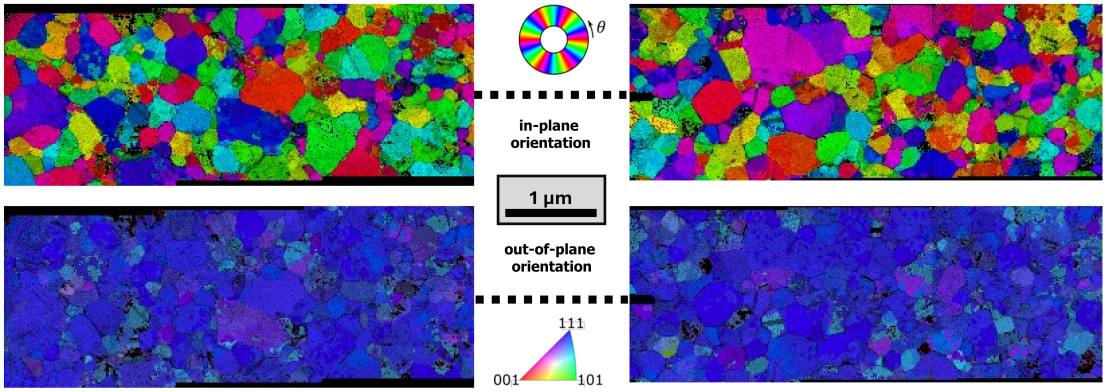

Figure 5.1: Orientation map showing the sample in its initial state on both sides of the notch (represented by the horizontal dashed line). The top row is the in-plane orientation maps and the bottom row the out-of-plane orientation maps. The mappings evidence a (111) out-of-plane texture. (color online)

gives an overview of stable crack growth propagating on both sides of the notch up to 15,000 cycles (14 kPa), with insets showing the enlarged region just left of the notch after 30 and 4600 cycles. Stable crack growth was also observed for the sample loaded at 15 kPa. In the following the mechanisms of crack growth will be studied in detail using the sample strained to 1,000 cycles at 14 kPa nominal differential peak pressure, whose data set includes 4D-STEM maps.

Fig. 5.3 presents the crack propagation path to the left and the right of the notch with the region where the crack propagates depicted after 0 ((a) and (b)) and 1,000 cycles ((c) and (d)). The crack propagates mostly transgranular but there are some sections, especially at regions of smaller grain sizes, where crack propagation is intergranular, marked by white arrows in the crack propagation path in Fig. 5.3 (a) and (b). In the vicinity of the crack path post-loading, activated slip systems are visible at both sides of the notch in the form of slip bands and also cross-slip is observed (Fig. 5.3(c) and (d)). A similar mix of transgranular and intergranular propagation was observed by Kondo et al. [23] in fatigue investigations of freestanding UFG Cu of 100 nm thickness while they only observed transgranular propagation in a 500 nm thick sample with larger grain size distribution. Molecular dynamics (MD) simulations of monotonic straining of nano-grained (NG) and gradient nano-grained (GNG) Cu, with grain sizes in the range of 10 nm, show some transgranular fracture associated with dislocation activities but intergranular fracture is the dominant mechanism through the formation and coalescence of voids at weak boundaries and triple junctions ahead of the crack tip [24].

A more detailed investigation of damage initiation and subsequent crack propagation is given in Fig. 5.4(a)-(c), showing bright-field STEM images of the right side of the

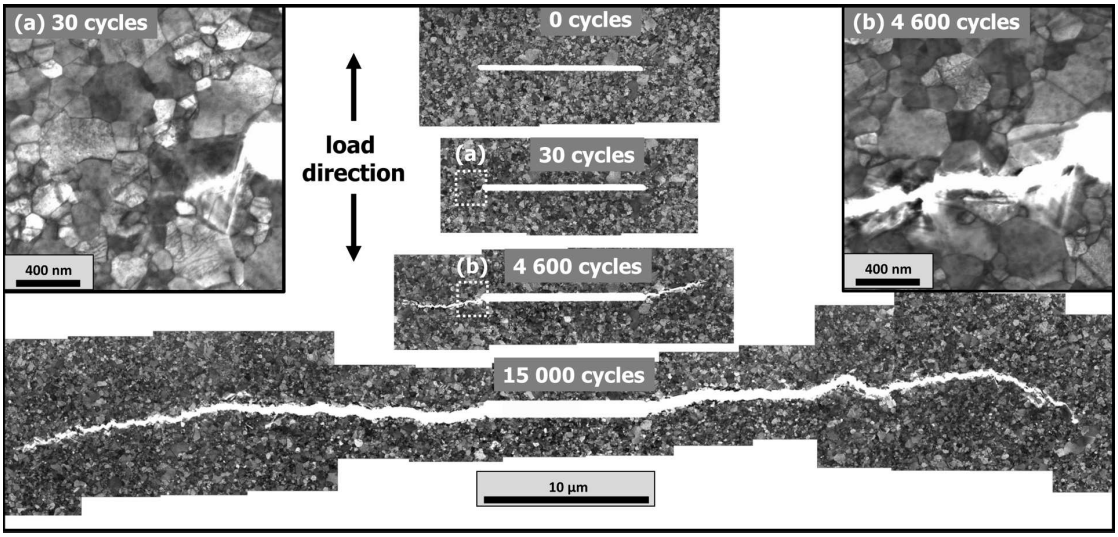

Figure 5.2: Bright-field STEM micrographs after 0, 30, 4600, and 15,000 cycles (14 kPa) show stable crack growth up to 15,000 cycles. The insets show enlarged depictions of the same region to the left of the notch after 30 (a) and 4600 (b) cycles.

notch, for the initial state and after 100 and 1,000 cycles, respectively. Fig. 4(d) and (e) give in-plane and (f) and (g) out-of-plane orientation maps in the initial state and after 1,000 cycles. Grains undergoing deformation are indicated with capital letters in Fig. 5.4(a). After 100 cycles deformation is localized in grains A and F to L (dashed white box) through slip and cross-slip. Additionally, voids or thinned regions appear at triple junctions and along GBs. Some slip bands initiate new slip bands through GBs while others appear to terminate or lead to cross-slip at GBs. Interestingly, with further cycling, the deformation is deflected into the region above the initial deformation zone (grain B-E) and after 1,000 cycles a crack path follows grains A-E (see Fig. 5.4(c) and dotted line in Fig. 5.4(a)).

The damage localization and crack propagation observed in the bright-field-STEM images appear to be influenced by both ip and oop angular mismatch between grains. It is well known that the probability of transmission of dislocations over GBs largely depends on the misalignment angle of neighboring grains, more precisely the angle between slip plane normals [25]. The fact that deformation is initially localized in grains F-L indicates that the barrier is smaller for deformation to propagate from grain A to the area below the notch rather than the area above the notch. The grains predominantly show a [111] zone axis in the initial state, as is to be expected with the earlier described texture of the films, and grains F and M are tilted out-of-plane from the [111] zone axis. Along the final crack propagation path, there is at first a large in-plane rotational mismatch

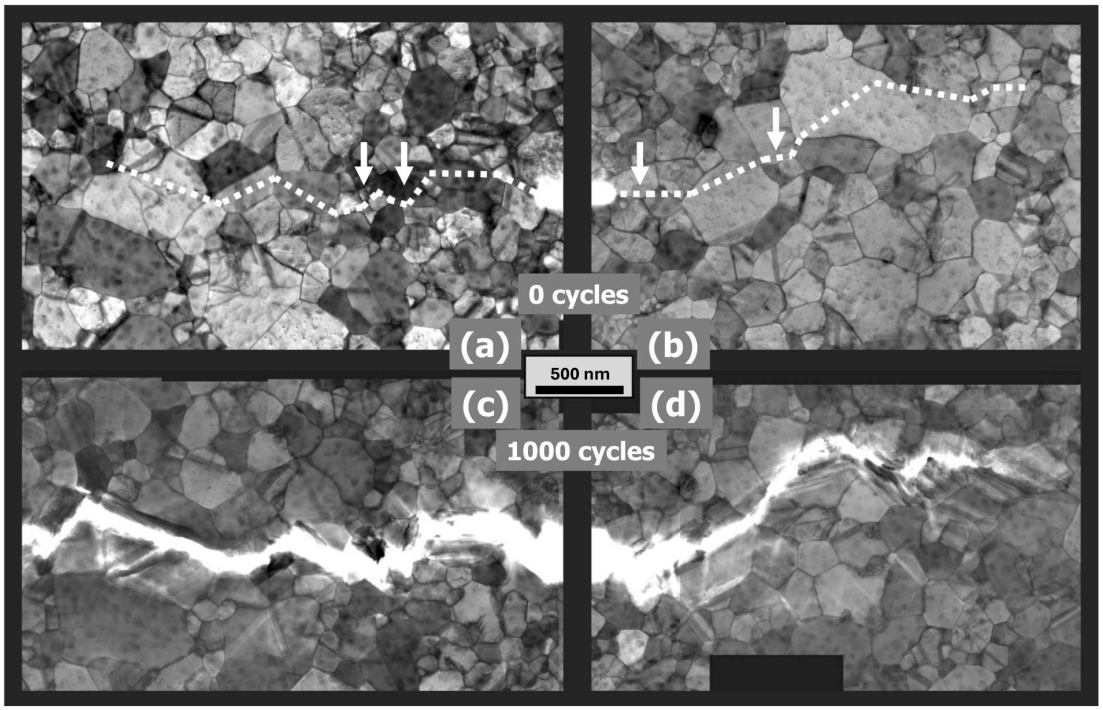

Figure 5.3: Bright-field STEM micrographs showing areas to the left and the right of the notch of the investigated sample in the initial state (a, b) and post-loading (c, d). Intergranular crack propagation is indicated between the white arrows in (a) and (b).

between grains A/B and B/C, and still a significant mismatch of around 10 ° at the relatively small shared boundary A/C. The in-plane rotational mismatch appears to be the initial barrier to plastic flow, showing three different slip bands terminating at the A/B boundary after 100 cycles (indicated by a white arrow in Fig. 5.4 (b); see also Fig. 5.5 (b)). There is a large in-plane angular mismatch at the boundaries between grains G and H with grains I and J, with the smallest angle present at the G/J boundary at around 13 °. Here, the plastic flow seems to be constrained to the GBs, indicated by areas of higher contrast at GBs and triple junctions after 100 cycles and by no apparent slip bands in grains I and J after 1,000 cycles (Fig. 5.4 (b) and (c)). However, the plastic flow does traverse this region and distinct slip bands are visible in the neighboring grains after 100 cycles (indicated in Fig. 5.4 (b)).

After 1,000 cycles, however, a crack develops through the area above the notch (grains A-E), suggesting that there may be a barrier at the end of the initial deformation zone (grains M-N) that is larger than the initial barrier that prevented deformation to propagate from grain A to grains B-E. The final barrier leading to the deflection of the crack above

the initial deformation zone appears to be grain M which does not show a [111] zone axis, is rotated out-of-plane, and its GBs with surrounding [111] grains are twist boundaries that can show reduced dislocation transmission probabilities compared to tilt boundaries [26] and were found to be a larger barrier to transgranular crack propagation [27]. M shares a long boundary with K and although slip bands are numerous in K after 100 and 1,000 cycles, none directly traverse the boundary and the only slip band visible in M after 1,000 cycles appears to originate at a triple junction. Another indicator is dense dislocation pile-ups at the top and bottom right of grain K (see white arrows in Fig. 5.4 (c)).

After 1,000 cycles, the crack has propagated transgranular through grain A, intergranular around grain C, and transgranular through grains D and E, with no significant deflection at the D/E boundary where the in-plane mismatch angle is smaller at approximately 5 °. A closer look at the transformation of the region around grains A to C is depicted in Fig. 5.5. Table 5.1 shows the out-of-plane orientation of grains highlighted in Fig. 5.5. In the initial state, all grains except for Q show [111] texture but the grains rotate out-of-plane and show increasing tilt angles, away from the [111] axis.

This grain rotation occurs alongside distinct GB migration of the A/B, A/P, and possibly the A/O boundary. Grain O is a special case here since it is annihilated within the first 100 load cycles. The data shows a small angle tilt boundary (in-plane rotation) between grain O and P of approximately 2 ° and an even smaller out-of-plane rotational mismatch of less than 1 ° (see Table 5.1) which might lead to grain-rotation-induced grain coalescence of O and P which has been suggested as a mechanism of grain coarsening in nanocrystalline (NC) metals [28] and has been observed in a cyclically loaded NC gold film in an in-situ TEM investigation [29].

Additionally, GB migration is observed at the A/B and the A/P boundaries. The boundaries do not migrate in their GB-plane-normal directions but the A/P boundary plane rotates over the first 100 cycles and a curvature is introduced at the A/B boundary. Shear stresses are strong in this region close to the crack and shear deformations are numerous in grain A due to plastic flow at slip bands (direction of bands indicated by blue dotted lines in Fig. 5.5 (b)) which suggests that some form of shear-induced GB migration is observed. Shear-induced GB migration is an active area of research with many proposed models [30]. Liebig et al. recently observed shear-coupled GB migration in a freestanding nanocrystalline Au film with (111) columnar texture at boundaries along an angle approximately 45 ° off the loading axis, where they described increased ductility of the specimen due to GB sliding and GB migration [31]. A disconnection-mediated mechanism of shear-coupled grain boundary migration was recently described in great detail for a low energy <110> tilt boundary in Au bicrystals in an in-situ TEM study supported by MD simulations [32, 33].

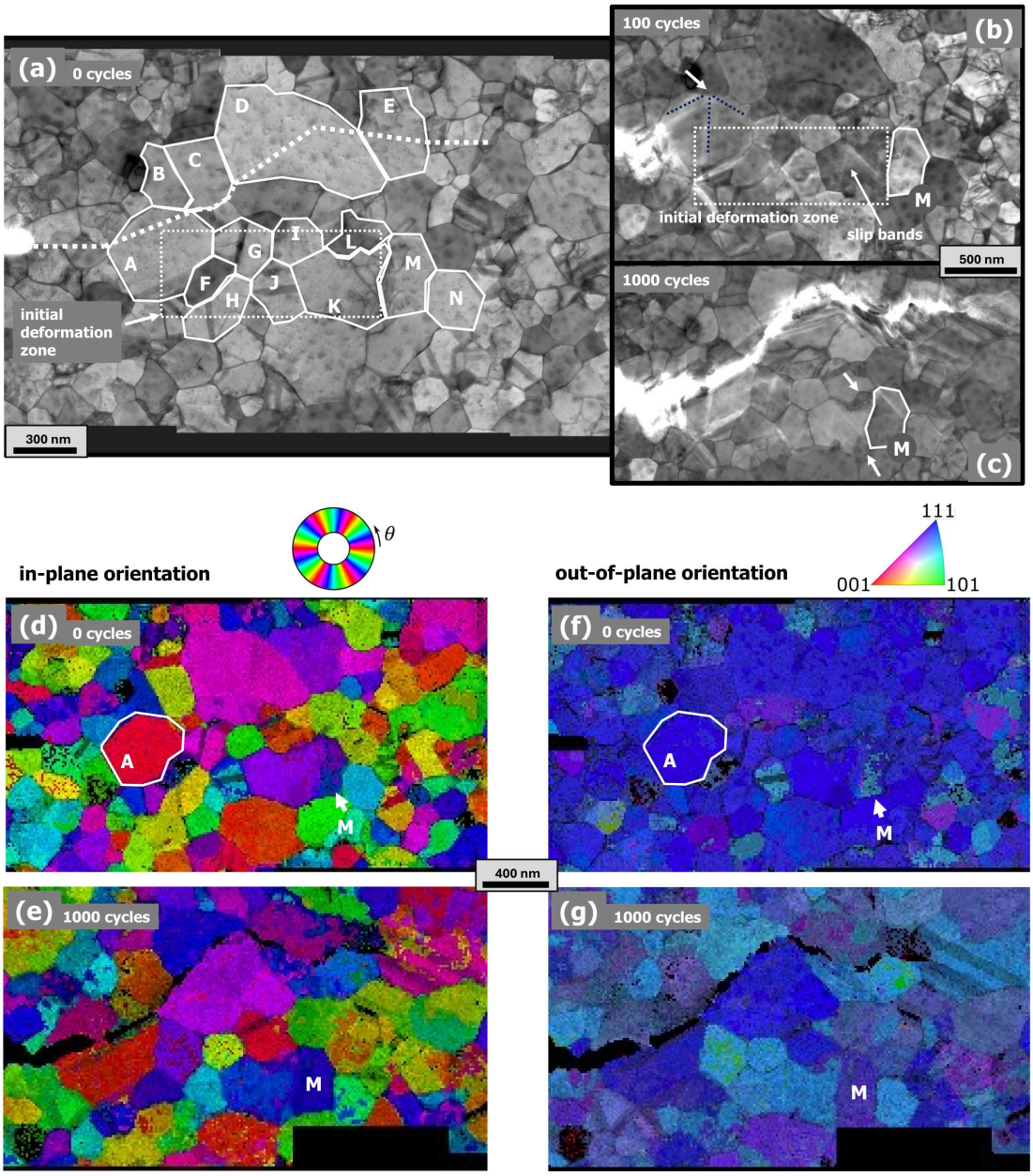

Figure 5.4: Bright-field STEM micrographs (a to c) to the right of the notch in the initial state (a), after 100 load cycles (b), and after 1,000 cycles (c). (d) and (e) show an in-plane and (f) and (g) an out-of-plane orientation map of the corresponding regions in the initial state and after 1,000 cycles. The crack path is highlighted by a white dotted line in (a). An area where most plastic flow happens over the first 100 cycles is roughly outlined by a white dotted box in (a) and (b). Active slip systems terminating at a boundary are indicated by dotted blue lines running parallel to them in (b) and slip bands crossing a boundary are indicated by white arrows to the left of grain M.

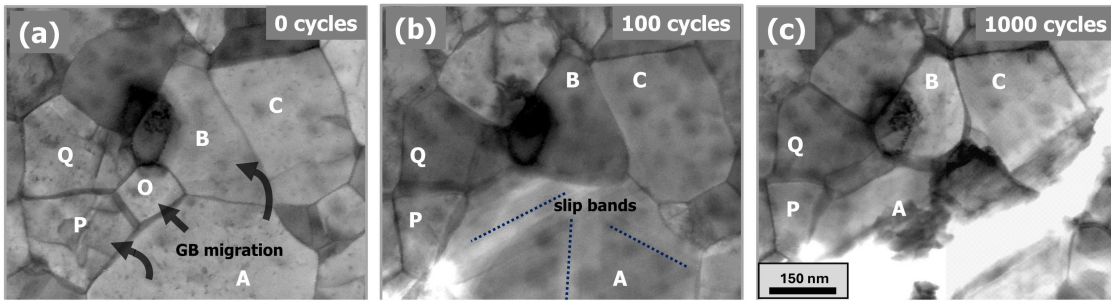

Figure 5.5: Grain boundary migration observed from the initial state (a), after 100 cycles (b), to the final state after 1,000 cycles (c). Grains A-C are the same as in Fig. 5.4 and grains O-Q are newly indexed. Black arrows arrows in (a) indicate GB migration direction. Blue dotted lines in (b) indicate active slip systems. Depicted diffraction patterns correspond to the state of the sample in the micrograph to their left. (color online)

Further examination of Fig. 5.5 reveals that the boundaries around grain Q appear to be relatively stable and while the grain itself rotates both in-plane and out-of-plane during cycling, no indications for extensive plastic flow are visible in the TEM micrographs. This does support the earlier notion that grain M (see Fig. 5.4), which also shows an initial out-of-plane rotation to its neighbors, is the proposed large barrier to plastic flow that leads to the deflection of deformation and crack propagation.

To ensure that the out-of-plane rotations observed in all investigated regions during cycling are not a global phenomenon introducing homogeneous tilt over all observed regions but that the out-of-plane rotations are localized, Fig. 5.6 shows orientation maps with out-of-plane tilt away from the [111] zone axis in the initial state (a), after 100 cycles (b), and after 1,000 cycles (c). In Fig. 5.6 (b) increased tilt from the [111] zone axis is observed closer to the notch tip which confirms that there is a gradient in out-of-plane rotation. Such out-of-plane rotations of grains have previously been observed directly at the propagating crack in similarly notched Au films in monotonic bulge tests with in-situ atomic force microscopy investigations, albeit only within a narrow path along the crack growth direction [34].

While Fig. 5.5 highlights the migration of boundaries, Fig. 5.7 presents the complete coalescence of two grains in two different locations. With respect to the mean propagation direction of the crack, parallel to the long axis of the notch, the boundary walls of interest are rotated 90 ° compared to the migrating boundaries presented in Fig. 5.5. With the simplified assumption that shear stresses are on average at a maximum at 45 ° angles from the crack tip at both sides, the shear stresses at the boundaries here (rotated 135 °

Table 5.1: Out-of-plane orientation data for grains depicted in Fig. 5.5 at different states and cycle counts.

Grain	OOP-Vector	Tilt [°] from [111]
Initial State		
A	[0.56, 0.56, 0.61]	2.0
B	[0.56, 0.56, 0.61]	2.0
C	[0.56, 0.54, 0.63]	3.6
O	[0.60, 0.54, 0.60]	2.9
P	[0.57, 0.55, 0.61]	2.6
Q	[0.60, 0.43, 0.67]	10
After 100 Cycles		
A	[0.50, 0.44, 0.74]	13
B	[0.58, 0.49, 0.65]	6.6
C	[0.49, 0.43, 0.76]	14
O	/	/
P	[0.62, 0.42, 0.66]	10
Q	[0.62, 0.36, 0.70]	14
After 1,000 Cycles		
A	[0.58, 0.38, 0.72]	14
B	[0.63, 0.43, 0.65]	10
C	[0.53, 0.40, 0.75]	15
O	/	/
P	[0.61, 0.41, 0.68]	11
Q	[0.60, 0.38, 0.70]	13

or -45 ° to the propagation direction) are lower than at the migrating boundaries in Fig. 5.5. The absolute mismatch angles between the grains of interest are calculated from the in-plane and out-of-plane mismatch angles and annotated in Fig. 5.7. Fig. 5.7 (a) are further away from the notch tip and no significant change in their mismatch angle was observed from the initial state and after 100 cycles. However, after 1,000 cycles the two grains have fully combined. In the immediate surroundings, some smaller grains were annihilated but no extensive GB migration can be observed. The coalescing grains depicted in Fig. 5.7 (b) are situated closer to the notch tip and the mismatch angle between the two grains decreases from approximately 13 ° in the initial state to 7 ° after 100 cycles, without distinct GB migration. After 1,000 cycles the two grains have also coalesced, possibly indicating grain-rotation-induced grain coalescence. Note that there

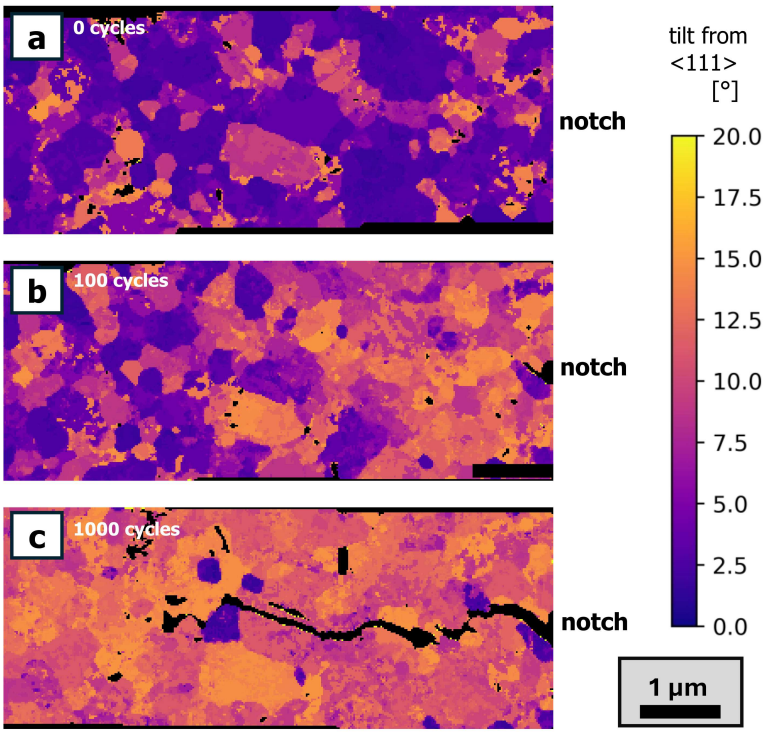

Figure 5.6: Orientation maps of the area left of the notch after 0, 100, and 1,000 cycles demonstrating an increase in out-of-plane tilt away from the [111] zone axis with increasing cycle number and with increasing distance from the notch. (color online)

is a twin boundary (TB) in the upper grain, manifested as a broad dark streak, best visible at 0 cycles. The diffraction patterns of this grain were all taken from the area below that TB.

From the available data, it is not entirely clear whether the observed coalescence process is governed by GB migration, or whether grain rotation is the main contributor. There are some indications for grain-rotation-induced grain coalescence: The grain boundary planes lie normal to the direction where shear stresses can on average be expected to show a maximum, a relatively large grain is fully annihilated in both regions, no GB migration is observed over the first 100 cycles between the coalescing grains, no extensive GB migration is observed in the immediate vicinity of the two grains over all 1,000 cycles, and grain rotation in the out-of-plane direction is observed throughout the sample during cyclic loading. Available literature indicates a cooperative process: Yang et al. observed both GB migration and grain rotation ahead of a crack tip in monotonic straining of a NG Au sample in high-resolution TEM investigations and accompanying MD simulations showed grain coalescence ahead of the crack tip as a joint process of both GB migration

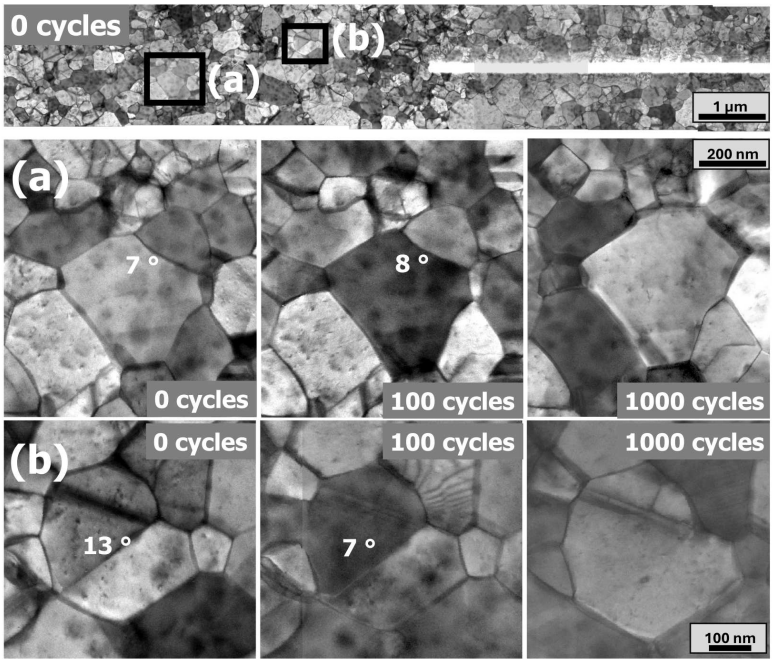

Figure 5.7: The top image is an overview of the sample in the initial state, with two areas outlined where two grains are observed to coalesce. (a) and (b) show the evolution of the two regions with increasing cycle numbers. Cycle numbers are increasing left to right and are indicated in the micrographs.

and grain rotation [35]. Additionally, they found that rotation was more prominent in larger grains due to enhanced dislocation activities which is in agreement with an earlier study by Wang et al. that also observed simultaneous GB migration and grain rotation in NC Au [36]. It needs to be stated that their findings may not be entirely applicable to the larger grains of the UFG Au sample presented in this study and more closely spaced strain maps would be necessary to investigate the mechanism.

5.4 Conclusions

The present paper investigates the deformation mechanisms of a notched freestanding thin Au film during cyclic loading in a bulge-tester. Intermittent STEM images during deformation are used to follow the deformation at the nanoscale, along with STEM orientation maps. While unnotched Au films in high-cycle-fatigue experiments with a very similar setup show little dislocation activity and plastic deformations [13], in the present case the notch introduces stress localization leading to a slow crack propagation starting

from the notch tip. Several deformation mechanisms are observed near the notch including local slip, grain rotation, grain boundary migration, and grain growth. Interestingly crack propagation follows a mixture of intergranular and transgranular fracture. 4D-STEM-based orientation mapping demonstrates that deformation localization and crack propagation is linked to the local grain orientation, specifically the misorientation between neighboring grains. The film initially shows a strong [111] texture. Cyclic deformation results in an increase in out-of-plane misorientation around the crack tip, demonstrating that this is an important deformation mechanism for freestanding metal thin films.

5.5 Acknowledgements

Funding: This work was supported by the Austrian Science Fund (FWF) [Project I 4384-N] and the German Research Foundation (DFG) [grant ME-4368/8] within the framework of the D-A-CH cooperation FATIFACE.

5.6 Data Availability

The data that support the findings of this study are available from the corresponding author upon reasonable request.

5.7 Author Declarations

The authors have no conflicts to disclose.

5.8 References

[1] E. O. Hall. The Deformation and Ageing of Mild Steel: III Discussion of Results. *Proc. Phys. Soc. B*, 64(9):747, September 1951. ISSN 0370-1301. URL http://doi.org/10.1088/0370-1301/64/9/303.

[2] J. Petch N. The cleavage strength of polycrystals. *J. Iron Steel Inst*, 174:25–28, 1953.

[3] C. C. Pande, R. R. Masumura, and R. R. Armstrong. Pile-up based Hall-Petch relation for nanoscale materials. *Nanostructured materials*, 2(9):323–331, 1993. ISSN 09659773. URL http://doi.org/10.1016/0965-9773(93)90159-9.

[4] Z. Fang, J. Xiao, S. Tan, C. Deng, G. Wang, and S. X. Mao. Atomic-scale observation of dynamic grain boundary structural transformation during shear-mediated migration. *Sci. Adv.*, 8(45):eabn3785., November 2022. ISSN 2375-2548. URL http://doi.org/10.1126/sciadv.abn3785.

[5] J. Schiøtz, F. D. Di Tolla, and K. W. Jacobsen. Softening of nanocrystalline metals at very small grain sizes. *Nature*, 391:561–563, February 1998. ISSN 1476-4687. URL http://doi.org/10.1038/35328.

[6] J. Zhang, F. Yang, Y. Liu, Z. Zhong, and J. Zhao. On the deformation-induced grain rotations in gradient nano-grained copper based on molecular dynamics simulations. *Nanotechnology Reviews*, 10(1):87–98, January 2021. ISSN 2191-9097. URL http://doi.org/10.1515/ntrev-2021-0010.

[7] P. Liu, S. C. Mao, L. H. Wang, X. D. Han, and Z. Zhang. Direct dynamic atomic mechanisms of strain-induced grain rotation in nanocrystalline, textured, columnar-structured thin gold films. *Scr. Mater.*, 64(4):343–346, February 2011. ISSN 1359-6462. URL http://doi.org/10.1016/j.scriptamat.2010.10.029.

[8] K. Li, Y. Bu, and H. Wang. Advances on in situ TEM mechanical testing techniques: a retrospective and perspective view. *Front. Mater.*, 10:1207024, June 2023. ISSN 2296-8016. URL http://doi.org/10.3389/fmats.2023.1207024.

[9] H. Idrissi, A. Kobler, B. Amin-Ahmadi, M. Coulombier, M. Galceran, J.-P. Raskin, S. Godet, C. Kübel, T. Pardoen, and D. Schryvers. Plasticity mechanisms in ultrafine grained freestanding aluminum thin films revealed by in-situ transmission electron microscopy nanomechanical testing. *Appl. Phys. Lett.*, 104(10), March 2014. ISSN 0003-6951. URL http://doi.org/10.1063/1.4868124.

[10] S. Stangebye, Y. Zhang, S. Gupta, E. Hosseinian, F. Yu, C. Barr, K. Hattar, O. Pierron, T. Zhu, and J. Kacher. Grain growth of nanocrystalline aluminum under tensile deformation: A combined in situ TEM and atomistic study. *Materialia*, 16:101068, May 2021. ISSN 2589-1529. URL http://doi.org/10.1016/j.mtla.2021.101068.

[11] V. B. Ozdol, C. Gammer, X. G. Jin, P. Ercius, C. Ophus, J. Ciston, and A. M. Minor. Strain mapping at nanometer resolution using advanced nano-beam electron diffraction. *Appl. Phys. Lett.*, 106(25), June 2015. ISSN 0003-6951. URL http://doi.org/10.1063/1.4922994.

[12] S. Karner, O. Blank, M. Rösch, J. Zalesak, J. Keckes, and C. Gammer. Nanobeam electron diffraction strain mapping in monocrystalline silicon of modern trench power MOSFETs. *Microelectron. Eng.*, 264:111870, August 2022. ISSN 0167-9317. URL http://doi.org/10.1016/j.mee.2022.111870.

[13] A. Krapf, B. Merle, D. D. Gebhart, M. Reiter, A. Lassnig, M. Göken, M. J. Cordill, and C. Gammer. Observing High-Cycle Fatigue Damage in Freestanding Gold Thin Films with Bulge Testing and Intermittent Transmission Electron Microscopy Imaging. *Advanced Engineering Materials*, 2024. URL http://doi.org/10.1002/adem.202400216. Cited by: 0; All Open Access, Hybrid Gold Open Access.

[14] E. I. Preiß, F. Gannott, M. Göken, and B. Merle. Scaling of the fracture toughness of freestanding metallic thin films with the yield strength. *Mater. Res. Lett.*, October 2018. URL https://www.tandfonline.com/doi/full/10.1080/21663831.2018.1520749.

[15] B. Merle and M. Göken. Fracture toughness of silicon nitride thin films of different thicknesses as measured by bulge tests. *Acta Mater.*, 59(4):1772–1779, February 2011. ISSN 1359-6454. URL http://doi.org/10.1016/j.actamat.2010.11.043.

[16] J. J. Vlassak and W. D. Nix. A new bulge test technique for the determination of Young's modulus and Poisson's ratio of thin films. *J. Mater. Res.*, 7(12):3242–3249, December 1992. ISSN 2044-5326. URL http://doi.org/10.1557/JMR.1992.3242.

[17] Y. Xiang, X. Chen, and J. J. Vlassak. Plane-strain Bulge Test for Thin Films. *J. Mater. Res.*, 20(9):2360–2370, September 2005. ISSN 2044-5326. URL http://doi.org/10.1557/jmr.2005.0313.

[18] pyxem/diffsims: diffsims v0.6.0, June 2024. URL http://doi.org/10.5281/zenodo.11491307. [Online; accessed 22. Aug. 2024].

[19] pyxem/orix: orix 0.12.1.post0, August 2024. URL http://doi.org/10.5281/zenodo.11068626. [Online; accessed 22. Aug. 2024].

[20] E. F. Rauch and M. Véron. Automated crystal orientation and phase mapping in TEM. *Mater. Charact.*, 98:1–9, December 2014. ISSN 1044-5803. URL http://doi.org/10.1016/j.matchar.2014.08.010.

[21] B. Merle and M. Göken. Bulge fatigue testing of freestanding and supported gold films. *J. Mater. Res.*, 29(2):267–276, January 2014. ISSN 2044-5326. URL http://doi.org/10.1557/jmr.2013.373.

[22] A. Krapf, D. D. Gebhart, C. Gammer, M. J. Cordill, and B. Merle. Creep-dominated fatigue of freestanding gold thin films studied by bulge testing. *Materials Science and Engineering: A*, 887:145759, 2023. ISSN 0921-5093. URL http://doi.org/https://doi.org/10.1016/j.msea.2023.145759.

[23] T. Kondo, H. Hirakata, and K. Minoshima. Thickness effects on fatigue crack propagation in submicrometer-thick freestanding copper films. *Int. J. Fatigue*, 103:444–455, October 2017. ISSN 0142-1123. URL http://doi.org/10.1016/j.ijfatigue.2017.06.029.

[24] Y. Liu, F. Yang, X. Zhang, J. Zhang, and Z. Zhong. Crack propagation in gradient nano-grained metals with extremely small grain size based on molecular dynamic simulations. *Int. J. Fract.*, 233(1):71–83, January 2022. ISSN 1573-2673. URL http://doi.org/10.1007/s10704-021-00610-2.

[25] H. Pan, Y. He, and X. Zhang. Interactions between Dislocations and Boundaries during Deformation. *Materials*, 14(4):1012, February 2021. ISSN 1996-1944. URL http://doi.org/10.3390/ma14041012.

[26] D. W. Adams, D. T. Fullwood, R. H. Wagoner, and E. R. Homer. Atomistic survey of grain boundary-dislocation interactions in FCC nickel. *Comput. Mater. Sci.*, 164:171–185, June 2019. ISSN 0927-0256. URL http://doi.org/10.1016/j.commatsci.2019.04.007.

[27] S. Chandra, N. Naveen Kumar, M. K. Samal, V. M. Chavan, and S. Raghunathan. An atomistic insight into the fracture behavior of bicrystal aluminum containing twist grain boundaries. *Comput. Mater. Sci.*, 130:268–281, April 2017. ISSN 0927-0256. URL http://doi.org/10.1016/j.commatsci.2017.01.023.

[28] D. Moldovan, V. Yamakov, D. Wolf, and S. R. Phillpot. Scaling Behavior of Grain-Rotation-Induced Grain Growth. *Phys. Rev. Lett.*, 89(20):206101, October 2002. ISSN 1079-7114. URL http://doi.org/10.1103/PhysRevLett.89.206101.

[29] A. Kobler, A. Kashiwar, H. Hahn, and C. Kübel. Combination of in situ straining and ACOM TEM: A novel method for analysis of plastic deformation of nanocrystalline metals. *Ultramicroscopy*, 128:68–81, May 2013. ISSN 0304-3991. URL http://doi.org/10.1016/j.ultramic.2012.12.019.

[30] S. Li, C. A. Powell, S. Mathaudhu, B. Gwalani, A. Devaraj, and C. Wang. Review of recent progress on in situ TEM shear deformation: a retrospective and perspective view. *J. Mater. Sci.*, 57(26):12177–12201, July 2022. ISSN 1573-4803. URL http://doi.org/10.1007/s10853-022-07331-4.

[31] J. P. Liebig, M. Mačković, E. Spiecker, M. Göken, and B. Merle. Grain boundary mediated plasticity: A blessing for the ductility of metallic thin films? *Acta Mater.*, 215:117079, August 2021. ISSN 1359-6454. URL http://doi.org/10.1016/j.actamat.2021.117079.

[32] Q. Zhu, G. Cao, J. Wang, C. Deng, J. Li, Z. Zhang, and S. X. Mao. In situ atomistic observation of disconnection-mediated grain boundary migration. *Nat. Commun.*, 10(156):1–8, January 2019. ISSN 2041-1723. URL http://doi.org/10.1038/s41467-018-08031-x.

[33] Q. Zhu, S. C. Zhao, C. Deng, X. H. An, K. X. Song, S. X. Mao, and J. W. Wang. In situ atomistic observation of grain boundary migration subjected to defect interaction. *Acta Mater.*, 199:42–52, October 2020. ISSN 1359-6454.

[34] E. I. Preiß, B. Merle, and M. Göken. Understanding the extremely low fracture toughness of freestanding gold thin films by in-situ bulge testing in an AFM. *Mater. Sci. Eng., A*, 691:218–225, April 2017. ISSN 0921-5093. URL http://doi.org/10.1016/j.msea.2017.03.037.

[35] X.-S. Yang, S. Yuan, H. Fu, and Y.-J. Wang. Grain boundary-mediated plasticity accommodating the cracking process in nanograined gold: In situ observations and simulations. *Scr. Mater.*, 194:113693, March 2021. ISSN 1359-6462. URL http://doi.org/10.1016/j.scriptamat.2020.113693.

[36] L. Wang, T. Xin, D. Kong, X. Shu, Y. Chen, H. Zhou, J. Teng, Z. Zhang, J. Zou, and X. Han. In situ observation of stress induced grain boundary migration in nanocrystalline gold. *Scr. Mater.*, 134:95–99, June 2017. ISSN 1359-6462. URL http://doi.org/10.1016/j.scriptamat.2017.03.003.

6

Outlook

Summary and Outlook

In this work, it is demonstrated that detailed information about the evolution of damage in metallic thin films can be obtained from electrical resistance measurements during cyclic loading. A new method was developed that analyzes the full width at half maximum (FWHM) of electrical resistance peaks to detect the formation of through thickness cracks. Advanced microscopy techniques, including intermittent transmission electron microscopy and 4D scanning transmission electron microscopy, were utilized to observe how microstructural features, such as grain orientations and dislocation structures, affect fatigue behavior at the nanoscale. The research presented in this thesis has advanced the understanding of fatigue behavior and damage mechanisms in metallic thin films, particularly emphasizing the role of interfaces and microstructural characteristics. Despite these contributions, additional research is needed to further harness the potential of thin film materials in technological applications.

One of the immediate needs in the field is the establishment of a fixed failure criterion based on electrical resistance increase. Currently, the definition of failure varies across studies, with somewhat arbitrary thresholds in resistance increase set as failure criteria. This lack of standardization limits the comparability of results and the development of universally applicable models. Future research should aim to determine an optimal failure threshold that balances practical application requirements with material limitations. Establishing such a criterion would facilitate more consistent data interpretation and enhance the predictive capability of fatigue models.

The in-situ electrical resistance measurements have proven invaluable for monitoring damage evolution. However, the data processing methods used to analyze these measurements can be further refined. The simplified resistor network model introduced in Fig. 1.4 provides a framework for understanding the relationship between average crack length and linear crack density and electrical resistance. Expanding this model to

incorporate more complex material behaviors could lead to more accurate predictions of fatigue life. Integrating machine learning algorithms with experimental data could unveil hidden correlations and patterns, enhancing our ability to predict material failure. Such data-driven approaches could account for the numerous variables influencing fatigue behavior.

While electrical resistance measurements offer valuable insights, they provide limited information regarding the separation of crack length and crack density due to their inability to distinguish between parallel and series resistances. Investigating impedance measurements could address this limitation. By analyzing phase shifts resulting from capacitive and inductive effects around cracks, it may become feasible to differentiate between crack length and density in real time during fatigue testing. This approach is rather challenging to implement because the capacitances and inductances are very small. However, it could significantly enhance the resolution of damage characterization and provide a more comprehensive understanding of the failure mechanisms at play.

The presence of oxide layers on metallic thin films can also influence their fatigue behavior. Oxide layers may alter surface properties, affect adhesion at interfaces, and change the electrical characteristics of the films. Future studies should systematically investigate how different oxide formations impact fatigue life and damage evolution. Understanding these effects is particularly crucial for metals prone to oxidation, as it could lead to the development of protective coatings or treatment processes that enhance fatigue resistance.

With the rise of additive manufacturing and printed electronics, printed metallic materials are poised to become more prevalent in various applications. These materials often exhibit different microstructures and interface characteristics compared to traditionally deposited films. Research should focus on how these differences affect fatigue behavior, especially concerning interface adhesion and the initiation and propagation of cracks. Evaluating the fatigue properties of printed materials will be essential for their reliable integration into flexible and wearable devices.

The intermittent TEM approach combined with bulge testing presented in this thesis has proven to be an effective method for observing nanoscale deformation mechanisms. Given its relative ease of use and the richness of information it provides, this technique should be applied to a broader range of materials. By investigating different material systems, we can gain a more generalized understanding of fatigue mechanisms. Such studies could reveal material specific behaviors and guide the development of tailored solutions to enhance fatigue life.

Self-healing materials represent a promising area for extending the service life of thin film components. These materials can autonomously repair damage, potentially mitigating the effects of fatigue. Incorporating self-healing mechanisms into metallic thin films could revolutionize their application in flexible electronics and other technologies where mechanical integrity is critical. Future research should apply the advanced characterization methods outlined in this thesis, such as in-situ electrical measurements and TEM observations, to study self-healing processes at the micro- and nanoscale. Understanding how self-healing mechanisms interact with microstructural features and interfaces will be key to optimizing their performance.

The findings of this thesis have opened several pathways for future research. By establishing a standardized failure criterion, refining data processing techniques, and exploring new methods, we can enhance our understanding of fatigue behavior in metallic thin films. Investigating the effects of oxide layers, printed materials, and self-healing mechanisms will address emerging challenges and opportunities in materials science. Applying advanced characterization techniques across various materials will further deepen our knowledge of the fundamental mechanisms governing fatigue. This approach, combining experimental innovation with theoretical modeling, will be essential for developing the next generation of reliable, high-performance thin film materials for technological applications.